FINAL REPORT

Quantification of Hydrodynamic Forcing and Burial, Exposure and Mobility of Munitions on the Beach Face

SERDP Project MR-2503

FEBRUARY 2020

Jack A. Puleo
Demetra Cristaudo
University of Delaware

SERDP
DOD ▪ EPA ▪ DOE

REPORT DOCUMENTATION PAGE

Form Approved OMB No. 0704-0188

1. REPORT DATE *(DD-MM-YYYY)*	2. REPORT TYPE	3. DATES COVERED *(From - To)*
13-02-2020	Final Report	9/14/2015 - 3/13/2020

4. TITLE AND SUBTITLE
Quantification of Hydrodynamic Forcing and Burial, Exposure, and Mobility of Munitions on the Beach Face

5a. CONTRACT NUMBER
W912HQ-15-C-0007

5b. GRANT NUMBER

5c. PROGRAM ELEMENT NUMBER

6. AUTHOR(S)
Jack A. Puleo
Demetra Cristaudo

5d. PROJECT NUMBER
MR-2503

5e. TASK NUMBER

5f. WORK UNIT NUMBER

7. PERFORMING ORGANIZATION NAME(S) AND ADDRESS(ES)
University of Delaware
259 Academy Street
Newark, DE 19716

8. PERFORMING ORGANIZATION REPORT NUMBER
MR-2503

9. SPONSORING / MONITORING AGENCY NAME(S) AND ADDRESS(ES)
Strategic Environmental Research and Development Program
4800 Mark Center Drive
Suite 16F
Alexandria, VA 22350

10. SPONSOR/MONITOR'S ACRONYM(S)
SERDP

11. SPONSOR/MONITOR'S REPORT NUMBER(S)
MR-2503

12. DISTRIBUTION / AVAILABILITY STATEMENT
Approved for public release; distribution is unlimited
Distribution A

13. SUPPLEMENTARY NOTES

14. ABSTRACT
The presence of unexploded ordnance (UXO), or munitions, in nearshore and other underwater environments is a worldwide concern due to the past military activities. UXOs have been found in the surf zone and on populated beaches, posing a risk for the public. Behavior of munitions located on the sea bed is poorly understood. The goal of this project was to design and fabricate instrumented surrogate munitions for use in large-scale laboratory and field experiment to investigate UXO burial and migration under a range of forcing conditions. We seek to understand the processes that lead to UXO migration and what processes might lead to a munition being located on the beach face.

15. SUBJECT TERMS
Munitions, Surrogate Munitions, Inert Munitions, In Situ Sensors, Munitions Sensors, Mobility, Burial, Migration, Swash Zone, Foreshore, Sediment Transport

16. SECURITY CLASSIFICATION OF:			17. LIMITATION OF ABSTRACT	18. NUMBER OF PAGES	19a. NAME OF RESPONSIBLE PERSON
a. REPORT	b. ABSTRACT	c. THIS PAGE			Jack A. Puleo
UU	UU	UU	UU	92	19b. TELEPHONE NUMBER *(include area code)* 302-831-2440

Standard Form 298 (Rev. 8-98)
Prescribed by ANSI Std. Z39.18

Table of Contents

List of Tables

List of Figures

List of Acronyms

ADPV	-	Acoustic Doppler Profiling Velocimeter (Vectrino II)
AHRS	-	Attitude Heading and Reference System
ATC	-	Aberdeen Test Center
AVT	-	Allied Vision Technology
A_1	-	Angle difference between magnetic and true north
A_2	-	Angle difference between true north and local coordinate direction x
B	-	Munition burial depth
B / D_m	-	Munition relative burial depth
CCP	-	Conductivity Concentration Profiler
C_d	-	Drag coefficient
C_f	-	Friction coefficient for friction force
C_m	-	Added mass coefficient
D_m	-	Object or munition diameter
EMCM	-	ElectroMagentic Current Meter
F_{acc}	-	Fluid acceleration force
F_b	-	Buoyant force
F_d	-	Drag force
F_f	-	Friction force
F_i	-	Impact force
F_{macc}	-	Munition acceleration force
KC	-	Keulegan-Carpenter Number
GPS	-	Global Positioning System
H	-	Maximum water depth at breaker zone deployment location
H_s	-	Significant wave height
IMU	-	Inertial Motion Unit
I_x	-	Axial moment of inertia
J	-	Jonswap wave spectrum
L	-	Munition length
LiFe	-	Lithium iron Phosphate
LiPo	-	Lithium Polymer
L_0	-	Deep water wave length
LWE	-	Littoral Warfare Environment
M	-	Monochromatic wave spectrum
MD	-	Maryland
MLLW	-	Mean Lower Low Water
MR	-	Munitions Response
NASA	-	National Aeronautics and Space Administration
NAVD	-	North American Vertical Datum
NOAA	-	National Oceanic and Atmospheric Administration
PH	-	Photocell
PM	-	Pierson-Moskowitz wave spectrum
PT	-	Pressure Transducer
R	-	Runup
RTK	-	Real-time Kinematic
SERDP	-	Strategic Environmental Research and Development Program

T_p	-	Peak wave period
T_s	-	Flow duration
U	-	Maximum cross-shore velocity at breaker zone deployment location
U_m	-	Cross-shore munition velocity
UnMES	-	Underwater Munitions Expert System
USA	-	United States of America
USCG	-	United States Coast Guard
UTM	-	Universal Transverse Mercator
UXO	-	Unexploded Ordnance
V	-	Volt
VA	-	Virginia
V_m	-	Munition volume
a_1, b_1	-	Coefficients in empirical relationship (equation 7)
a_2, b_2	-	Coefficients in empirical relationship (equation 8)
a_3, b_3, c_3	-	Coefficients in empirical relationship (equation 20)
a_4, b_4, c_4, d, e	-	Coefficients in empirical relationship (equation 21)
a_5, b_5, c_5, d_5	-	Coefficients in empirical relationship (equation 22)
d_i	-	Munition distance traveled from time increment i-1 to i
d_x	-	Total cross-shore munition travel distance
d_y	-	Total alongshore munition travel distance
$d_{x,i}$	-	Cross-shore munition distance traveled from time increment i-1 to i
$d_{y,i}$	-	Alongshore munition distance traveled from time increment i-1 to i
d_{50}	-	Median grain diameter
f_w	-	Friction factor for bed shear stress calculation
g	-	Gravitational acceleration
h	-	Water depth
m	-	Mass
r^2	-	Squared correlation coefficient
s	-	Total munition travel distance
t	-	Time
tanβ	-	Beach slope
u	-	Nearbed cross-shore velocity
u_b	-	Backwash velocity
u_u	-	Uprush velocity
x, y, z	-	Local coordinate system
x_{CG}	-	Munition axial center of gravity
x_m, y_m, z_m	-	Local munition coordinate system
Δd_x	-	Incremental distance traveled by a munition from time t_{i-1} to t_i
Δz	-	Elevation change
α	-	Angle between photocell sensors on the 155-mm munition
γ	-	Munition heading
θ	-	Shields number
θ_m	-	Mobility number
$\theta_{m,mod}$	-	Modified mobility number
ξ	-	Iribarren number
ρ_m	-	Munition bulk density

ρ_s - Sediment density
ρ_w - Water density
τ_b - Bed shear stress
φ - Cumulative angle of rotation
φ_{roll} - Instantaneous munition orientation relative to x_m
φ_{gyro} - Instantaneous munition angular velocity around x_m

Keywords

Munitions
Surrogate Munitions
Inert Munitions
In Situ Sensors
Munitions Sensors
Mobility
Burial
Migration
Swash Zone
Foreshore
Sediment Transport

Acknowledgements

We would like to thank government employees Gene Fabian and Seth Lyter and contractors Carl Johnson, Carl Cramer, John Wertsch and Rick Fling for their assistance with LWE1 and LWE2 conducted at the Aberdeen Test Center Littoral Warfare Environment. Jonathan Harp of CHPT Manufacturing assisted in the design and was responsible for the fabrication of the surrogate munitions. Numerous researchers assisted during the studies: Ramy Marmoush, Peter Tereszkiewicz, Jose Carlos Pintado-Patino, Ryan Mieras, Douglas Krafft, Patricia Chardon-Maldonado, Matthew Doelp, Yeulwoo Kim, Michaela Maguire, David Polakoff, Stephen Napoli, Emily Robison, Nancy Zhou, Soupy Dalyander, Tim Nelson, Katherine Anarde, Stanford Borrell, Shannon Brown, Edward Cruz, Alex Ferencz, Caroline Ferreira, Benedict Gross, Michael Larner, Laura Lopez, Marcel Krause, Maro Pontiki, Daniel Posanski, Peter Rivera Casillas, Jantine Rutten, Rachel Schaefer, Janelle Skaden, Benjamin Tsai, Jose Clemente Tuz Pech.

Abstract

Introduction and Objectives: The presence of unexploded ordnance (UXO), or munitions, in nearshore and other underwater environments is a worldwide concern due to the past military activities. UXOs have been found in the surf zone and on populated beaches, posing a risk for the public. Behavior of munitions located on the sea bed is poorly understood. The goal of this project was to design and fabricate instrumented surrogate munitions for use in large-scale laboratory and field experiment to investigate UXO burial and migration under a range of forcing conditions. We seek to understand the processes that lead to UXO migration and what processes might lead to a munition being located on the beach face.

Technical Approach: Instrumented surrogate munitions were designed and fabricated to match physical properties for a variety of common munitions. Munitions instrumentation, when internal volume capacity allowed, consisted of internal motion units for estimating migration and orientation, pressure transducers for estimating water depth and wave arrival, and passive photocells for estimating UXO burial. Extensive large-scale laboratory and field experiments were conducted at the Littoral Wafare Environment (LWE) outdoor wave flume (LWE1; 1:16 foreshore slope, LWE2 1:10 slope), Aberdeen, MD and at the NASA Wallops Flight Facility Wallops Island, VA respectively. In situ measurements of fluid velocity, water depth and sediment concentration were made at multiple cross-shore locations. Imaging systems were used for redundant measurement of fluid processes and to track munitions when visible. Munitions positions and beach morphology were collected using a precision GPS system. Dimensionless forcing parameters related to munitions processes were estimated from the acquired data and used to investigate relationships with the observed munitions migration and burial.

Results: Migration distances for proud munitions initiated in the swash zone were greatest for the steeper foreshore slope study. Under similar forcing conditions, lower density munitions migrated farther offshore than higher density munitions. Munition migration mimicked wave runup with net offshore transport. Breaker zone munitions experienced episodes of onshore- and offshore-directed motion without preferred direction. Denser munitions were observed to bury deeper, up to 2 munition diameters. Moderate correlation was observed between burial (r^2 = 0.45) or migration (r^2 = 0.37) with dimensionless parameters (such as Shields parameter, Keulegan-Carpenter number, and object mobility number), attributed to the high variability in munition response even under similar offshore forcing conditions. Forty-four percent of the field observations showed only burial and no migration. Migration in the field occurred with preferred directions being seaward (71%). Maximum onshore and offshore migrations were 10.3 and 17.9 m, respectively. Munition burial was also influenced by far-field processes with maximum burial between surveys of up to 10 munition diameters.

Benefits: Data on munitions migration and burial and associated environmental conditions are perhaps the first extensive measurements in prototype scale swash zones. The study provides information on burial and migration characteristics under a wide range of forcing and munitions types (caliber and density) and attempts to relate those processes to commonly used dimensionless numbers. These data and relationships are needed to validate probabilistic models of munitions migration and burial near the shoreline. The study additionally provided robust design characteristics for a variety of munition surrogates, the use of a variety of commercial internal sensor for munitions attitude, and a new sensor array for estimating munition burial.

Executive Summary

Introduction: Munitions exist on the sea floor as a result of past military activities. These munitions can cause environmental issues as well as pose a danger to receptors that may come into contact with the munitions. Of particular concern is the potential for munitions to migrate or change their burial status. Munition characterization (mobility, exposure, burial) is perhaps most important in shallower water where there is a higher density of potential receptors and increased magnitude of forcing conditions. Some prior work has focused on the shoaling and surf zones (Figure 1). The work described herein focuses on the inner surf and swash zones where data on munitions processes are lacking.

Objectives: The objective is to quantify the hydrodynamic processes (velocity, shear stress, dimensionless forcing parameters) and associated munitions mobility (burial, exposure, transport). Extensive large-scale laboratory and field experiments using a wide array of in situ sensors, remote sensors and sensor-enabled surrogate munitions were conducted. We hypothesize that munition characteristics such as size, shape and density must play a vital role in mobility and several surrogate munitions spanning the parameter space were designed and constructed. The research addresses questions such as:

1) Does a munition that is stranded on the beach face (from dune erosion, excavated in place or delivered via transport from seaward), scour in partially, bury, or become transported offshore?
2) Does a munition that nears the shoreline reach the beach face or remain offshore?
3) How are the answers to 1-2 governed by forcing conditions and munition characteristics?
4) Do surrogate and inert munitions behave similarly under the same forcing conditions?
5) Can a simple force balance be used to determine munitions mobility on beaches?

Technical Approach: Instrumented surrogate and inert munitions (the latter provided by the SERDP repository from Aberdeen, MD) were used in large-scale laboratory and field experiments. Surrogates were designed and fabricated that have nearly the same physical characteristics of actual munitions. Actual munition physical properties (target values) were obtained and cataloged through measurements of inert munitions and/or identified in military reports. Actual munition shapes were then split into individual parts with different material density. Surrogate parameters (mass, body density, center of gravity, and axial moment of inertia) were calculated and compared with the target values. Materials and sizes of individual parts of the surrogate were modified to minimize differences between surrogate and target values to less than 20%. The smallest surrogates, 20-mm and 40-mm rounds do not have volume capacity for internal devices (Figure ES1). The BLU-61 Cluster Bomb, due to its size, only housed an inertial motion unit (IMU) for heading and roll, centered with the surrogate centroid. The Rocket and 155-mm have the capability for water depth measurements using a pressure transducer (PT). Lastly, the 155-mm surrogate has sufficient capacity to house the IMU, PT, and an array of photocells for estimating burial depth.

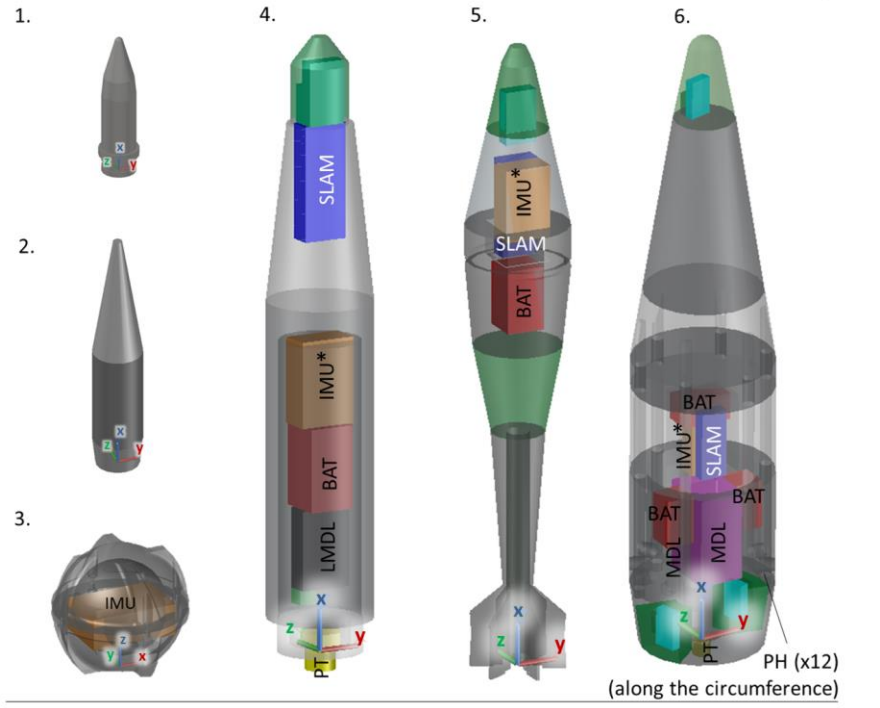

Figure ES1. Smart surrogate munitions designed using AutoCAD: 1) 20-mm round; 2) 40-mm round; 3) BLU-61 cluster bomb; 4) Hydra Rocket; 5) 81-mm mortar; 6) 155-mm Howitzer. Surrogates are shown with internal devices. Body part color identifies different material: light grey = 6061-T6 aluminum, dark grey = 304/304L stainless steel and green = 20% glass filled Delrin.

Large-scale laboratory experiments (June 2016 and November to December, 2016) were conducted in the Littoral Warfare Environment (LWE) outdoor flume in Aberdeen, MD (Figure ES2). The flume is 100 m long, almost 30 m wide, and permitted munitions testing in near-prototype conditions. The beach profile was composed of median diameter, d_{50} = 0.33 mm, sand. The two experiments were largely distinguished by the initial foreshore slope; 1:16 for test LWE1 and 1:10 for test LWE2. The experimental area (delimited by the black box in Figure ES2A) spanned several meters either side of the still water shoreline (white dash-dot line). Instrumentation and munitions were largely confined to the experimental area (Figure ES2B). A frame consisting of scaffolding pipes was installed across the profile for deploying sensors to record velocity and water depth. Two cameras, one on the flume wall and another on the frame, were used to record video imagery of runup and munition migration. An additional underwater camera was deployed on the frame to detect qualitatively information of munition motion.

A real time kinematic (RTK) GPS system was used to survey munitions position pre- and post-run, sensor positions, and record beach morphology changes. Munition sensors were initialized to record at the beginning of each day to avoid opening/closing operations of munition shells between runs. In situ sensors and the cameras were cabled and connected to a series of time-synchronized laptop computers located in a command trailer landward of the maximum runup line. Waves were run in bursts of 2.5, 5, or 10 minutes for a total of 58 runs. Forcing conditions at LWE were defined using Monochromatic (M), Jonswap (J), or Pierson-Moskowitz (PM)

spectra, the significant wave height ranging from 0.2 and 1.1 m and the peak wave period ranging from 3 to 9 s. Nearly all possible combinations were tested during the two studies with choices made in an effort to minimize large morphological changes. Swash zone munitions were deployed / re-deployed along the shoreline at the beginning of each run spanning roughly 9 m between the instrument frame and flume wall. This wide area allowed the deployment of multiple munitions at the same time. Position, orientation, and burial status were recorded for each munition pre- and post-run.

The instrumentation set up was similar for the field experiment conducted at the NASA Wallops Flight Facility (August to October, 2018). In situ data were collected continuously except for battery swapping and data download. Waves in the field were typically less than 1 m in August and greater than 1 m for the other months. Two major storm events occurred, a tropical storm (Sep 8th – Sep 9th) followed by hurricane Florence (Sep 11th – Sep 14th) with a maximum significant wave height of 3.3 m. Over 50 munitions were deployed at the beginning of the experiment within a U-shaped fenced area that spanned 60 m in the alongshore and 60 m in the cross-shore in an effort to keep munitions corralled to a local area. Munitions positioning was performed when possible at low tides. Additional munitions deployment in front of the underwater camera were conducted for single event force analysis cases.

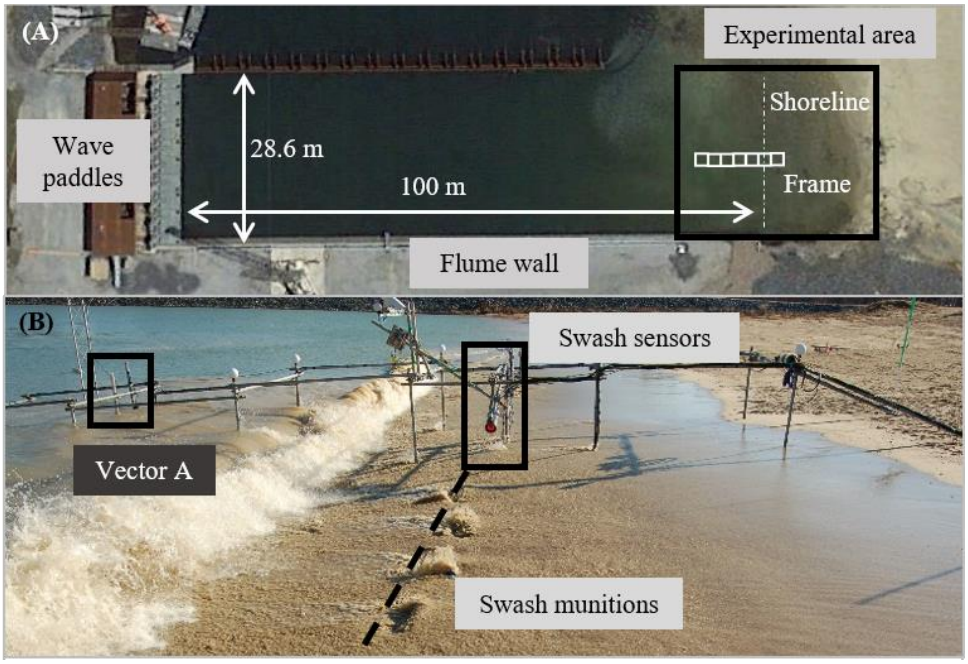

Figure ES2. A) Littoral Warfare Environment (LWE) large-scale outdoor flume located at the Aberdeen Test Center in Aberdeen, Maryland, USA (Google Earth). Shoreline depicted in the image is the shoreline location during the experiment but does not match the available satellite imagery. B) Picture of the experimental area.

Results and Discussion: Relationships between burial depth observed for cases of no migration (98) and dimensionless numbers for LWE studies were investigated. The two most common dimensionless numbers related to munitions burial are the Shields number, θ, as a ratio between destabilizing and stabilizing forces and the Keulegan-Carpenter number, *KC*, as a ratio between drag and inertia forces. The color separation in Figure ES3 indicates the different experiments and thus the foreshore slope (milder slope in red tones for LWE1, steeper slope in blue tones for LWE2). The color gradient provides a representation of munition density. Sixty-four of the 98 cases occurred on the milder slope where less migration was observed. The munition density is clearly important considering denser munitions, especially for the milder slope experiment (LWE1) showed greater relative burial, B/D_m, where B is the burial depth and D_m is the munition diameter.

Past efforts by SERDP and other researchers suggest dimensionless equilibrium burial may follow a power law relationship of the form

$$B/D_m = a_1\theta^{b_1}, \quad \text{(ES1)}$$

where a_1 and b_1 are fitting coefficients. There is a high level of scatter in the data (Figure ES3A). The highest correlation with the swash zone data relative burial data were for $a_1 = 0.47$ and $b_1 = 0.29$ but r^2 was only 0.05, suggesting the Shields number is a poor predictor of relative burial in the swash zone.

Previous research also suggested a power law relationship for dimensionless burial related to KC as

$$B/D_m = a_2(KC)^{c_2}, \quad \text{(ES2)}$$

where a_2 and c_2 are fitting coefficients. The two lines in Figure ES3B were identified previously for cylinders ($a_2 = 0.1$; $c_2 = 0.51$) and frusta ($a_2 = 0.0077$; $c_2 = 0.78$) for equilibrium burial of fully submerged objects subjected to wave forcing. Swash zone observations fall between the two empirical relationships even though they are intermittently submerged and do not reach equilibrium burial. Coefficients $a_2 = 0.09$ and $c_2 = 0.43$ were found for the observed dimensionless burial depths with an r^2 of 0.39; commensurate with correlations found in previous studies. The moderate correlation suggests roughly 40% of the observed dimensionless burial variance can be explained by the relationship to KC.

Morphological changes may be one reason the correlations between dimensionless burial depth and forcing parameters are low to moderate. A comparison was conducted between the relative burial achieved by the munition at the end of the run and the normalized beach profile changes, $\Delta z/D_m$, occurring within the run (Figure ES3C). The majority of the data had relative burial greater than 0 as most of the munitions were deployed proud. A $\Delta z > 0$ (< 0) indicates accretion (erosion) had occurred. The first quadrant ($\Delta z > 0$ and positive burial) indicates foreshore

accretion and munition burial. If the burial processes were governed solely by the beach morphology changes, the data would exist along the 1:1 line (accretion = burial depth).

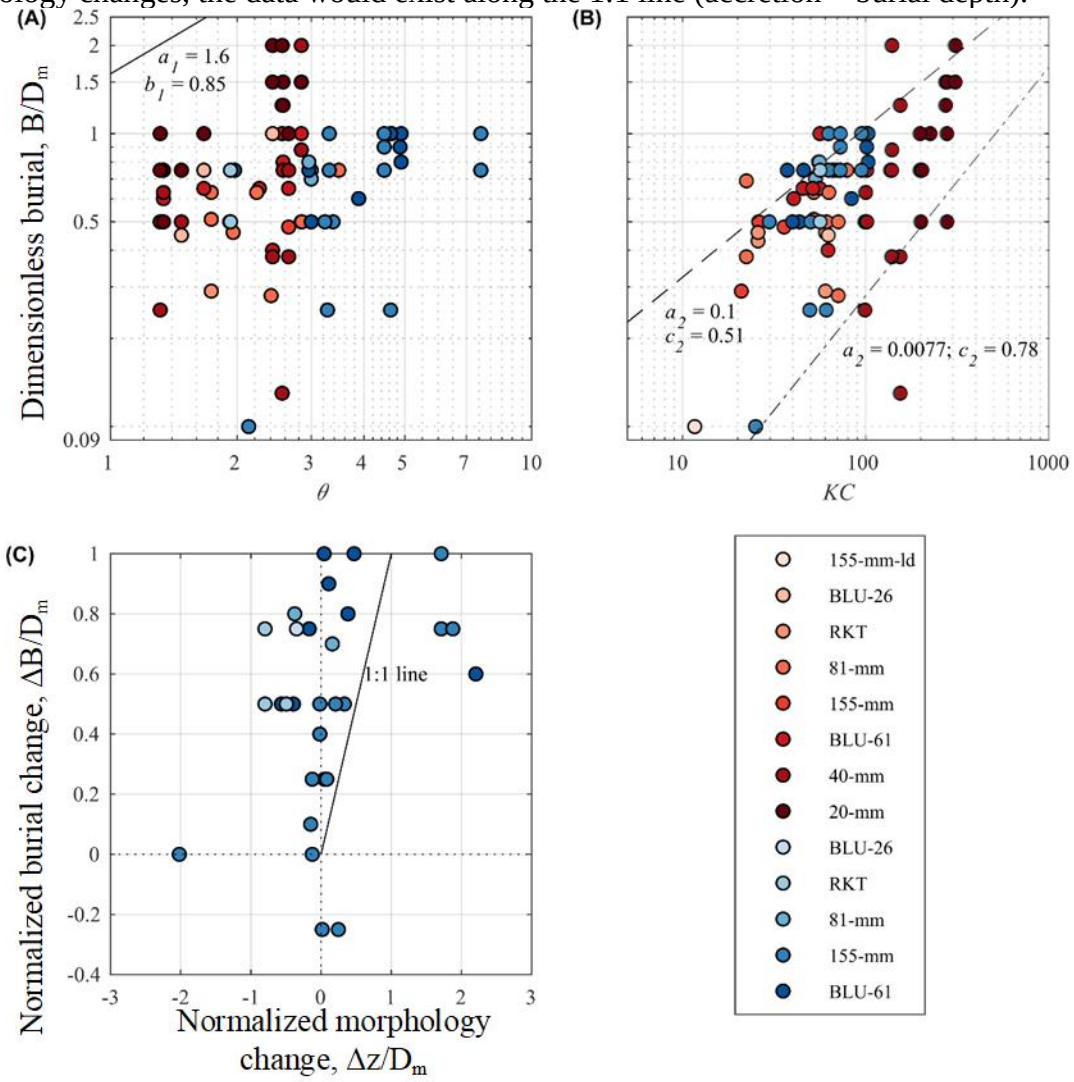

Figure ES3. Post-run dimensionless burial depth observations as a function of Shields number (A) and the Keulegan-Carpenter number (B) for swash zone deployed munitions of the no migration cases. C) Dimensionless burial (difference in burial between two runs) as a function of the dimensionless beach morphology change. Color separation is relative to the foreshore steepness (red slope = 1:16, blue for slope = 1:10). Color gradients indicate munition density with lighter color corresponding to less dense objects. Lines (A and B) represent different relationships from the literature with corresponding coefficients a_1 and b_1 and a_2 and c_2.

However, the observations are mostly located above the 1:1 line suggesting that the munition burial on the foreshore is governed additionally by local scour processes. Even when the foreshore eroded ($\Delta z < 0$), munitions experienced burial, further indicating the importance of local scour processes. Correlations between dimensionless burial and forcing conditions improves by roughly 20% by including additional parameters beyond θ and KC. However, the

small increase in correlation must be weighed against the inclusion of up to three additional fitting parameters.

Analyses were conducted for the motion group (Figure ES4; 100 cases for the steeper slope and 49 cases for the milder slope). Most of the mobility (69%) was offshore-directed (positive distance) with some onshore-directed motion for a range of munitions bulk density. The largest offshore migration (15 – 20 m) occurred for the 155-mm-ld (munition density = 2115 kg/m^3) on the milder sloping foreshore. Interestingly, some 155-mm-ld also migrated onshore yielding the three largest onshore directed migrations observed of 2.5, 4.3 and 5.1 m. In contrast, the similarly shaped 155-mm (munition density = 4230 kg/m^3) had average offshore migration distances of only 0.1 m regardless of forcing or slope conditions. There was an exception where one 155-mm migrated offshore 4.2 m under the most intense forcing conditions but another 155-mm deployed initially at the same cross-shore position migrated only 0.14 m. No 155-mm were observed to migrate onshore. These findings suggest that 1) munitions response will be varied even under the same munition characteristics and forcing conditions; and 2) less dense munitions more easily migrate whereas more dense munitions migrate shorter distances or bury in place.

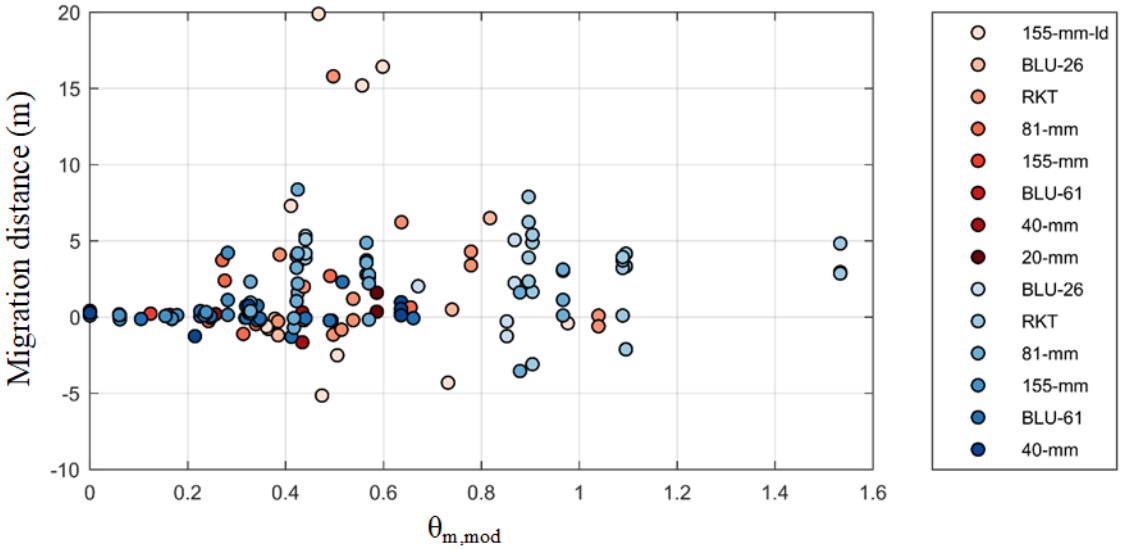

Figure ES4. Cross-shore migration measured post-run as a function of the modified object mobility number for swash zone deployed munitions of the motion cases. Color separation is relative to the foreshore steepness (red for milder slope = 1:16, blue for steeper slope = 1:10). Color gradients indicate munition density with lighter color corresponding to less dense objects.

Comparisons for migration were also made against a modified object mobility number, $\theta_{m\,mod}$, that relates the velocity squared to gravity, diameter, and the excess munition density. An extra factor is included in $\theta_{m\,mod}$ to account for initial burial depth variations between 0 (100% or more initial burial) and 1 (0% initial burial). The maximum object mobility number observed was 1.53. However, the majority of the munition motion occurred for had $\theta_{m\,mod} < 1.09$. Under equal conditions a larger object mobility number should indicate a larger potential for the object to be mobilized. The plot has considerable scatter, but denser munitions migrate shorter distances. Interestingly, different migration distances were observed under the same mobility number for the same type of munition. There is no obvious correlation between mobility number and migration distance in this study for munitions deployed in the swash zone.

Results were less conclusive for the field study due to loss of munitions and intermittent surveying. Of the 129 munition surveys, 56% showed migration with cross-shore being the dominant direction. Maximum seaward migration was 17.9 m and maximum landward migration was 10.3 m. Munitions also migrated preferentially to the south due to the local wave climate with a maximum travel distance of 21 m (note that this munition would have travelled farther but was impeded by the retaining fence). The no migration burial cases (44%) experienced some burial depths up to 10 munition diameters indicating far-field processes were often more responsible for burial than local scour. There were no clear trends between incremental migration distance and the mobility number. The total migration distance in the backwash was only moderately correlated ($r^2 = 0.45$) to the integrated mobility number. Force balance analysis proved difficult (a torque analysis should also be considered) but indicated drag and friction are the dominant forces. Separate calculation of the impact force yielded magnitudes two to three times the drag force.

Implications for Future Research and Benefits: Data on munitions migration and burial and associated environmental conditions are perhaps the first extensive measurements in prototype scale swash zones. The study provides information on burial and migration characteristics under a wide range of forcing and munition types (caliber and density) and attempts to relate those processes to commonly used dimensionless numbers. These data and relationships are needed to validate probabilistic models of munitions migration and burial near the shoreline. The study additionally provided robust design characteristics for a variety of munition surrogates, the use of a variety of commercial internal sensor for munitions attitude, and a new sensor array for estimating munition burial.

Approximately 30% of the munition cases had onshore-directed migration when the munition was placed proud initially. Proud placement presents the best possible case for onshore-migration and suggests that partially buried or buried munitions are unlikely to be exhumed and migrate onshore. Instead, offshore-migration may occur if the munition becomes exposed to the flow especially on steeper foreshores. However, munitions with density greater than roughly 4000 kg/m^3 tended to bury rather than migrate suggesting that most intact munitions are not likely to migrate long distances onshore. Offshore migration, however, could occur if again the munition becomes exposed to the flow. Poor to moderate correlation between dimensionless forcing parameters and observed migration and burial indicates that the parameters alone may be insufficient to predict munitions processes *and* that perhaps the number of iterations tested was insufficient to fully explore potential relationships. That is, the large variability in the burial and migration of munitions is due to the numerous parameters and factors that must play a role in their behavior. Additional data are required to enlarge the swash zone observations dataset for munition mobility and burial. Long-term investigations using numerous munitions of the same type and with density variations performed in controlled environments may help to narrow the important parameters and forces important for burial and migration.

1 Objective

Munitions exist on the sea floor as a result of past military activities. These munitions can cause environmental issues as well as pose a danger to receptors that may come into contact with the munitions. Of particular concern is the potential for munitions to migrate or change their burial status. Munition characterization (mobility, exposure, burial) is perhaps most important in shallower water where there is a higher density of potential receptors and increased magnitude of forcing conditions. Some prior work has focused on the shoaling and surf zones (Figure 1). The work described herein focuses on the inner surf and swash zones where data on munitions processes are lacking. The objective is to quantify the hydrodynamic processes (velocity, shear stress, dimensionless forcing parameters) and associated munitions mobility (burial, exposure, transport). Extensive large-scale laboratory and field experiments using a wide array of in situ sensors, remote sensors and sensor-enabled surrogate munitions were conducted. We hypothesize that munition characteristics such as size, shape and density must play a vital role in mobility and several surrogate munitions spanning the parameter space were designed and constructed. The research addresses questions such as:

6) *Does a munition that is stranded on the beach face (from dune erosion, excavated in place or delivered via transport from seaward), scour in partially, bury, or become transported offshore?*
7) *Does a munition that nears the shoreline reach the beach face or remain offshore?*
8) *How are the answers to 1-2 governed by forcing conditions and munition characteristics?*
9) *Do surrogate and inert munitions behave similarly under the same forcing conditions?*
10) *Can a simple force balance be used to determine munitions mobility on beaches?*

1.1 SERDP Relevance

The research described here is in direct response to the Statement of Need for the Munitions Response (MR) Program Area, that calls for studies related to (1) assessing the environment for which munitions are found, and (2) environmental conditions, especially sediment type and hydrodynamic conditions, that are used to predict munition mobility and burial. To our knowledge, all previous and current SERDP funding related to the nearshore focused in regions that are continually submerged. This effort is unique in that it seeks to understand munition mobility and processes controlling mobility in the region of the nearshore that is intermittently submerged (Figure 1). Results from this effort will assist stakeholders focused on site remediation and management in understanding munitions mobility as it nears and/or reaches the beach face. These data are needed to assess the potential for munitions to remain in place, migrate landward/seaward, and or migrate into previously cleared areas. The acquired data and results are also needed to enhance probabilistic and process-based models being developed by SERDP researchers for predicting the potential for migration, burial, and / or exposure.

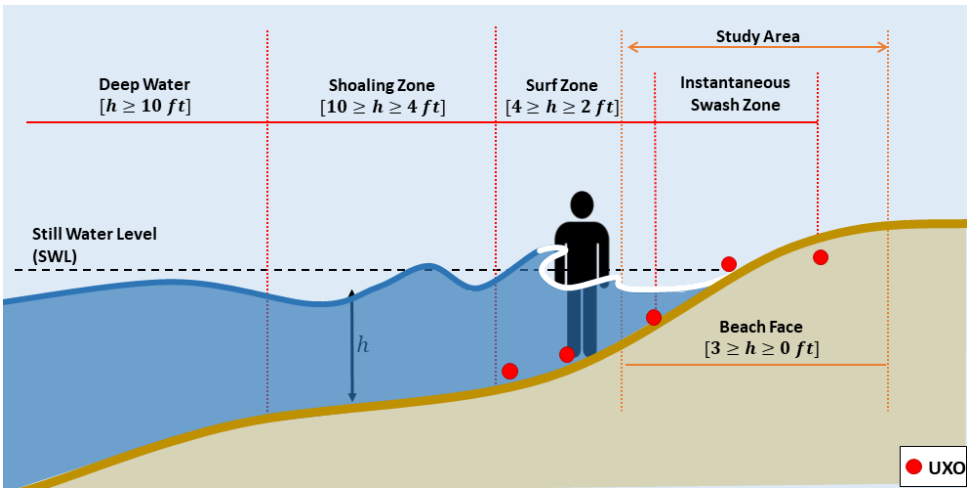

Figure 1. Schematic showing the nearshore region. The studies conducted during this work deployed surrogate and inert munitions in regions identified by the filled red circles.

2 Background

Motion and burial of objects (e.g. cobbles, cylinders, conical frusta, surrogate munitions) has been investigated for different environments, including energetic nearshore regions (Table 1). Many of the studies were conducted in small-scale wave flumes (waves with and without a superimposed current or a simple accelerating flow) or flow tunnels (under oscillatory flows). Empirical formulations between equilibrium burial depth and dimensionless numbers, such as the Keulegan-Carpenter number, the Shields parameter and the object mobility number were identified (Cantano-Lopera et al., 2011, 2007; Demir and García, 2007; Friedrichs et al., 2016a; Rennie et al., 2017; S.I. Voropayev et al., 2003). Initiation of motion was investigated through laboratory experiments identifying the critical object mobility number of underwater cylinders as a function of the ratio between object diameter and bed roughness (Rennie et al., 2017). Field studies of surrogate munitions in the surf zone (Traykovski and Austin, 2017) and seaward of the surf zone (Calantoni, 2014) have recognized munition density as an important quantity for determining munition mobilization (densities lower than saturated sediment density) or no mobilization (higher densities).

The majority of the aforementioned studies were conducted in the surf zone or deep water or in oscillatory flow tunnels where the object is continuously submerged. There is a lack of knowledge of munition processes in the swash zone; the portion of the beach where flows intermittently inundate the beach face. The swash zone is highly energetic/dynamic and swash processes are different than those occurring in the other regions of the nearshore. The motion of cobbles in the swash zone was studied in the laboratory using a dam-break mechanism over a solid, impermeable sloping bottom (Luccio et al., 1998). In particular, cross-shore displacement was measured for different cobble characteristics (density, size, shape) and different forcing conditions. A theoretical model was implemented and compared with the results obtained from the experiment. Collection of data in the swash zone over a permeable, mobile bed which include the scour/burial processes and interaction of the object with the bottom have been accomplished in a more recent laboratory study (Gross and Puleo, 2019). However, no field or large-scale laboratory data on munitions processes in the swash zone, to the authors' knowledge, have been collected.

Table 1. Experimental efforts on burial and motion of underwater objects.

Authors	Experiment type	Tested objects	Focus	Region	Bottom type
(Luccio et al., 1998)	Laboratory: Dam-break scenario	Cobbles	Motion	Swash zone	Smooth and rough impermeable sloping beach
(Voropayev et al., 2001)	Laboratory: Large wave tank	Cobbles	Motion	Surf zone	Rough impermeable sloping beach
(S. I. Voropayev et al., 2003)	Laboratory: Large wave tank	Cylinders	Scour, burial	Nonlinear progressive shoaling waves	Sandy sloping beach
(S.I. Voropayev et al., 2003)	Laboratory: Large wave tank	Cobbles	Motion, burial	Surf zone	Sandy sloping beach with bedforms
(Cantano-Lopera et al., 2007)	Laboratory: large oscillating water-sediment tunnel, large wave-current tank	Cylinders	Burial	Oscillatory flow & waves and currents	Sandy flat bed
(Demir and García, 2007)	Laboratory: large oscillating water-sediment tunnel	Cylinders	Burial	Oscillatory flow	Sandy flat bed
(Cantano-Lopera et al., 2011)	Laboratory: Large wave-current flume	Conical frusta	Scour, Burial	Waves and combined flow	Sandy flat bed
(Calantoni, 2014)	Field	Surrogate munitions	Burial, Motion	Outside surf zone	Sandy
(Traykovski and Austin, 2017)	Field	Surrogate munitions	Burial, Motion, re-exposure	Surf zone	Sandy
(Friedrichs et al., 2016a)	Synthesis of observations	-	Burial	-	-
(Rennie et al., 2017)	Laboratory: closed loop recirculating flow channel	Cylinders	Burial, initiation of motion	Currents and waves, accelerating flow	Rigid bottom and sandy bed
(Gross and Puleo, 2019)	Laboratory: Dam-break scenario	Spheres	Burial, motion	Swash zone	Sandy sloping beach

Ongoing efforts are using probabilistic models to predict munitions migrations distances from their initial location and munition burial/exposure status. The Underwater Munitions Expert System (UnMES; Rennie, 2017), provides probabilities on whether a munition remains in place or migrates (either near or far from the initial position). The distance traveled is estimated as a function of the mobility number of the munition. The model relies on recent UXO mobility observations (Rennie et al., 2017; Traykovski and Austin, 2017). Other than migration, UnMES also predicts the degree of burial of munitions via relationships obtained from the scientific and engineering literature. UnMES is designed for wave-dominated climates over non-cohesive sands where bottom orbital flows are the main forcing mechanism. The model has not yet been validated for munitions status in intermittently submerged nearshore environments. Thus,

UnMES and other models for predicting munitions burial/exposure will benefit from observations of munitions processes in the swash zone.

2.1 Dimensionless Numbers Related to Burial and Migration

Two dimensionless numbers have been related to burial of pipelines or objects on a mobile bed; the Keulegan-Carpenter (*KC*) number and the Shields number (θ). The Keulegan-Carpenter number represents the ratio between drag and inertia forces as

$$KC = \frac{u\,T_s}{D_m}, \tag{1}$$

where u is the nearbed cross-shore velocity, T_s is the flow period (often wave period) and D_m is the object diameter. The Shields number indicates the ratio between destabilizing and stabilizing forces for sediment mobilization

$$\theta = \frac{\tau_b}{(\rho_s - \rho_w) g d_{50}}, \tag{2}$$

where ρ_s and ρ_w are sediment and water densities (2650 kg/m^3 and 1000 kg/m^3 respectively), g is the gravitational acceleration, and d_{50} is the median sediment diameter. The bed shear stress, τ_b, is expressed using a friction coefficient f equal to 0.03 (Puleo and Holland, 2001)

$$\tau_b = \frac{1}{2}\rho_w f u|u|. \tag{1}$$

Incipient sediment motion is normally assumed to occur for $\theta > 0.05$ (Soulsby and Whitehouse, 1997). However, munition presence on/in the bed can lead to increased bed shear stresses (Truelsen et al., 2005).

The object mobility number has been related to the object distance traveled and is defined as

$$\theta_m = \frac{u^2}{g D_m \left(\frac{\rho_m}{\rho_w} - 1\right)}, \tag{2}$$

where ρ_m is the munition bulk density. The object mobility number has also been used to study initiation of motion and identify the threshold for motion / no motion. A modified objected mobility number considering the initial burial depth, B_i, may be more appropriate for this study

$$\theta_{m\,mod} = \frac{u^2}{g D_m \left(\frac{\rho_m}{\rho_w} - 1\right)} \frac{D_m - B_i}{D_m}. \tag{3}$$

Considering that the experiments mostly occurred in the swash zone, parameters such as the foreshore slope and the runup are also considered as potentially important. The Iribarren number (Iribarren and Nogales, 1949), ξ, providing the ratio between the foreshore slope ($tan\beta$) and the offshore wave steepness, is

$$\xi = \frac{tan\beta}{\sqrt{\frac{H_s}{L_0}}} = \frac{tan\beta}{\sqrt{\frac{2\pi H_s}{gT_p{}^2}}}, \quad (4)$$

where H_s is the significant wave height, L_0 is the offshore wave length, and T_p is the peak wave period. The Iribarren number provides an indication of the type of beach, either dissipative ($\xi <$ 0.5, milder beach slope) or reflective ($\xi >$ 3.3, steeper beach slope) (Dean and Dalrymple, 2002).

Past efforts (Cataño-Lopera et al., 2007; Demir and García, 2007; Friedrichs et al., 2016a) suggest a power law relationship for dimensionless equilibrium burial of the form

$$B/_{D_m} = a_1\theta^{b_1}, \quad (7)$$

where a_1 and b_1 are fitting coefficients. Typical values for (a_1, b_1) are (1.2, 0.33), (0.97, 0.33), (13, 1) and (1200, 2.4) depending on D_m and munition shape for lab and field data of objects constantly submerged and in the presence of steady current and no waves (Friedrichs et al., 2016a). Objects subjected to oscillatory flow or wave and/or combined flow conditions yielded b_1 = 0.8 (Cataño-Lopera et al., 2007; Demir and García, 2007).

Previous research (Cataño-Lopera et al., 2011; Friedrichs et al., 2016a; Sumer and Fredsøe, 2001) also suggest a relationship of the form

$$B/_{D_m} = a_2(KC)^{c_2}, \quad (8)$$

where a_2 and c_2 are fitting coefficients with values for cylinders (a_2 = 0.1; c_2 = 0.51) and frusta (a_2 = 0.0077; c_2 = 0.78) for equilibrium burial of fully submerged objects subjected to wave forcing reported by (Friedrichs et al., 2016a). Similar coefficients were also found by Sumer & Fredsøe (2001) for fixed pipelines subjected to waves and currents and by Cataño-Lopera et al (2011) for frusta in waves alone and combined flow. Additional empirical formulations can be arranged by collecting more dimensionless parameters. Furthermore, empirical formulations for migration distance as a function of various parameters can be tested.

2.2 Force Balance and Surge Force

The migration and burial of a munition on the beach face from hydrodynamic forcing is a complex process. The complexity is attributed multiple factors. First, the sandy bed represents a permeable and mobile surface, which interacts with the munition. Second, scour processes may dominate owing to bed irregularities and flow variation around the munition. Third, the physical properties of the munition, such as shape, density, dimensions, and roughness of the external surface, alter transport and burial characteristics. Orientation of the munition relative to the flow direction is also important. Fourth, flow characteristics including varying water depths, fluid acceleration and turbulence add more complexity to the problem. A main difficulty is that while the munition moves, the parameters that govern the motion vary in time and may be difficult to estimate. The munition can migrate by rolling, sliding or by saltation; with saltation the least likely.

Migration formulations can be envisioned through a summation of torques or forces acting on the munition. Here, the work of Luccio et al. (1998) is adopted with the forces applied to a munition resting on a sloping as (see schematic in Figure 2 for uprush and backwash motion): the munition acceleration force F_{macc}; the flow acceleration force F_{facc}; the drag force F_d; the buoyancy force F_b and the friction force F_f. A perfect force balance for the case of a munition migrating indicates that F_{macc} equates to the sum of all the other forces

$$F_{macc} = F_{facc} + F_d + F_b + F_f. \tag{9}$$

Each force is expressed as:

$$F_{macc} = (\rho_m + \rho_w C_m)\, V_m\, \frac{du_m}{dt}, \tag{10}$$

$$F_{facc} = (1 + C_m)\, \rho_w\, V_m\, \frac{du}{dt}, \tag{11}$$

$$F_d = \frac{1}{2} C_d\, \rho_w\, D\, L\, |u|u, \tag{12}$$

$$F_b = \begin{cases} (\rho_m - \rho_w)\, V_m\, g\, sin\beta \quad for\ h \geq D_m, \\ \left(\rho_m V_m - \rho_w \pi \frac{h^2}{4} L\right) g\, sin\beta \quad for\ h < D_m, \end{cases} \tag{13}$$

$$F_f = C_f\, V_m\, (\rho_m - \rho_w)\, g\, cos\beta, \tag{14}$$

where C_m, C_f and C_d are the coefficients of added mass, friction, and drag, V_m is the munition volume, u_m is the cross-shore munition velocity, L is the munition length, and h is the water level. The drag force assumes the munition is oriented perpendicular to flow; the case for the force balance analysis undertaken in this work. If the munition remains motionless, the sum of the stabilizing force is greater than the destabilizing force and there is no balance.

Swash events contain two phases: uprush and backwash. During uprush, the flow runs up the beach slope and, if the munition is mobilized, it travels up the slope by the flow against gravity. During backwash, the flow runs down the slope and, again, if the object is mobilized, it will move down slope in conjunction with gravity until stopping completely in its final position. Due to the presence of a mobile bed, an extra term could be incorporated into the force balance; the suction force. The suction force acts as an additional stabilizing force that inhibits munition mobilization. The suction force arises from pressure that the munition weight exerts on the mobile bed while partially embedded and the inability for fluid to rapidly infiltrate when the munition is lifted with some vertical component from its partial burial. However, the suction force is less studied in non-cohesive sediments and extremely difficult to estimate. In addition, the force balances were tested for initially proud munitions where the suction force would be small. Therefore, the suction force will be assumed to be already included in the friction force.

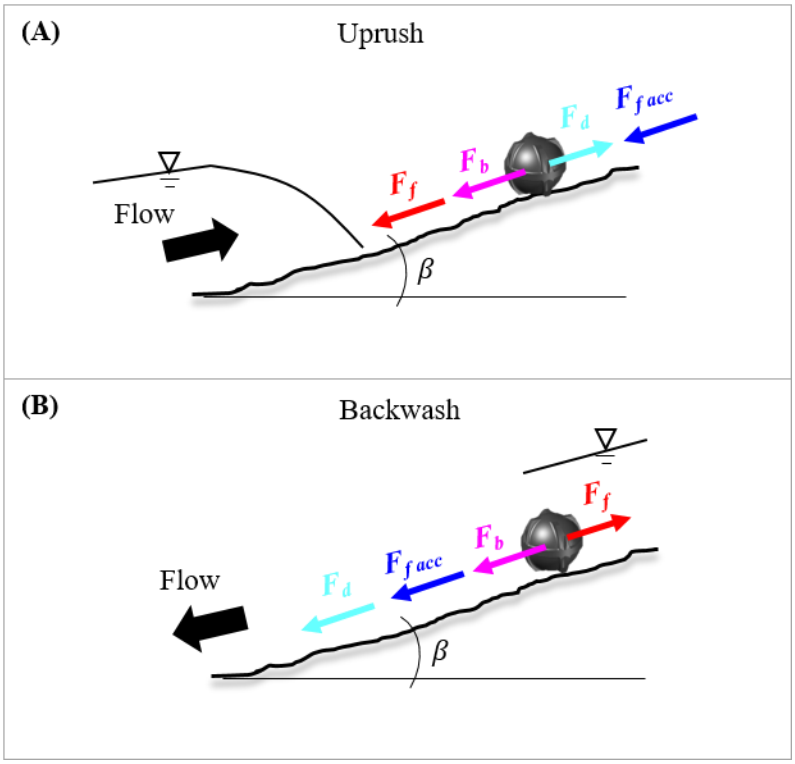

Figure 2. Schematic of the forces applied on a munition resting on a sloping bed during a swash event, uprush (A) and backwash (B).

A different term can be described if the interest is the initiation of motion of munitions in the swash zone; the impact (also called surge) force from the incoming uprush. Considering that the munition, prior the swash event, is not-submerged, the transfer of momentum from the fluid to the munition may be expressed as

$$F_i = \rho_w u^2 h L + \frac{1}{2}\rho_w g h^2 L, \quad (15)$$

where the momentum flux transferred from the flow to the munition acts on the area of impact (h by L if the munition is oriented with the long axis perpendicular to the flow and $h < D_m$. Otherwise h is replaced by D_m in equation 15). The first term represents the dynamic force and the second term the hydrostatic force. The impact force has been used in tsunami debris interaction studies (Yeh, 2006) and likely applies for only a short period of time (Nandasena and Tanaka, 2013) on the order of 0.5 s or less.

3 Materials and Methods

3.1 Surrogate Munitions and Embedded Sensors

Eight different types of munitions were tested during the experiments: 20-mm and 40-mm Projectiles; 81-mm Mortar; BLU-26 and BLU-61 Cluster Bombs; M151-70 Hydra Rocket; and two variants of M107 155-mm High Explosive Howitzer Projectiles with the same dimensions but different bulk densities (Figure 3). Hereafter, each munition type is identified with an ID for clarity (Table 2). The selected munitions were chosen from a larger group of potential munitions in underwater environments based on discussions with a group of Strategic Environmental

Research and Development Program (SERDP) munitions mobility researchers (Calantoni, 2014). SERDP maintains a standardized target repository from which the subset list is contained.

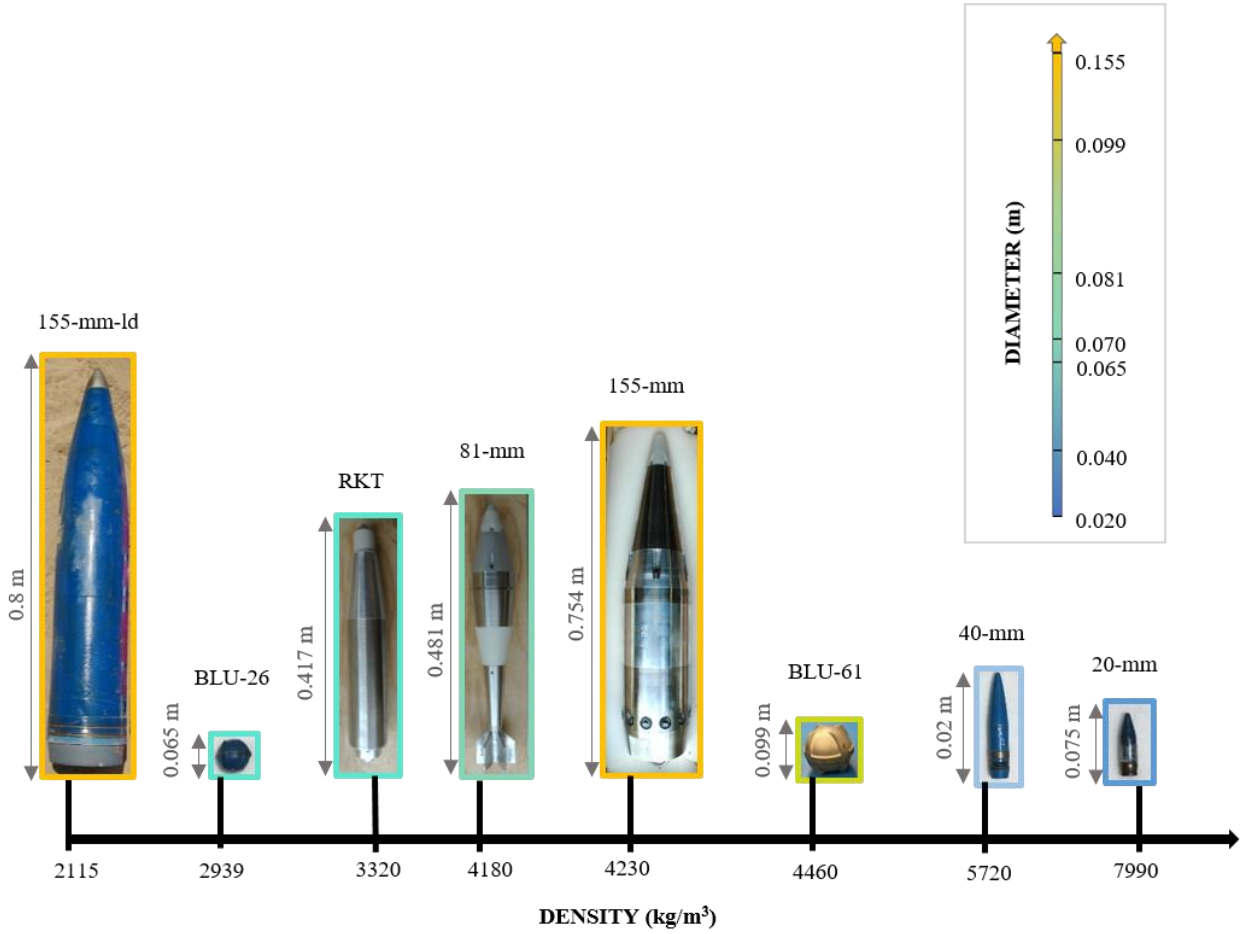

Figure 3. Munition types tested during LWE1 and LWE2 experiments (individual images are not to scale). Munition IDs (located above individual images) correspond with the actual munition names in Table 2.

Table 2. Munition ID and values of munition physical characteristics.

Munition	Munition ID	Shape	Density ρ_m (kg/m^3)	Diameter D_m (m)	Length L (m)	D_m/L
20 mm Projectile	20-mm	Cylindrical	7990*	0.020	0.075	0.266
40 mm Projectile	40-mm	Cylindrical	5720*	0.040	0.200	0.200
BLU-26 Cluster Bomb	BLU-26	Spherical	2939	0.065	0.065	1.000
BLU-61 Cluster Bomb	BLU-61	Spherical	4460*	0.099	0.099	1.000
81 mm Mortar	81-mm	Cylindrical	4180*	0.081	0.481	0.168
M151-70 Hydra Rocket	RKT	Cylindrical	3320*	0.070	0.405	0.173
155 mm High Explosive Howitzer Projectile	155-mm	Cylindrical	4230*	0.155	0.754	0.205
155 mm High Explosive Howitzer Projectile	155-mm-ld	Cylindrical	2115	0.155	0.800	0.193

* Reported values are relative to surrogates.

The eight munitions have different physical characteristics: shape; bulk density; diameter; and length (Table 3), noting that those physical characteristics may play a role in their mobility / burial. The munitions are small caliber (diameter) and cover a wide range of bulk densities 2115 - 7990 kg/m^3 and dimensions, both in length, 0.065 - 0.8 m, and diameters, 0.02 - 0.155 m. Most of the munitions have an elongated shape (referred to as cylindrical) with D_m / L ratios of 0.168 to 0.266, whereas the two Cluster Bombs are nearly spherical (D_m / L = 1), except for the raised spin-arm flutes.

The munitions used for the study are contained in two categories: inerts and surrogates. *Inert* is a real munition that is inactive (no explosive component inside). Inerts were provided by the Aberdeen Test Center (ATC) SERDP repository. The other set includes objects designed/fabricated to mimic the physical characteristics of real munitions and are referred to as *surrogate* munitions. Surrogate munitions were instrumented where possible. A detailed description of the surrogate munitions used can be found in Bruder et al. (2018). An overview of munitions fabrication and embedded sensors is provided here. Hereafter, the term *munition* will be used without regard to inert or surrogate except where necessary for clarification.

3.1.1 Surrogate munitions: design

Six out of the eight munition types were fabricated: 20-mm, 40-mm, 81-mm, BLU-61, RKT, and 155-mm. The other two types: BLU-26 Cluster Bomb and a variant of the 155-mm High Explosive Howitzer Projectile (155-mm-ld) were not replicated but still used in the inert form during the study. Two of the fabricated munitions, 20-mm and 40-mm, do not have the internal volume capacity to be instrumented.

The larger surrogate munitions were designed with the main scope of having realistic objects with the capacity to fit sensors inside their shells. The sensors are able to measure one or more of the components of the munition behavior. Quantification of the physical characteristics (e.g. length, diameter, center of mass, density, and axial moment of inertia) were made at the SERDP repository. Military manuals (Federation of American Scientists, 2017; Harms, 1978; Rogers and Celmins, 2009; Wessam and Chen, 2015) were also consulted. Three construction materials were used in combination to achieve similarity with real munitions: 20% glass filled Delrin, 6061-T6 aluminum and 304/304L stainless steel (density of 1560, 2720 and 7999 kg/m^3 respectively). Design, in AutoCAD, consisted of decomposing the munition into an array of simple geometrical shapes (cylinders, frusta, cones) to simplify the actual construction process (see Figure 4 for example munitions, AutoCAD drawings and fabricated surrogates). Errors between the physical characteristics of the surrogate and the actual corresponding munition were minimized by assigning different materials to different shapes as well as varying the shell thickness. Absolute errors of surrogate physical characteristics ranged between 0 and 16.3% (Table 3). Note that there are numerous iterations of a given real munition type depending on internal chemical composition, fabrication material and shape characteristics (Calantoni, 2017). Therefore, characteristic variation less than 20% for the particular set of munitions is deemed acceptable.

Figure 4. Example of munitions, CAD drawing, and fabricated surrogates for A) 155 mm Howitzer, B) Hydra 70 Rocket and C) 81 mm mortar. A ruler is provided for scale.

Table 3. Values of mass, center of gravity, axial moment of inertia, and total body density of real munitions (target values) and absolute errors (%) between surrogate parameters and target values.

	TARGET VALUES				SURROGATE ERRORS (%)			
	Mass m (kg)	Axial Center of Gravity from base x_{CG} (m)	Axial Moment of Inertia I_x (kg m^2)	Density ρ_m (kg/m^3)	Mass m	Axial Center of Gravity from base x_{CG}	Axial Moment of Inertia I_x	Density ρ_m
20 mm Projectile	0.098	0.0253	0.00523 10^{-3}	7260	10.19	1.76	15.12	10.19
40 mm Projectile	0.983	0.0638	0.17938 10^{-3}	5640	1.42	6.22	4.24	1.42
BLU-61 Cluster Bomb	1.477	0.0405	1.06198 10^{-3}	4940	5.56	0.00	6.95	9.67
M151-70 Hydra Rocket	4.220	0.1778	30.424 10^{-3}	3440	3.70	1.07	4.82	3.70
81 mm Mortar	4.583	0.2820	37.100 10^{-3}	4260	1.83	6.35	16.30	1.83
M107 155 mm	43.000	0.2640	1120 10^{-3}	4400	3.97	12.50	1.07	3.97

3.1.2 Migration tracking sensor

X-IO Technologies Inertial Motion Unit (IMU) is a compact, self-contained, low-cost sensor equipped with an accelerometer, a gyroscope and a magnetometer. IMU measurement capabilities include triple axis accelerations, angular velocity around each of the three axes,

Euler angles (roll, pitch and yaw), quaternion angles and rotation matrix elements. Cost effectiveness and deployment ease are key features of the IMU. The sensor is housed inside the surrogate munitions and may be connected to an external battery (internal to the munition) for extended measurements. Data are saved to an SD card. The IMU fits inside each of the surrogates capable of housing sensors. However, IMU data in this work are shown only from 155-mm, 81-mm and RKT. The near-spherical shape of the BLU-61 allows the munition to rotate around all axes, complicating the derivation of migration distance. The reference system of the IMU matches the reference system of the surrogates and is denoted as x_m, y_m, z_m where x_m corresponds to the axis that passes through the longest dimension of the munition with positive x_m pointing towards the nose of the object. The IMU is equipped with an attitude heading and referencing system (AHRS) algorithm. Thus, the heading of the munition relative to Earth may be determined based on yaw angle measurements. The intent was to derive the munition migration in the local reference system combining the temporal history of the roll and yaw measurements. IMU sampling rate during the studies was 256 Hz or 512 Hz.

3.1.3 Water depth sensor

A Measurement Specialties Pressure Transducer (PT) was installed in the 155-mm projectile and RKT surrogates. The pressure transducer measures gage pressure relative to the sealed interior of the surrogate. The PT yields water depth and timing of wave arrival relative to surrogate motion. The PT in the 155 mm is powered by a 6.6V 1900 mAh Lithium Iron Phosphate (LiFe) battery with data logged on one channel of a 7-channel Site-Log Multi Channel Data Logger from Microedge. The PT in the RKT is powered by a 7.4V 2700 mAh Lithium Polymer (LiPo) battery with data logged to a Madgetech Volt101A-15V logger.

3.1.4 Burial tracking sensor

Luna Optoelectronics TO-8 Hermetic NSL-4960 Photocell (PH) is an optical sensor that detects the amount of received light and converts it into a voltage signal. The 155-mm munitions were designed with an array of 12 photocells surrounding the circumference of the cross-section. Other surrogates did not house PH due to space constraints. Photocells are wired to 3.6 V AA sized batteries for power and then to Microedge data loggers to record data (Bruder et al., 2018). The maximum light detected from a photocell may change depending on the brightness (which varies throughout the day but also from a day to another) with higher voltages when light is more intense. Time series from the 12 photocells provide an indication of the local bed level relative to the cross-section of the munition and therefore may serve as an indicator of the temporal variability in burial. PH data were recorded at a sampling rate of 16 Hz or 10 Hz for the munitions deployed in the swash zone. Sampling rates of 1.25 Hz and 10 Hz were used for the munitions in the breaker zone.

3.2 Experimental Study Locations

Experiments were conducted in a large-scale laboratory facility in Aberdeen, Maryland and a natural beach at Wallops Island, VA.

3.2.1 Aberdeen, Maryland

Two large-scale laboratory experiments were conducted in June and November – December 2016 to observe munition response in the swash zone and the breaker zone. Both experiments were conducted at the Littoral Warfare Environment (LWE) at the ATC in Aberdeen, Maryland,

USA. The LWE outdoor flume (Figure 5) is 100 m long, almost 30 m wide, and permitted munitions testing in near-prototype conditions. The beach profile was composed of median diameter, d_{50} = 0.33 mm, sand. The sand sorting is 0.48 and is considered poorly graded. In addition, some cobbles were observed during the experimental runs. The two experiments were largely distinguished by the initial foreshore slope; $tan\beta$ = 1:16 for test LWE1 and $tan\beta$ = 1:10 for test LWE2. The foreshore profile was adjusted by ATC personnel prior to the beginning of each experiment. The profile evolved during the course of each experiment without any additional intervention from personnel.

The approach undertaken to carry out the experiments was similar for both LWE1 and LWE2. The experimental area (delimited by the black box in Figure 5A) spanned several meters either side of the still water shoreline (white dash-dot line). Instrumentation and munitions were largely confined to the experimental area (picture in Figure 5B and schematic in Figure 5C). Munitions were tested in two regions: the swash zone and the breaker zone. A frame consisting of scaffolding pipes was installed across the profile for deploying sensors. Two Nortek Acoustic Doppler Velocimeters (Vectors) were positioned in line with the breaker zone munitions (Vector A) and at the seaward end of the frame (Vector B) to record the free surface elevation and near bed flow velocity. An array of sensors was affixed to (or near) the frame in line with the munitions, in proximity of the shoreline for the swash zone measurements ("Swash sensors" in Figure 5 and more detailed configuration in Figure 6). The swash sensors include a Druck PTX1830 pressure transducer (PT) located at the bed level to measure water depths. Flow velocity was recorded by a Valeport electromagnetic current meter (EMCM) positioned initially at 0.03 m above the bed. The PT and EMCM were located at the same cross-shore and alongshore position with the PT buried in the sand below the EMCM. Two cameras, C1 (AVT Prosilica GT1920) and C2 (AVT Prosilica GC655), were used to record video imagery of runup and munition mobility. C1 was positioned on the wall of the flume providing imagery of the munition area from the side (Figure 5B), while C2 was installed on the frame aimed downward (Figure 6A) to quantify runup and the munitions motion closest to the frame. For LWE1, C2 was not deployed and C1 was positioned at the same alongshore location but more landward. An additional camera, underwater camera (UC), was deployed on the frame (Figure 6) to detect qualitatively information of munitions motion. Unfortunately, imagery of munitions underwater is obscured by the high turbidity of the water, bubbles and the presence of sediment in suspension.

A real time kinematic (RTK) GPS system was used to survey munitions position pre- and post-run, sensor positions, and the beach profile. RTK GPS data were collected in UTM zone 18 and NAVD88 vertical datum and subsequently transformed to a local *x, y, z* coordinate system. Hereafter, all morphology data are shown in the local reference *x, y, z* system (Figure 6). The horizontal origin was set at the still water line (landward far end of the flume wall) while the origin elevation was set at the initial shoreline elevation. The *x* and *y* axes indicate the cross-shore and alongshore directions, respectively. Positive cross-shore, alongshore and elevations were set to offshore, into the flume wall and upward respectively (a right-handed coordinate system).

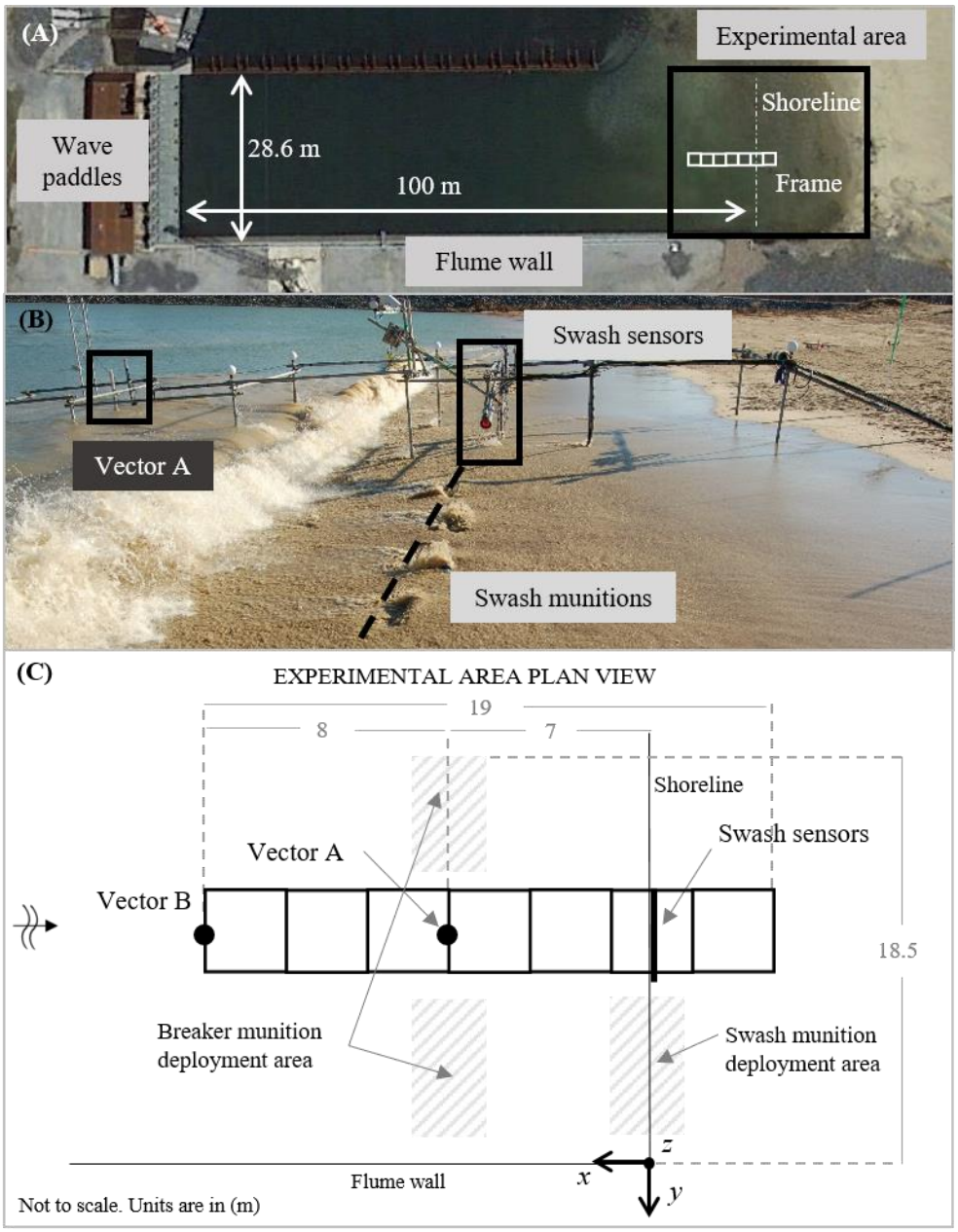

Figure 5. (A) Littoral Warfare Environment (LWE) large-scale outdoor flume located at the Aberdeen Test Center in Aberdeen, Maryland, USA (Google Earth). Shoreline depicted in the image is the shoreline location during the experiment but does not match the available satellite imagery. (B) Picture of the experimental area. (C) Sketch representing the plan view of the experimental area.

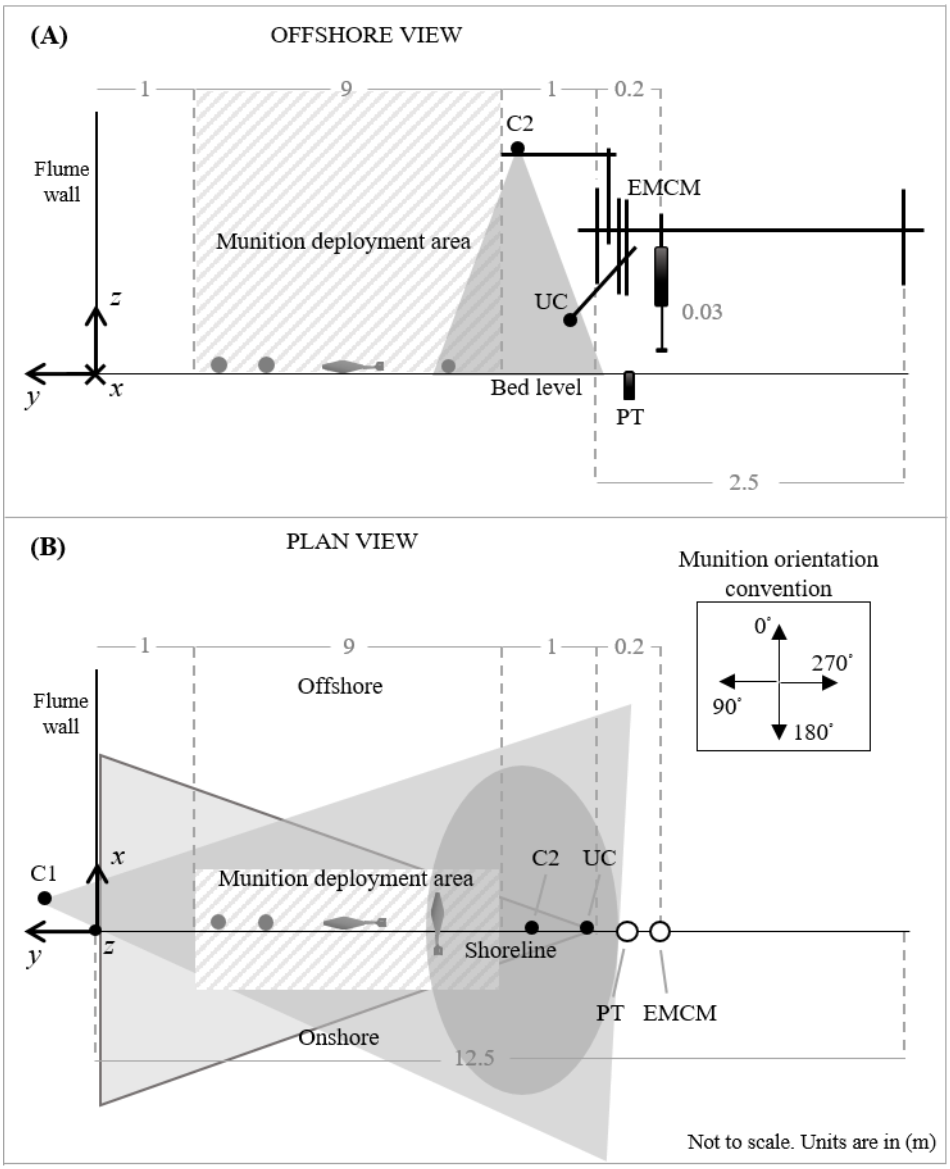

Figure 6. Swash zone sensors configuration. Offshore (A) and plan (B) views of munition deployment area, hydrodynamic sensors and cameras. The munition orientation convention is for a munition in the xy plane (munition nose is used as the pointing direction).

The munition sensors, being housed inside the munition shells, are self-contained. For this reason, munition sensors were initialized to record at the beginning of each day to avoid opening/closing operations of munition shells between runs. In situ sensors and the cameras were cabled and connected to a series of laptop computers located in a command trailer landward of the maximum runup line. All sensors involved in the experiment were synchronized via a dedicated time server using a Garmin GPS receiver and Tac32 and Dimenion4 software. In situ sensors sampled at 16 Hz. Cameras C1, C2 and UC recorded at 40, 83.33 and 30 Hz respectively.

3.2.1a Experimental procedure - Waves were run in bursts of 2.5, 5, or 10 minutes. The number of conducted runs totaled 33 for experiment LWE1 and 25 for experiment LWE2 (Table 4 and Table 5 respectively). The LWE facility has a limited number of wave spectra that can be used as

forcing conditions in the wave flume. Thus, the forcing conditions of each run were defined using Monochromatic (M), Jonswap (J), or Pierson-Moskowitz (PM) spectra, the significant wave height ranging from 0.2 to 1.1 m and the peak wave period ranging from 3 to 9 s. Nearly all possible combinations were tested during the two studies with choices made in an effort to minimize large morphological changes. Smaller morphological changes simplify sensor adjustment between runs and allow for more data collection as some sensors have a limited vertical measurement range. Breaker zone munitions were deployed at the beginning of each experiment in 0.8 - 1 m water depth. Breaker zone munitions were rarely reset between runs unless battery replacement was required due to time constraints and difficulty locating and surveying munitions in water depths potentially exceeding 1 m. Swash zone munitions were deployed along the shoreline at the beginning of each run (Figure 5B, hatched area) spanning roughly 9 m between the instrument frame and flume wall. This wide area allowed the deployment of multiple munitions at the same time. Swash zone munitions were re-deployed at the beginning of each run. The experimental procedure adopted during each run consisted of several steps. First, the swash zone munitions used for a particular run were deployed along the shoreline before the run started (Figures 5 and 6). Position, orientation and burial status were recorded for each munition. RTK GPS surveys of munition position involved either the survey of both the nose and tail of the munition and/or the munition center. The frame sensors and the cameras were initialized to start recording following surveying. Waves were forced with variable duration (Tables 4 and 5). At the end of the run, any live recording instrumentation was stopped. Post-run surveys of the orientation, burial, and position of the munitions were conducted for the swash and the breaker zone munitions. Orientation measurements were taken with a compass relative to True North (later rotated into the local coordinate system) and burial status was estimated using a ruler and undisturbed bed level. A manual estimate of 0, 25, 50, 75 or 100% buried was made when the munition was submerged and not visible under opaque water.

Table 4. Run conditions and hydrodynamics for LWE1 (tanβ = 1:16).

Run ID	Spectrum	H_s (m)	T_p (s)	Run duration (min)	Swash					Breaker	
					T_s (s)	h (m)	u_u (m/s)	u_b (m/s)	R (m)	H (m)	U (m/s)
1	J	0.52	3.28	5.0	-	-	-	-	-	0.87	1.01
2	J	0.64	3.64	5.0	5.83	0.16	0.82	0.57	-2.92	0.89	1.03
3	J	0.91	4.80	5.0	5.86	0.20	0.86	0.70	-4.04	1.00	1.14
4	J	0.91	4.80	5.0	5.54	0.19	0.78	0.82	-4.24	1.05	1.31
5	J	0.52	3.28	5.0	-	-	-	-	-	0.86	1.01
6	J	0.52	3.28	5.0	-	-	-	-	-	0.91	0.94
7	J	0.52	3.28	5.0	-	-	-	-	-	0.77	0.32
8	J	0.52	3.28	5.0	-	-	-	-	-	0.86	0.91
9	PM	0.77	4.42	5.0	5.84	0.12	0.90	0.79	-3.71	0.92	1.07
10	J	0.91	4.80	5.0	6.63	0.16	0.85	0.94	-4.12	1.01	1.24
11	J	0.91	4.80	2.5	5.79	0.11	0.88	0.69	-3.68	0.91	1.06
12	J	0.91	4.80	2.5	5.80	0.12	0.90	0.70	-3.54	0.90	1.06
13	J	0.91	4.80	2.5	5.60	0.11	0.92	0.75	-3.29	0.92	1.07
14	PM	1.10	5.25	2.5	6.47	0.23	0.99	0.97		1.02	1.19
15	PM	1.10	5.25	2.5	5.71	0.24	1.13	0.97		1.03	1.20

16	PM	1.10	5.25	2.5	5.53	0.26	1.08	1.02	-3.82	1.03	1.27
17	PM	1.10	5.25	2.5	5.71	0.25	0.98	0.98	-4.17	1.05	1.25
18	PM	1.10	5.25	2.5	5.67	0.25	1.13	0.91	-4.54	1.03	1.18
19	J	0.52	3.28	2.5	-	-	-	-	-	0.83	0.81
20	PM	0.77	4.42	2.5	5.36	0.13	0.95	0.80	-3.39	0.88	1.02
21	PM	0.77	4.42	2.5	5.26	0.14	0.83	0.82	-	0.89	0.93
22	J	0.91	4.80	2.5	5.85	0.15	0.83	0.85	-3.85	0.89	0.94
23	J	0.91	4.80	2.5	5.98	0.17	0.90	0.84	-	0.90	0.95
24	PM	1.10	5.25	2.5	5.69	0.26	0.95	1.02	-	1.02	1.28
25	PM	1.10	5.25	2.5	5.72	0.26	0.87	0.92	-	1.05	1.21
26	M	0.30	-	10.0	6.19	0.16	0.63	0.93	-3.07	0.92	0.99
27	M	0.30	-	5.0	6.37	0.17	1.00	1.29	-4.27	0.90	1.00
28	J	0.52	3.28	2.5	-	-	-	-	-	0.96	0.75
29	J	0.52	3.28	2.5	-	-	-	-	-	0.98	0.75
30	J	0.91	4.80	2.5	6.04	0.16	0.81	0.92	-3.77	1.03	0.97
31	J	1.10	5.25	2.5	5.72	0.25	1.09	1.13	-4.25	1.17	1.07
32	J	0.52	3.28	2.5	5.69	0.24	1.20	1.04	-4.44	1.15	1.03
33	J	0.52	3.28	2.5	3.24	0.27	0.37	0.56	-4.64	1.11	1.08

Table 5. Run conditions and hydrodynamics for LWE2 (tanβ = 1:10).

Run ID	Spectrum	H_s (m)	T_p (s)	Run duration (min)	Swash					Breaker	
					T_s (s)	h (m)	u_u (m/s)	u_b (m/s)	R (m)	H (m)	U (m/s)
34	J	0.91	4.80	2.5	5.78	0.16	1.30	1.08	-4.37	0.95	1.02
35	J	0.64	3.64	2.5	4.13	0.16	0.80	0.92	-3.20	0.90	0.88
36	J	0.52	3.28	10.0	-	-	-	-	-	0.72	0.18
37	M	0.30	9.00	5.0	9.01	0.20	1.71	1.72	-4.66	0.92	1.08
38	J	0.33	2.61	2.5	-	-	-	-	-	0.76	0.44
39	J	0.64	3.64	2.5	4.16	0.15	0.96	1.04	-2.94	0.89	1.02
40	J	0.91	4.80	2.5	4.41	0.20	1.30	1.06	-2.46	0.91	1.04
41	M	0.30	9.00	5.0	8.94	0.24	1.66	1.64	-2.57	0.95	1.06
42	M	0.30	9.00	5.0	8.96	0.20	1.64	1.09	-4.63	0.93	0.99
43	J	0.91	4.80	2.5	4.20	0.20	0.96	1.12	-3.18	0.95	1.00
44	M	0.30	9.00	5.0	8.92	0.23	1.68	1.26	-4.41	0.93	0.90
45	PM	1.10	5.25	2.5	5.17	0.33	1.07	1.22	-3.41	1.07	0.97
46	M	0.30	9.00	5.0	7.72	0.24	1.77	1.32	-4.75	1.00	0.94
47	M	0.30	9.00	5.0	7.61	0.26	1.12	1.32	-	0.99	0.93
48	PM	0.78	4.42	2.5	4.76	0.23	1.06	0.88	-	1.01	0.93
49	J	0.91	4.80	2.5	4.40	0.20	0.89	0.85	-	1.01	0.96
50	M	0.30	9.00	5.0	7.23	0.24	1.22	1.07	-4.72	0.98	0.90
51	M	0.30	9.00	5.0	7.35	0.29	1.55	1.28	-2.41	0.93	0.95
52	M	0.20	9.00	5.0	7.10	0.22	1.22	1.08	-2.30	0.86	0.56
53	J	0.52	3.28	2.5	-	-	-	-	-	0.91	0.70

54	J	0.91	4.80	2.5	4.46	0.24	0.74	0.90	-2.51	0.97	0.91
55	M	0.60	7.00	2.5	7.03	0.35	1.65	1.18	-3.86	1.10	0.79
56	M	0.30	9.00	5.0	7.45	0.34	1.43	1.20	-3.66	0.99	0.90
57	M	0.50	9.00	2.5	7.85	0.40	1.23	1.20	-5.20	1.00	1.12
58	M	0.30	9.00	2.5	7.52	0.31	1.45	1.56	-4.89	0.99	0.97

3.2.1b Example hydrodynamics and morphology – Time series of water depth *h*, cross-shore velocity *u* and video imagery (C1 and C2) were measured continuously during each run. Data treatment was performed prior to analysis to discard signal noise and/or times when sensors were not submerged. PT data were first adjusted for atmospheric pressure (measured by an additional subaerial PT deployed near the field trailer) and converted from volts into meters based on laboratory calibrations constructed by lowering into water the sensor to known depths. The instantaneous position of the PT and EMCM, relative to local bed level, during a run was estimated based on the position surveyed before and after each run and assuming the bed level changed linearly in time. EMCM data were removed whenever the sensor was above *h* (i.e. exposed in air). Additional quality-control for velocity data included discarding spikes based on an absolute velocity threshold (depending on the run conditions 1.6 - 2.9 m/s) and acceleration threshold (9.81 m/s^2). Examples of quality-controlled time series of *h* and *u* are shown in Figure 7 for monochromatic (A, C, E) and irregular (B, D, F) waves.

Images collected from C1 and C2 were georeferenced for quantitative analysis. Lens calibration and the survey of ground control points were used to resolve the geometry of each camera (Holland et al., 1997); where the geometry enables transferring from the two-dimensional image reference system to the three-dimensional LWE reference system. The rectification was performed projecting the original image to the beach surface (assuming alongshore uniformity) with an *xy* grid with 0.05 m spacing in both directions. A time stack (Figure 7E,F) was formed by sampling the image intensity along a particular cross-shore transect. The runup curve (Aagaard and Holm, 1989) was then detected from the time stack (black curves in Figure 7E,F) using image thresholding and manual correction. Maximum runup occasionally occurred outside of the field of view. Spline extrapolation was used to identify maximum runup in these instances.

The RTK GPS antenna was attached to a cart and pushed on a cross-shore transect for beach profiling out to wading depth. Additional offshore data were obtained from a boat using a second GPS system coupled with a sonar. The coupled system allowed the profile to be sampled almost to the wave paddles rather than solely where a researcher could wade. The profile was re-sampled every few wave runs during LWE1 and after every wave run during LWE2 to quantify the bathymetric change (Figure 8). The beach profiles changed throughout the studies, forming an offshore sandbar and changing steepness from the initial 1:16 slope for LWE1 and 1:10 slope for LWE2. However, wave conditions during LWE2 were alternated in an effort to minimize drastic changes in beach shape.

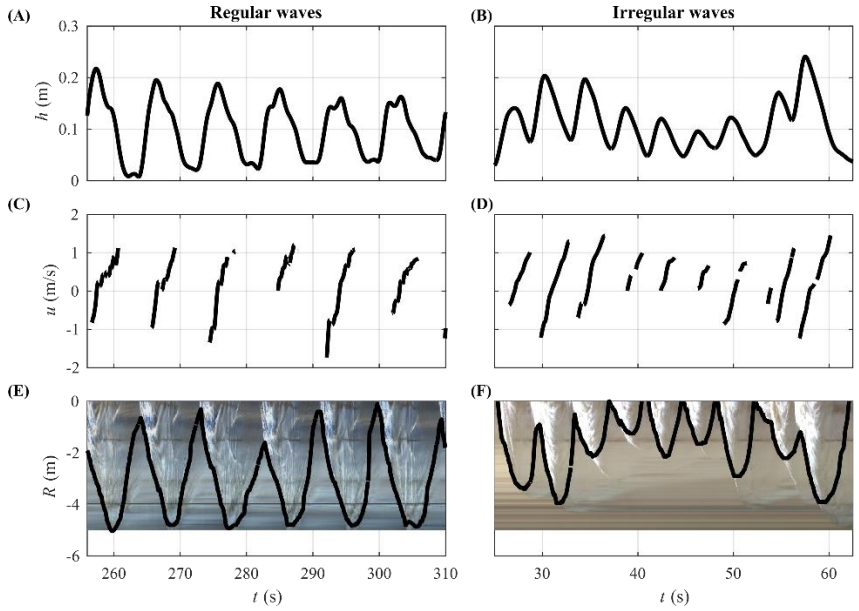

Figure 7. Swash zone observations examples for regular (run 42; left) and irregular (run 39; right) waves. A and B) water depths measured by the PT. C and D) Cross-shore flow velocity measured by the EMCM. E and F) Image time stack with horizontal run-up curve, R, highlighted (solid black line).

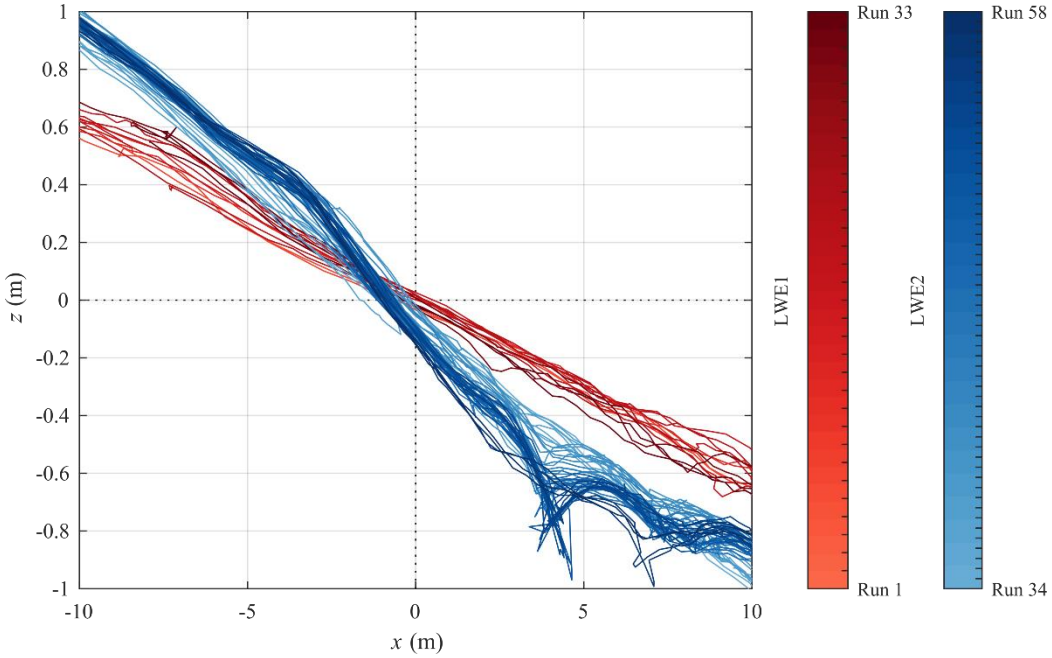

Figure 8. Foreshore profiles in the LWE reference system for LWE1 (red lines) and LWE2 (blue lines). Color gradient represents the time evolution; Run 1 (light red) to Run 33 (dark red) for LWE1 and Run 34 (light blue) to Run 58 (dark blue) for LWE2. Initial foreshore slopes are 1:16 (LWE1) and 1:10 (LWE2). The intersection between dotted black lines depict the horizontal and vertical location of the initial shoreline. Swash munitions were deployed at x = 0 m. Breaker zone munitions were placed initially at approximately x = 7 m.

3.2.2 Wallops Island, Virginia

The field study was conducted from August 15th through October 24th 2018 at a beach site within the NASA Wallops Flight Facility located in Wallops Island (Virginia, USA; 37.8431° N, 75.4779° W) (Figure 9A,B). The beach is composed of sediment with a median grain diameter of 0.35 mm. The tidal range varied between 1.0 and 1.4 m (National Oceanic and Atmospheric Administration; NOAA; 8630440 Wallops Island station). Offshore forcing conditions (Figure 9C-E) were obtained from NOAA National Data Buoy Center (station 44089 - Wallops Island). The lowest significant wave height, H_s, was recorded in August with values below 1 m. In September, H_s was generally greater than 1 m. Two major events occurred during the first half of the month, a tropical storm (September 8th – 9th) followed by hurricane Florence (September 11th – 14th). In October, H_s was consistently greater than 1 m for the first part of the month and then varied between 0.5 and 2 m except for a peak of 3.3 m on October 12. The dominant peak period, T_p, was between 5 and 15 s. The wave direction was mostly oriented around the shore-normal direction of 133° (black solid line in Figure 9E; where 133° is the angle between True North and positive *x*.

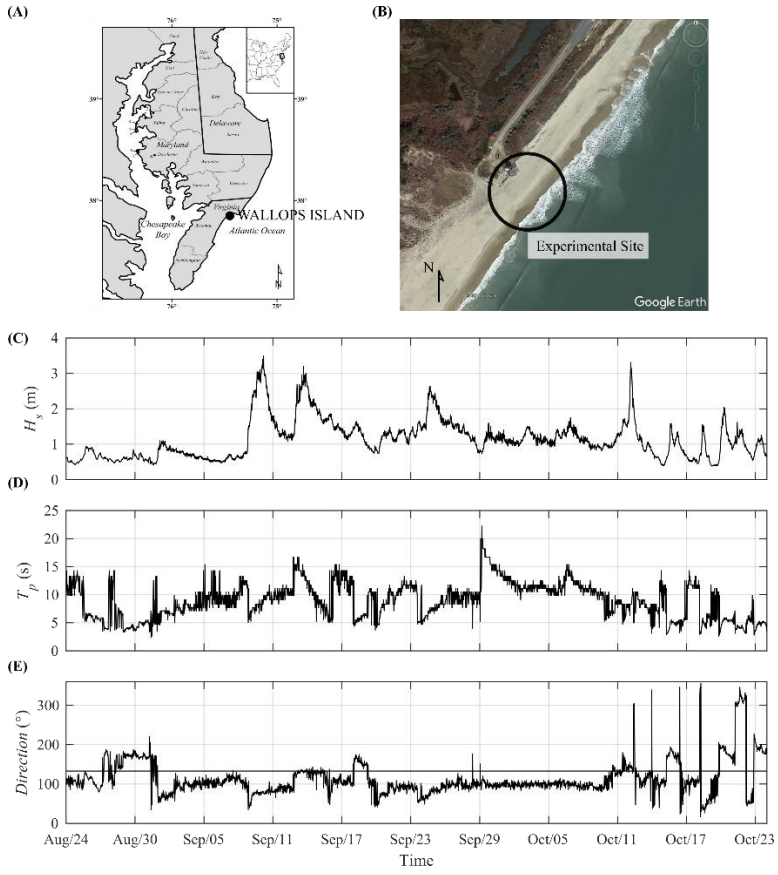

Figure 9. Map representing Wallops Island location (A) and the experimental site (B). Significant wave height (C), peak wave period (D) and wave direction (E) during the study time. Direction units are degrees from true North, increasing clockwise, with North as 0 degrees and East as 90 degrees. Solid straight line in panel E indicates the shore normal oriented direction which is 133°. Data are provided by the NOAA National Data Buoy Center; station 44089 - Wallops Island (VA).

The layout of the deployed infrastructure and instrumentation is shown in Figure 10. A confining fence was installed with the hope of preventing munitions loss outside the study area (grey dots in Figure 10A). Individual 2.4 m sections of chain-link fence were made using galvanized pipes (0.9 or 1.2 m high) as the vertical end members. Fence sections were jetted into the beach during low tide to a depth of 0.75 m. Adjacent fence sections were attached to each other using hose clamps. The overall fence structure consisted of three legs, one nearly shore-parallel (60 m) and two nearly shore normal (60 m each). The shore normal legs extended from roughly the low tide during spring conditions to the back beach. The fence area identified the majority of the study region and the region where munitions were initially deployed.

Elevation, sensor location, and munition position data were collected using RTK GPS system. Data were collected in Universal Transverse Mercator (UTM) zone 18 with vertical position referenced to North American Vertical Datum 88 (NAVD88). A local reference system, *xyz*, was subsequently identified such that *x* and *y* directions are cross-shore and alongshore respectively. The horizontal origin was set at the most landward and left pipe of the frame (see Figure 10A). Positive *x* is oriented offshore and positive *y* is oriented north such that the *xyz* reference system is right-handed. The local vertical coordinate, *z*, is positive upward and retains the value relative to NAVD88. The Mean Lower-Low Water (MLLW) is 0.32 m below NAVD88 at station 8630249, Chincoteague, USCG VA (NOAA Tides and currents).

A frame consisting scaffolding pipes was deployed inside the experimental area, roughly in the middle, as a support structure for instrumentation (grey circles in Figure 10A and photo in Figure 10B). The frame extended for a length of roughly 25 m in the cross-shore direction (~ 0 - 25 m in *x*; Figure 10A). Nine instrument stations (St. 1-9) were deployed on the frame with cross-shore spacing of about 2.7 m. Each station contains at least two sensors: an RBR pressure sensor (RBR) for water depth; and a sensor to detect flow velocity, either an electromagnetic current meter from JFE Advantech Co. (JFE) or an Acoustic Doppler Profiling Velocimeter from Nortek (Vectrino). A schematic of a station configuration is shown in Figure 10C as an example. The RBR and JFE or Vectrino always maintained the same distance relative to each other. The RBR was deployed initially at the local bed level. The JFE and Vectrino were deployed initially at 0.1 and 0.06 m above the bed respectively. Stations 5-7 were also equipped with two Conductivity Concentration Profilers (CCP) for sheet flow sediment concentrations measurements. An underwater camera, UC, located at Station 2 was oriented to detect imagery of munitions on the side of the frame and used for force balance analysis. An additional camera, deployed on top of a 2 m tower, was set to occasionally measure runup. Two additional stations, 10 and 11, with a RBR and a Nortek Vector (Figure 10A and photo in Figure 10D) were installed on standalone structures one onshore and the other one offshore with respect to the fence. The Vector is equipped with a canister where a pressure sensor is located and a probe for flow velocity measurements. The RBR and Vector canister were deployed at the bed while the Vector probes were located initially 0.25 m from the bed.

All the sensors except Vectrinos, CCPs and cameras were self-contained (batteries and data logging). The Vectrinos, CCPs and cameras were cabled and connected to computers located inside a trailer landward of the dune. All computers were synchronized using a local network, Garmin GPS antenna and Dimension4 and Tac32 software. Self-contained sensors were initialized via computers connected to the network prior to deployment. Sample rates were 2 Hz

and 16 Hz for RBRs, 10 Hz for JFEs, 100 Hz for Vectrinos, 8 Hz for CCPs, 30 Hz for cameras and 32 Hz for Vectors. Cabled sensors continuously recorded throughout the duration of the experiment. Recordings from self-contained sensors were interrupted each time battery switching and/or data downloading was needed but otherwise recorded for the duration of the experiment. Vectors were set to record in bursts of 5 minutes every 30 minutes to preserve battery life. Some sensors malfunctioned during the experiment.

3.2.2a Daily sensor procedure - The daily site routine involved sensor elevation adjustments relative to the local bed level and beach profile surveys to roughly 0.5 m depth at low tide using the RTK GPS system. Two cross-shore transects were chosen, one on each side of the frame and approximately 5 m away from it. The selected transects extended from -20 to 30 m in *x*. The field site was accessible during weekdays and only between the local hours of 0800 and 1800. Thus, surveys and instrumentation adjustments occurred every weekday, during the most convenient low tide.

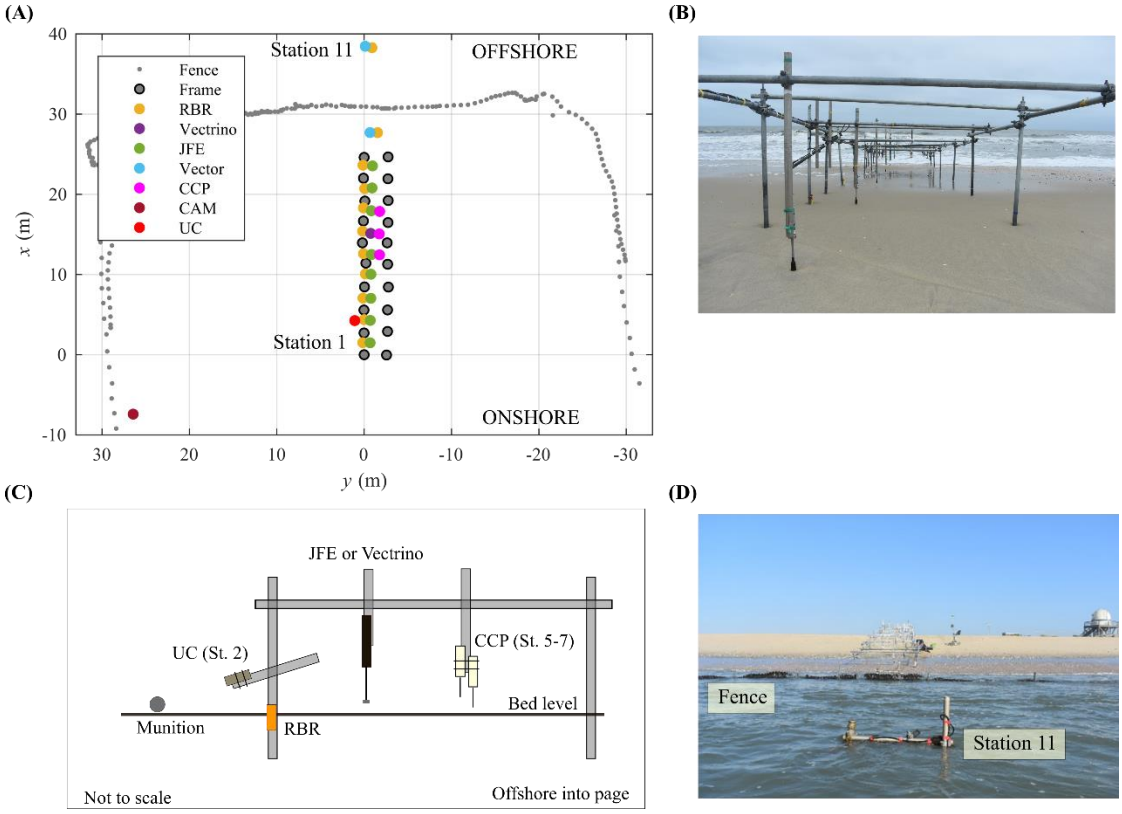

Figure 10. Field setup. (A) 2D map of deployed infrastructure and instrumentation in the local reference system. (B) Photo of the frame and the stations taken from the onshore looking seaward. (C) Schematic of a generic instrumentation station (St. 1-9 only) with pipe and sensors configuration. (D) Photo of the frame and the stations taken from the offshore side looking landward.

3.2.2b Munitions deployment - Munitions (Figure 11A) were deployed in two approaches: long-term deployment and rapid resetting for force analysis. A total of 50 munitions were deployed for the long-term approach on August 24th on both sides of the instrument frame and within the experimental area confined by the fence (Figure 11B and Table 6). The initial munition

configuration (Figure 11B) followed the criteria of deploying the same type of munition at the same cross-shore location with different initial burial states to observe differences in initiation of motion caused by different degrees of burial. Munitions were deployed with at least 2 m clearance relative to other munitions reducing the chance of collision in case of mobility. Each munition had a string attached to it with a float on the other end to facilitate munition identification in water or in case of burial. Different float sizes were used proportionally with the weight of the munitions to avoid interfering with motion.

Only 10 munitions out of the 50 long-term deployed contained sensors (Table 6), due to the large amount of munitions and the relatively smaller number of available sensors. The IMU was housed in eight munitions: two RKT, three 155-mm, one BLU-61, one 81-mm and one 81-mm-nf; where nf implies no fins. The PT was deployed in four RKT and two 155-mm. Figure 11B provides an overview of where instrumented munitions were deployed and the sensor distribution among the munitions. Instrumented surrogates were deployed with the IMU and PT already in recording mode. The IMU and PT were both initialized using a laptop computer synchronized to the other recording devices in the field trailer. Sampling rates were 16 Hz for IMU and 4 Hz for PT. The daily munition survey routine involved munition locating aided by metal detectors, surveying of found munition position via RTK GPS, munition orientation (in case of cylindrical-shape munitions) and burial depth relative to local bed level.

For force analysis, each of the munitions listed in Table 6 (force balance analysis munitions section) was deployed alone on the beach face in front of the UC camera when swash conditions occurred at Station 2. The munitions selected all contain an IMU. Before performing force testing, the IMU was initialized and synchronized with the rest of the instrumentation. Hydrodynamic data were continuously recording. The sequence of events for force analysis deployment was: 1) Deploy the munition proud in front of camera UC; 2) Survey the initial position via RTK GPS; 3) Survey the final position and burial depth following a swash event. Each munition was tested repeatedly but on different days since swash conditions generally lasted for about one hour at Station 2. Each swash event per each munition tested is referred to as a case (Table 6). Sampling rates for munition sensors were set equal to long term munition sensors.

3.2.2c Hydrodynamics and morphology – The hydrodynamics experienced during the field study showed variations over a period of about two months. As an example, water depth and cross-shore velocities from three different days are shown (Figure 12): August 24th when munitions were initially deployed; September 9th when the most energetic storm observed during the experiment occurred; and October 2nd when the first efforts for force analysis were conducted. The data excerpts provide an indication of the offshore conditions and a corresponding swash event (the time windows selected correspond to one of the two high tides of the day). Subsequently, data from stations 2 and 4 are used for swash data while station 9, located farther offshore, is used for surf zone hydrodynamics. Station 4 is chosen for August 24th due to the steepness of the beach profile; at the beginning of the experiment, station 3 was barely reached by swash motions and stations 1 and 2 stayed dry for the entire tidal cycle.

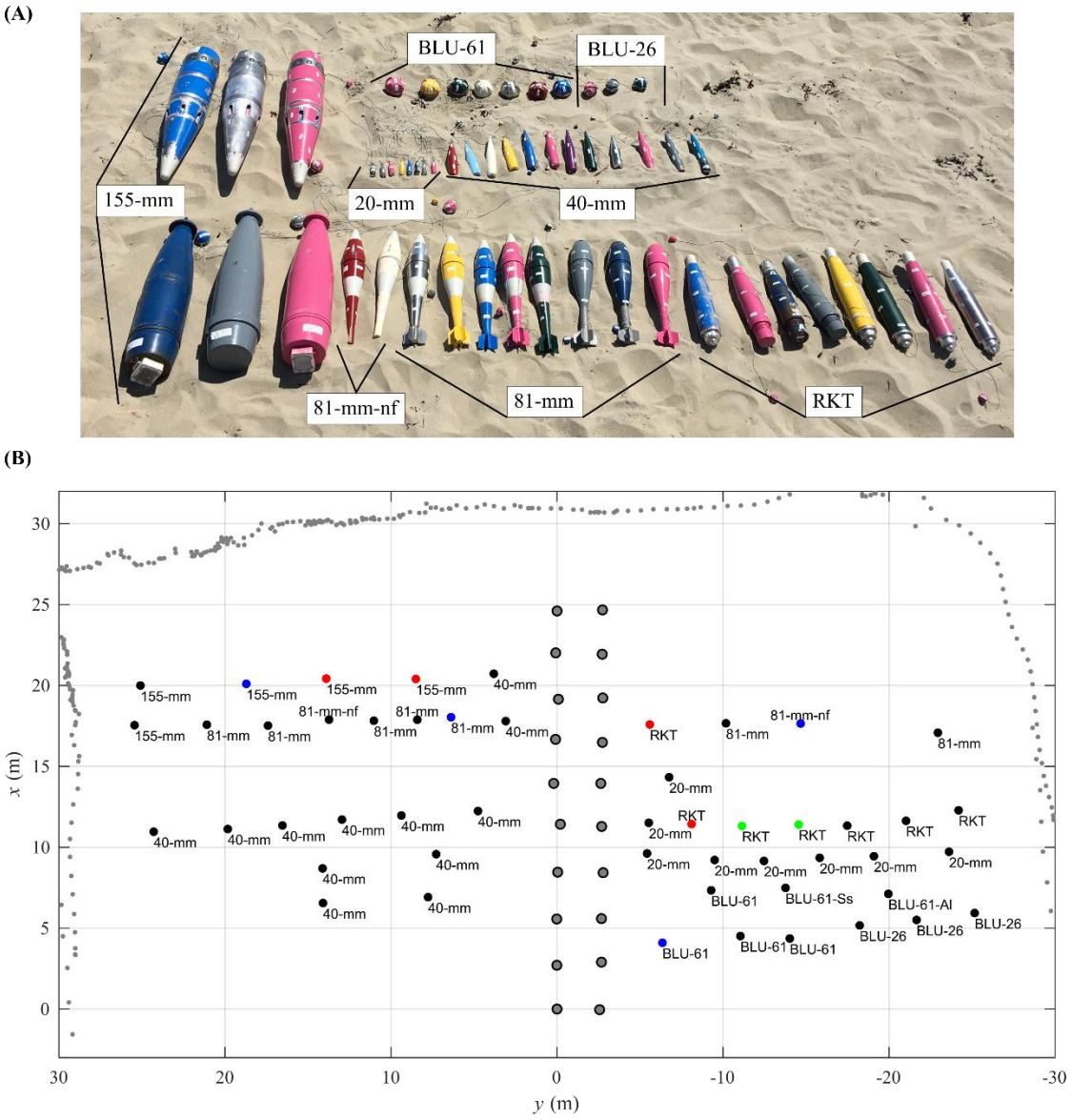

Figure 11. (A) Munitions deployed during the field study (both long term and force analysis munitions). (B) Long term munition initial deployment. Color-coding is related to munition instrumentation, green = PT; Blue = IMU; Red = IMU and PT; and black = not instrumented.

Table 6. Munitions deployed for long term observations and for force balance analysis and relative physical parameters of diameter, length and density.

Long term munitions						Force analysis munitions			
Munition ID	D_m (m)	L (m)	ρ_m (kg/m3)	No-sensors	Sensors	Munition ID	Date	Sensors	Cases Tested
20-mm	0.020	0.075	7990	8	-	RKT	Oct 2	IMU, PT	7
40-mm	0.040	0.200	5720	12	-				
BLU-26	0.065	0.065	2939	3	-	BLU-61	Oct 3	IMU	7
BLU-61	0.099	0.099	4460	3	1				
BLU-61-Ss	0.099	0.099	7999	1	-	81-mm	Oct 9	IMU	13
BLU-61-Al	0.099	0.099	2700	1	-				
81-mm	0.081	0.481	4180	6	1	81-mm-nf	Oct 4	IMU	7
81-mm-nf	0.081	0.481	4180	1	1				
RKT	0.070	0.405	3320	3	4	155-mm	Oct 10	IMU, PH, PT	24
155-mm	0.155	0.754	4230	2	3				
Total	-	-	-	40	10	Total	-	-	58

Water levels are referenced to the local bed level. Flow velocities are negative (positive) if onshore (offshore) oriented. Water levels at station 9 were commonly between 1.5 - 2 m for August 24th (Figure 12A) and Oct 2nd (Figure12E) which represent calm conditions. However, *h* exceeded 3 m at station 9 on September 9th (Figure12C), which is the highest *h* observed over the experiment duration. Flow velocities were not recorded on Sep 9th due to beach accretion and sensor burial. Near-bed flow velocities during calm conditions were confined between -1.0 and 0.6 m/s (Figure 12A) and -0.9 and 1.1 m/s (Figure 12E).

The corresponding swash zone data show large cross-shore velocities with maximum values reaching 2.5 m/s for both calm days (Figure 12B and 12F). Maximum water depths are on the order of 0.2 m for both days. Depth and cross-shore velocity during the storm (0.3 m and 2.3 m/s respectively; Figure 12D) appear comparable with the calm days. However, sensor elevation above the bed is likely responsible for this counterintuitive finding. An erosion event of over 1 m vertically occurred between September 7th and the 10th. RBR and JFE sensors at station 2 on September 7th at 10 am local time were located at -0.01 m and 0.07 m respectively. On September 10th at 12 pm local time (the subsequent weekday when the site could be accessed) sensors at station 2 were located at ~ 1.2 m above the bed. The sensor locations relative to the bed suggest that the sensors were also located at a higher relative elevation on September 9th during the storm (Figure 12D). Therefore, *h* measurements are underestimated potentially by over 1 m and *u* is only captured just at the beginning of the event.

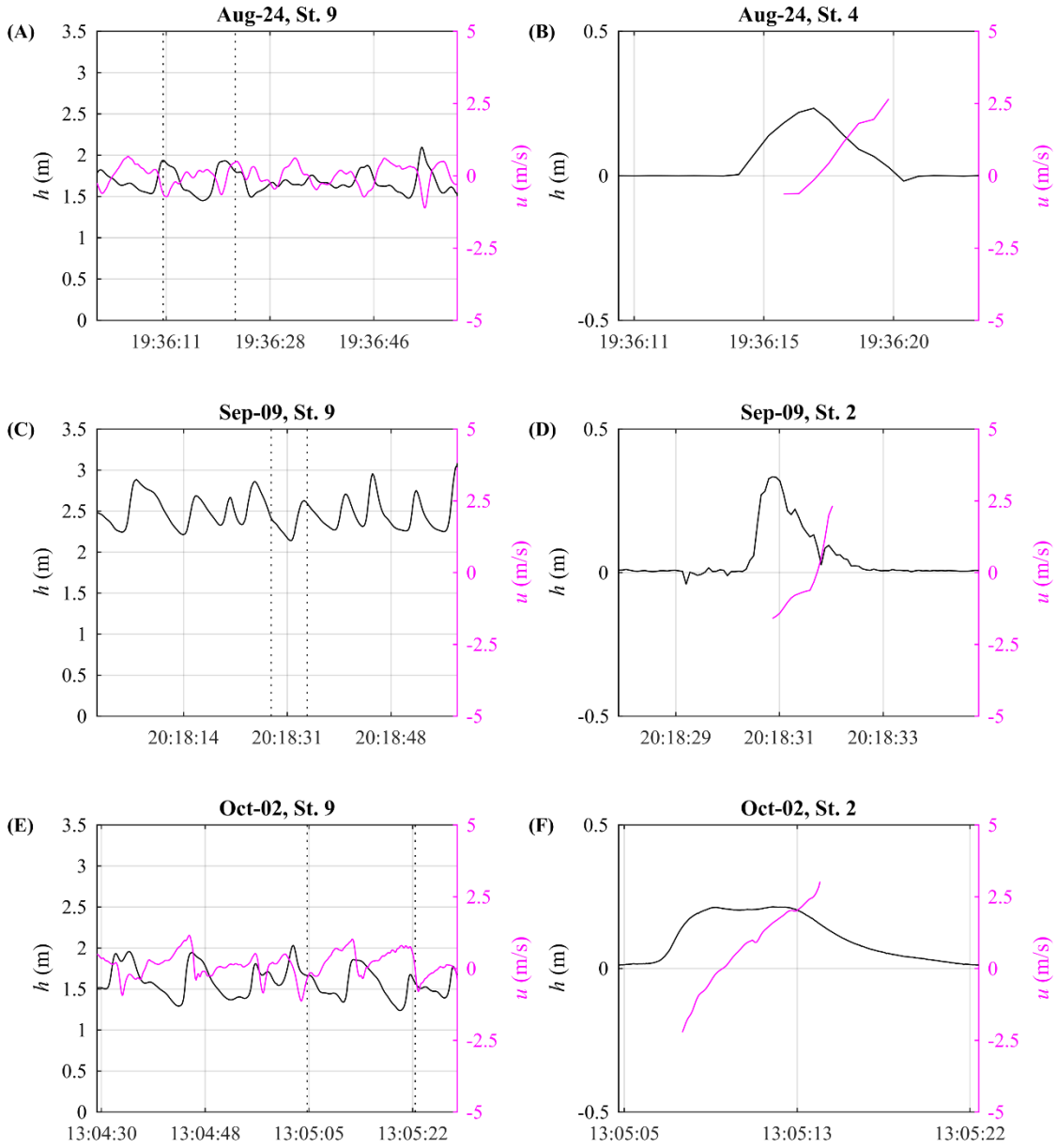

Figure 12. Typical hydrodynamics, water depth and near-bed cross-shore velocities observed during the experiment in calm conditions (A, B), storm event (C, D) and during the period the force balance analysis was carried out (E, F).

The beach profile evolved in response to the forcing conditions with daily changes (Figure 13). The profiles shown were surveyed on the left (north) side of the frame looking seaward ($y \approx 5$ m). Vertical changes were maximally 0.20 m from August 24th to September 7th. After the storm occurred (September 8th - 9th) the landward part of the profile ($x < 16.5$ m) eroded drastically causing the seaward part of the profile ($x > 16.5$) to accrete. The maximum accretion observed was almost 1.3 m and it occurred at $x = 2.6$ m. In the seaward part of the profile, the erosion observed was on the same order of magnitude and ~1.4 m at the fence ($x = 32$ m). The beach

profile flattened and changed steepness from 1:8 to 1:30 during the storm. For the rest of the study time the beach slowly recovered and readjusted to the initial profile (around Oct 20th). Beach morphology changes that occur in the swash and surf zones influence munition burial or exhumation.

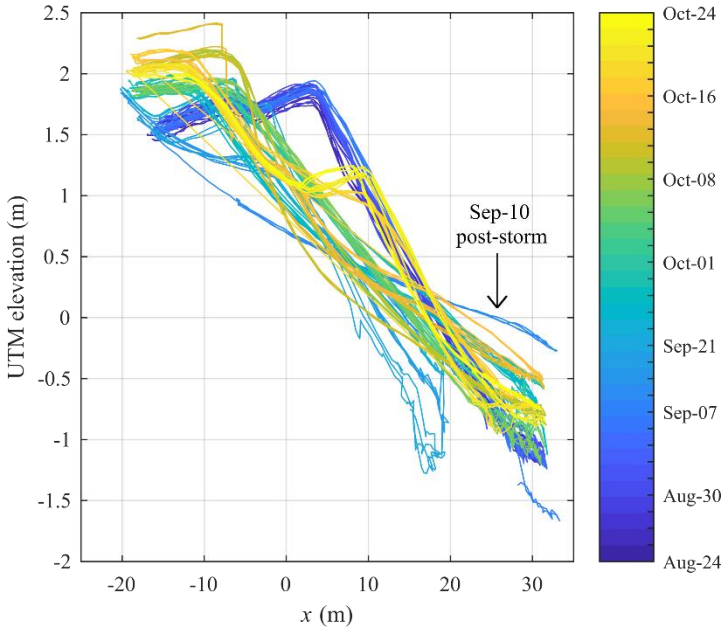

Figure 13. Beach profile evolution over the field experiment duration. The profiles were surveyed on the left (north) side of the frame looking seaward ($y \approx 5$ m).

3.3 Munition Attitude Data Extraction

3.3.1 Munition migration from imagery

Munition tracking from imagery consists of locating munition *x, y* positions in the rectified image. The tracking may be accomplished automatically via image processing algorithms if the object is easily identifiable. During the LWE studies multiple munitions were deployed at the same time and most of the motion occurred when the munition was difficult to identify automatically due to the presence of foam. The presence of fluid and foam also complicated automated algorithms during the field effort. Therefore, munition positions (nose and tail) were identified manually. Multiple manual identifications (18 iterations) of a particular fixed munition yielded horizontal variability errors of 0.05 m for *x* and 0.08 m for *y;* essentially the same size as the grid spacing used for image rectification. This error is assumed to be consistent for all manual identification. Munition position identification is not possible when the munition is fully submerged or completely covered by bubbles/foam.

3.3.2 Munition migration from the IMU

The IMU can overcome some of the imagery limitations since data are recorded continuously. A simple algorithm was developed to derive munition trajectories using IMU measurements (shown schematically in Figure 14A; see also Frank et al., 2016). Munitions of cylindrical shape were observed to move mostly due to rolling around x_m, the axis passing through the longest dimension. Thus, the initial step was to quantify the cumulative angle of rotation (φ) time series

around x_m. Second, the migration in the local reference system x, y was determined through the IMU heading measurement.

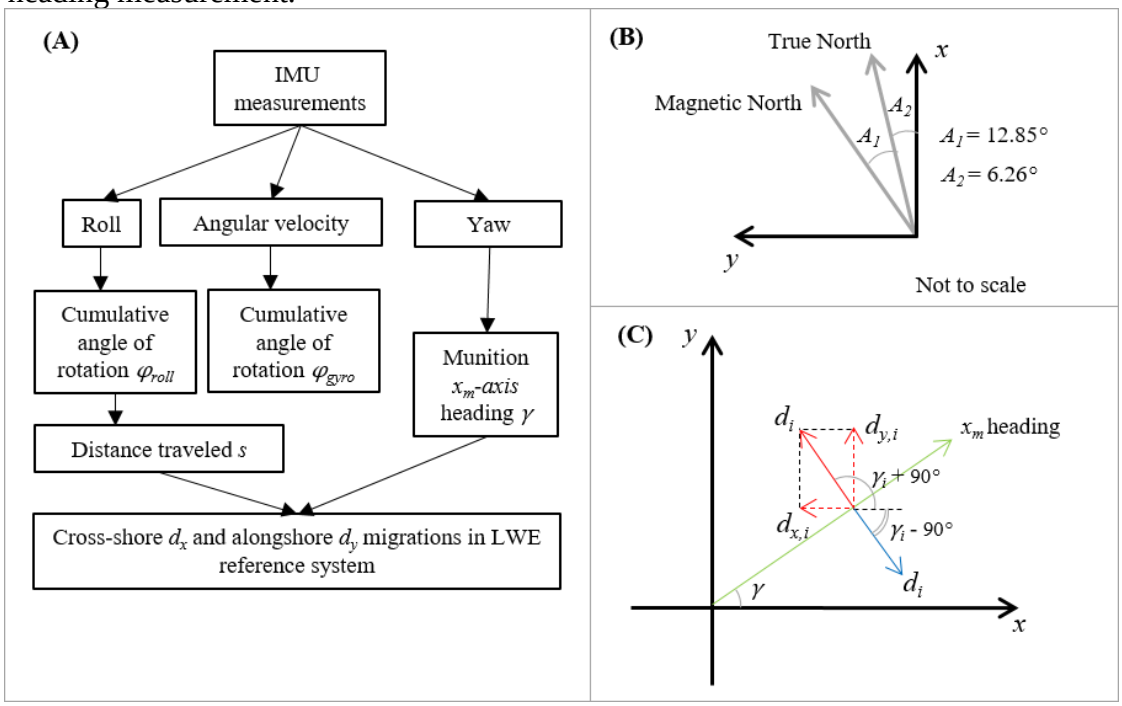

Figure 14. A) Steps involved in the IMU algorithm developed to derive the munition trajectory relative to the LWE reference system. B) LWE reference system, True North and Magnetic North directions. C) Schematic of the variables involved in the IMU algorithm.

There are two IMU measurements from which φ can be estimated: the instantaneous orientation relative to x_m (φ_{roll}); and the angular velocity around x_m (φ_{gyro}). IMU sign convention follows the right-hand rule; clockwise munition rotation around x_m yields a positive roll and positive angular velocities. Cumulative rotation angle is obtained directly from roll simply summing cumulatively the roll time series and subtracting the initial roll. The distance traveled by the rolling munition is quantified using the munition diameter as

$$s = \frac{\pi D_m \varphi_{roll}}{360^{\circ}}, \tag{16}$$

where s represents the cumulative distance traveled through rotation around x_m. The combination of s with the time series of heading of x_m is used to identify the cross-shore and alongshore trajectory components. The instantaneous yaw angle determines the angle between x_m and Magnetic North (Figure 14B). Angles A_1 and A_2 (respectively indicating the angle difference between Magnetic North and True North, and True North and x; Figure 14B) are used to alter yaw measurements and determine the munition heading time series, γ. Note that γ ranges between 0 and 360°, indicating the heading relative to the xy horizontal plane. On the contrary, φ_{roll} does not have a 360° limitation and the sign could be either positive or negative, depending on the munition migration.

The steps involved to derive munition trajectory in x, y using γ and s are repeated for each instant of time. The trajectory, d_i, from time t_{i-1} to t_i, is calculated from the distance traveled s_{i-1} to s_i as

$$d_i = s_i - s_{i-1}. \quad (17)$$

The heading of x_m in the horizontal plane at t_i is provided by γ_i (green arrow in Figure 14B). Depending on the sign of d_i, the munition rolled either clockwise (positive roll, positive d_i, blue arrow in Figure 14B) or counterclockwise (negative roll, negative d_i, red arrow in Figure 14C). With γ_i being the heading relative to the Cartesian axis, γ_i + 90° and γ_i - 90° are the corresponding angles of the red and blue arrows. The relative components of d_i in x and y, $d_{x,i}$ and $d_{y,i}$, are thus calculated as

$$d_{x,i} = d_i \cos(\gamma_i \pm 90°) \cos\beta, \quad (18)$$

$$d_{y,i} = d_i \sin(\gamma_i \pm 90°). \quad (19)$$

Equation (18) accounts for the angle β between the plane where the munition moves (beach slope) and the horizontal x coordinate. The cumulative sum of $d_{x,i}$ and $d_{y,i}$ provides the time series of the components of motion in x and y respectively. The initial munition position from RTK GPS surveys or manual measurements is added to d_x and d_y that have initial values of zero, if needed.

3.3.3 Munition burial evolution

Apparent burial time series is estimated for surrogate 155-mm munitions that contained the photocell array. Each of the 12 photocell voltage time series was normalized by the highest voltage recorded by all 12 photocells during the run. The photocell voltage, after normalization, varies between 0 (no light received) and 1 (maximum light received). Deriving the amount of burial, B (defined as burial depth below the mean local bed level; Friedrichs et al., 2016), from the photocell array data is possible if the orientation of the munition (from the IMU), is known at each instant of time. There are 24 possible initial orientations (from the photocell standpoint) considering that either one or two photocells can be oriented downward. The 24 orientations are classified as $\alpha \pm 15°/2$ where $\alpha = 0°,15°,\ldots,330°$, the angular separation distance between photocells. The roll angle at time t determines the orientation at time t. For instance, photocells PH01 and PH02 are oriented downward when $\alpha = 0° \pm 15°/2$ (Figure 15A). Another example, shows a single photocell (PH11) oriented downward when α falls in the range $75° \pm 15°/2$ (Figure 15B).

Note that temporal burial evolution is derived for cases of no motion only (cutoff of 0.05 m for cross-shore migration). Thus, the change of orientation is relatively small and confined within less than one complete rotation ($\varphi_{roll} < 360°$). For cases where the IMU malfunctioned, initial munition orientation may be determined by the photocell array signal. The photocell with the minimum normalized voltage can be identified as being oriented downward and thus has an error of ± 7.5°. Occasionally, multiple photocells had the same minimum normalized voltage at time t = 0. For such cases, the photocell/photocells located in the middle among the lowest voltage photocells is/are set as oriented downward. An algorithm was implemented to estimate the time history of local bed level, relative to the cross-section of the 155-mm. A normalized threshold of 0.5 for the swash zone and 0.2 for the breaker zone was used to indicate burial or exposure; where photocells with a normalized voltage lower than the threshold were considered buried.

Different thresholds were needed in the swash and breaker zones due to water turbidity and depth for the breaker zone munitions (light attenuation) and the shallower water depth and intermittent exposure to air for the swash zone munitions. Often, multiple photocells appear buried at a given time. The arc of buried photocells is divided in half by a vertical line that passes through the circle center (Figure 15C). The local bed level (i.e. burial depth B) is set as the same elevation of the highest buried photocells among the highest on the left (PHL in Figure 15C) and on the right (PHR in Figure 15C). Finally, B is normalized by the corresponding munition diameter D_m. B/D_m represents the dimensionless burial depth.

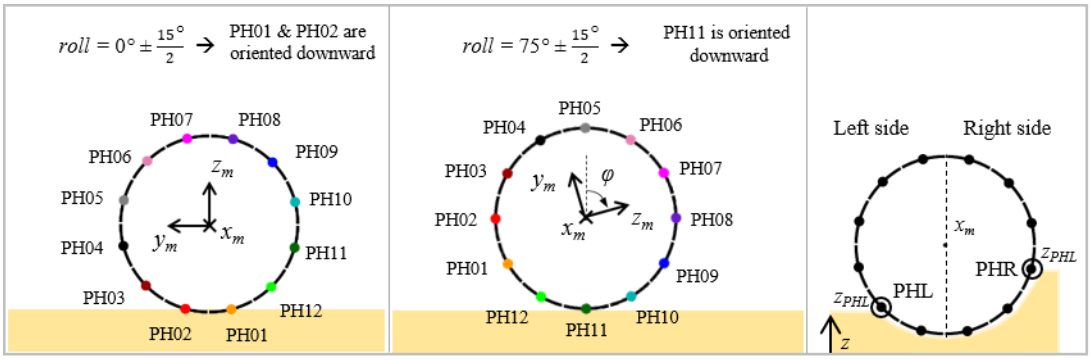

Figure 15. Cross-sections of 155-mm surrogate munition showing photocell location relative to the munition and IMU reference system $x_m y_m z_m$; A) and B) examples of cross-shore munition orientation relative to z axis of LWE reference system for roll angles of 0° and 75° respectively. C) Example of a typical configuration of burial status that highlight how the burial algorithm works if the degree of burial is different when comparing the left and right side of the munition cross-section.

4 Results and Discussion

4.1 Burial as a Function of KC, θ and Bed Morphology Changes

Relationships between burial depth observed from LWE cases of no motion (98) and θ (Figure 16A) and KC (Figure 16B) were investigated. Note that cases of different run conditions, different munition types and different foreshore slopes are presented together. Inerts and surrogates are not segregated. The color separation indicates the different experiments and thus the foreshore slope (milder slope in red tones for LWE1, steeper slope in blue tones for LWE2). The color gradient provides a representation of munition density. Sixty-four of the 98 cases occurred on the milder slope where less migration was observed. The Shields number ranged between 1.3 and 7.5; indicating the presence of sheet flow conditions (Nielsen, 1993) and/or bed fluidization. KC ranged between 11.6 and 308.1. It appears the munition density played a role for LWE1 cases since denser munitions (darker red markers) showed greater B/D_m with maximum relative burial of 2. Data were tested with equation (7) with the highest correlations for $a_1 = 0.47$ and $b_1 = 0.29$ but the squared correlation coefficient, r^2, was only 0.05. Note the solid line in Figure 16A representing equation 7 with $b_1 = 0.85$ was found for short cylinders in oscillatory flow (Cantano-Lopera et al., 2007). Equation (8) for KC was also tested. The two lines in Figure 16B were identified for cylinders ($a_2 = 0.1$; $c_2 = 0.51$) and frusta ($a_2 = 0.0077$; $c_2 = 0.78$) for equilibrium burial of fully submerged objects subjected to wave forcing (Friedrichs et al., 2016a). LWE swash zone observations fall between the two empirical relationships even though they are intermittently submerged and do not reach equilibrium burial. Coefficients $a_2 = 0.09$ and

c_2 = 0.43 were found for the observed burial depths (solid line in Figure 16B) with an r^2 of 0.39. Using the object mobility number instead of Shields number or KC yielded an r^2 of 0.32.

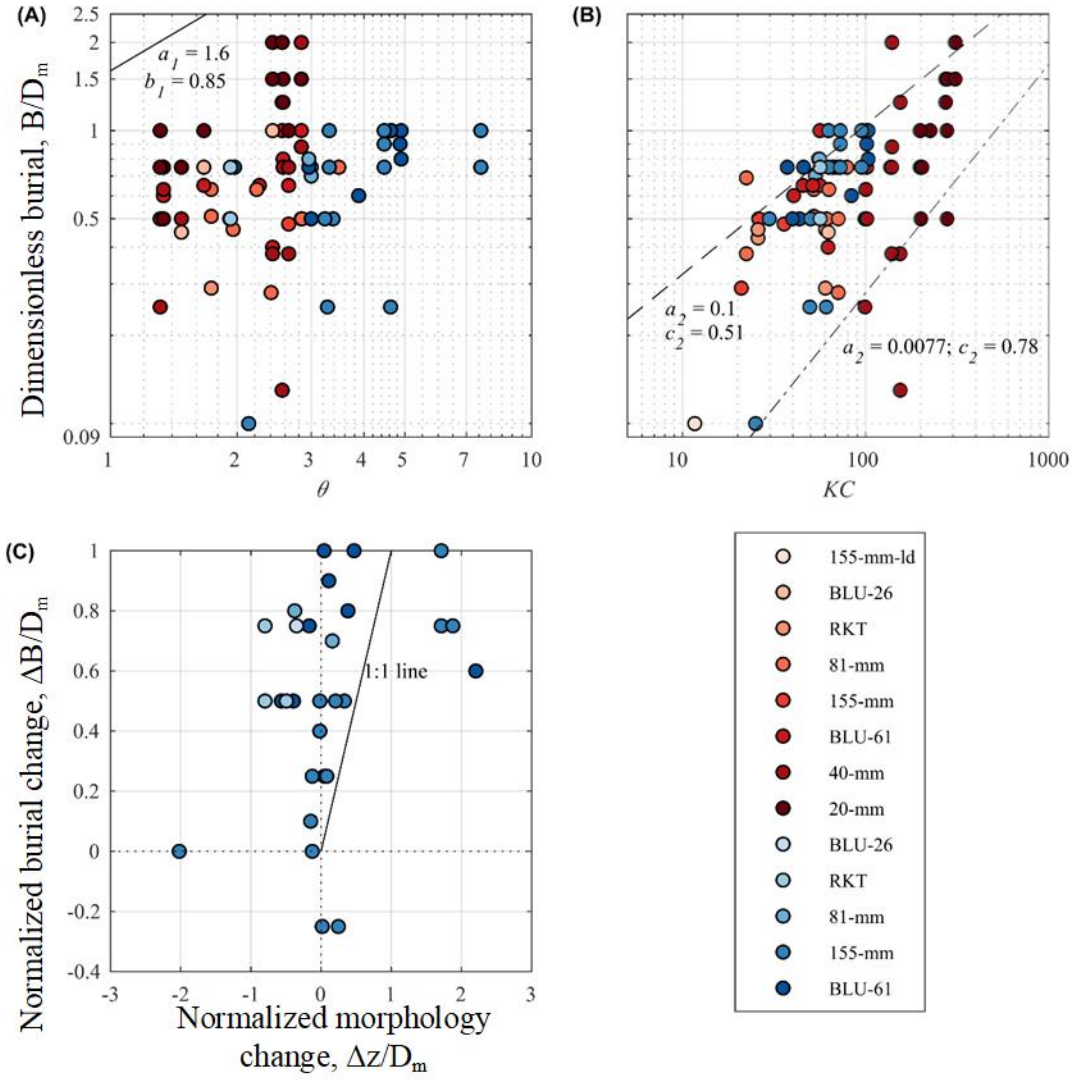

Figure 16. Post-run dimensionless burial depth observations as a function of Shields number (A) and the Keulegan-Carpenter number (B) for swash zone deployed munitions of the no motion cases. C) Dimensionless burial rate as a function of the dimensionless beach morphology change rate. Color separation is relative to the foreshore steepness (red for tanβ = 1:16, blue for tanβ = 1:10). Color gradients indicate munition density with lighter color corresponding to less dense objects. Lines (A and B) represent different relationships from the literature with corresponding coefficients a_1 and b_1 and a_2 and c_2.

A comparison between the relative burial achieved by the munition at the end of the run and the normalized beach profile changes, $\Delta z/D_m$, occurring within the run is shown to investigate the role of the morphodynamic changes in the munition burial process (Figure 16C). The data are shown for no mobility munitions tested for the LWE2 1:10 slope (beach profiles were not surveyed after every run for LWE1 – slope 1:16 experiment). The majority of the data had

relative burial greater than 0 as most of the munitions were deployed with an initial burial, B_i = 0. $\Delta z > 0$ (< 0) indicates accretion (erosion) had occurred. The first quadrant in the figure ($\Delta z > 0$ and positive burial) indicates foreshore accretion and munition burial. If the burial processes were governed solely by the beach morphology changes, the data would exist along the 1:1 line (accretion = burial depth). However, the observations are mostly located above the 1:1 line suggesting that the munition burial on the foreshore is governed additionally by local scour processes, as might be expected. Even when the foreshore eroded ($\Delta z < 0$), munitions also experience burial further indicating the importance of local scour processes.

4.2 Migration as a Function of KC, θ_m and Bed Morphology Changes

Additional analyses on cross-shore migration were conducted for the LWE motion group (Figure 17) with 100 cases for the steeper slope and 49 cases for the milder slope (Table 7). Most of the mobility (69%) was offshore-directed (positive d_x) with some onshore-directed motion for a variety of munitions bulk density. The largest offshore migration (15 – 20 m) occurred for the 155-mm-ld (ρ_m = 2115 kg/m^3; Figure 17), the lowest density munition tested, on the milder sloping beach. Interestingly, some 155-mm-ld also migrated onshore yielding the three largest onshore directed migrations observed of 2.5, 4.3 and 5.1 m (θ = 2.3- 3.5). In contrast, the similarly shaped 155-mm (ρ_m = 4230 kg/m^3) had average offshore migration distances of only 0.1 m regardless of forcing or slope conditions. There was an exception where one 155-mm migrated offshore 4.2 m under the most intense forcing conditions but another 155-mm deployed initially at the same cross-shore position migrated only 0.14 m. No 155-mm were observed to migrate onshore.

Table 7. Number of swash zone and breaker zone munitions tested for LWE1 and LWE2 experiments. Note that the "IMU" cases are a sub-group of "Cases tested" with the IMU deployed only inside certain munitions.

Region	Study	*tan β*	Cases tested			IMU		
			Total	No Motion	Motion	Total	No Motion	Motion
Swash zone	LWE1	1:16	113	64	49	23	15	8
	LWE2	1:10	134	34	100	48	16	32
Breaker zone	LWE1	1:16	792	-	-	202	181	21
	LWE2	1:10	159	64	95	60	44	16

Comparisons for migration were also made with the object mobility numbers. The maximum object mobility number observed was 1.53. However, the majority of the motion data had θ_m < 1.09 (similarly for $\theta_{m\,mod}$). There is no substantial difference between the relationships found for migration with θ_m (Fig 17A) and $\theta_{m\,mod}$ (Figure 17B) as most of the munitions were typically deployed proud initially. The extra factor included in $\theta_{m\,mod}$ that accounts for initial burial depth varies between 0 (100% initial burial or more) and 1 (0% initial burial). Under equal conditions a larger object mobility number should indicate a larger potential for the object to be mobilized. Note in Figure 17B the data points in proximity of $\theta_{m\,mod}$ between 0 and 0.2 with the mobility number reduced by the extra factor. Both plots indicate scatter but with denser munitions migrating shorter distances. Interestingly, different d_x were observed under the same mobility number (i.e. same flow velocity) for the same type of munition. These cases were observed

mostly for RKT and 81-mm with travel distances ranging from 1.6 – 7.8 m for θ_m = 0.89 and 0.07 – 4.1 m for θ_m = 0.4 respectively.

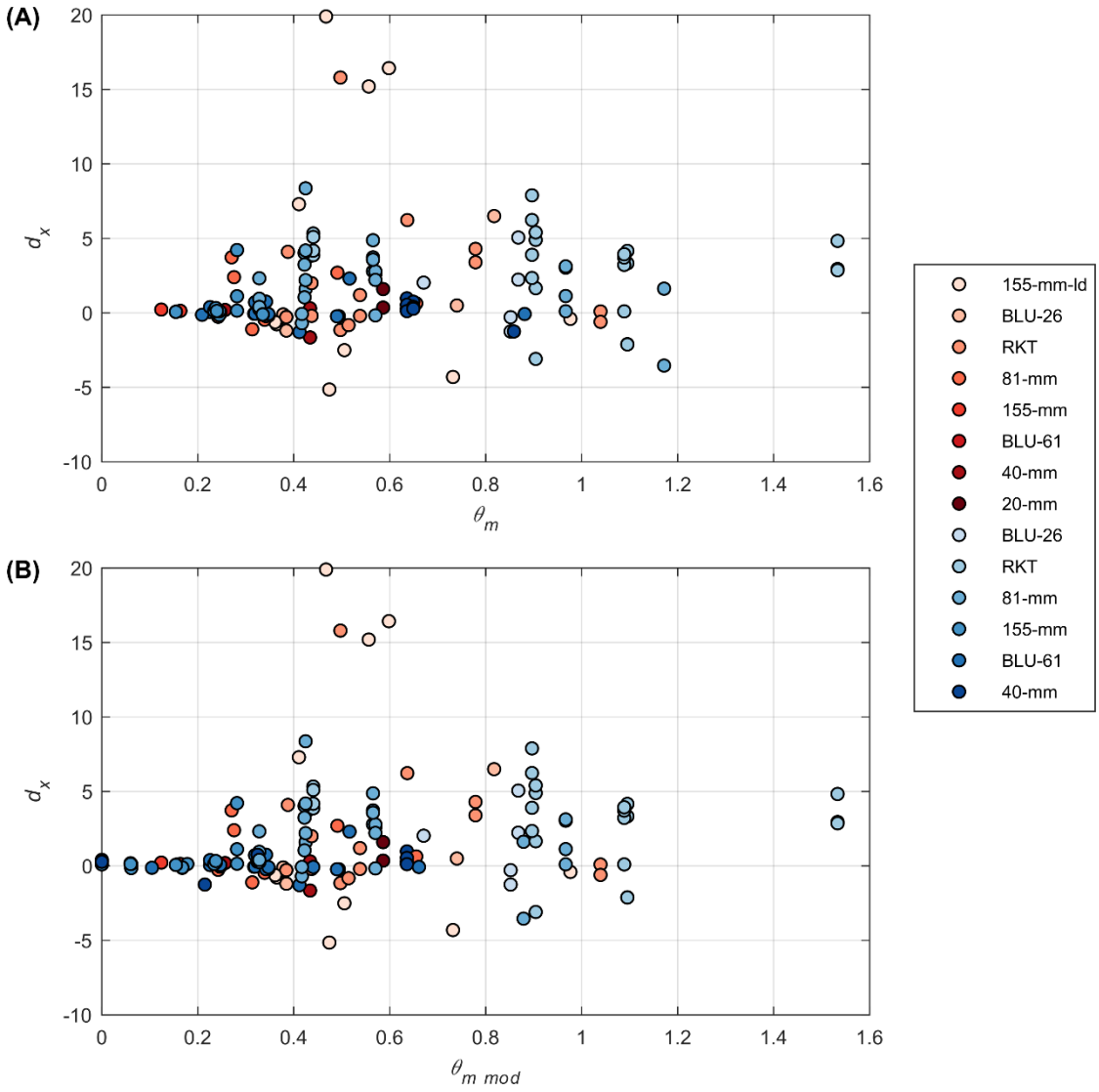

Figure 17. Cross-shore migration measured post-run as a function of the object mobility number (A) and the modified object mobility number (B) for swash zone deployed munitions of the LWE motion cases. Color separation is relative to the foreshore steepness (red for tanβ = 1:16, blue for tanβ = 1:10). Color gradients indicate munition density with lighter color corresponding to less dense munitions.

4.3 Burial and Migration Semi-Empirical Formulations

Numerous potential parameters could be associated with munitions burial; *KC* and θ already tested individually. A nonlinear least squares regression of the form

$$B/_{D_m} = a_3 \theta^{b_3} KC^{c_3}, \tag{20}$$

was tested yielding a_3 = 0.06, b_3 = 0.24 and c_3 =0.5 (Figure 18A). The r^2 value is 0.45 with a best fit slope and intercept of 0.94 and 0.046 respectively. A similar coefficient c_3 was found previously for cylinders (c_3 = 0.51; Friedrichs et al., 2016a) and fixed pipelines (c_3 = 0.50; Sumer and Fredsøe, 2001).

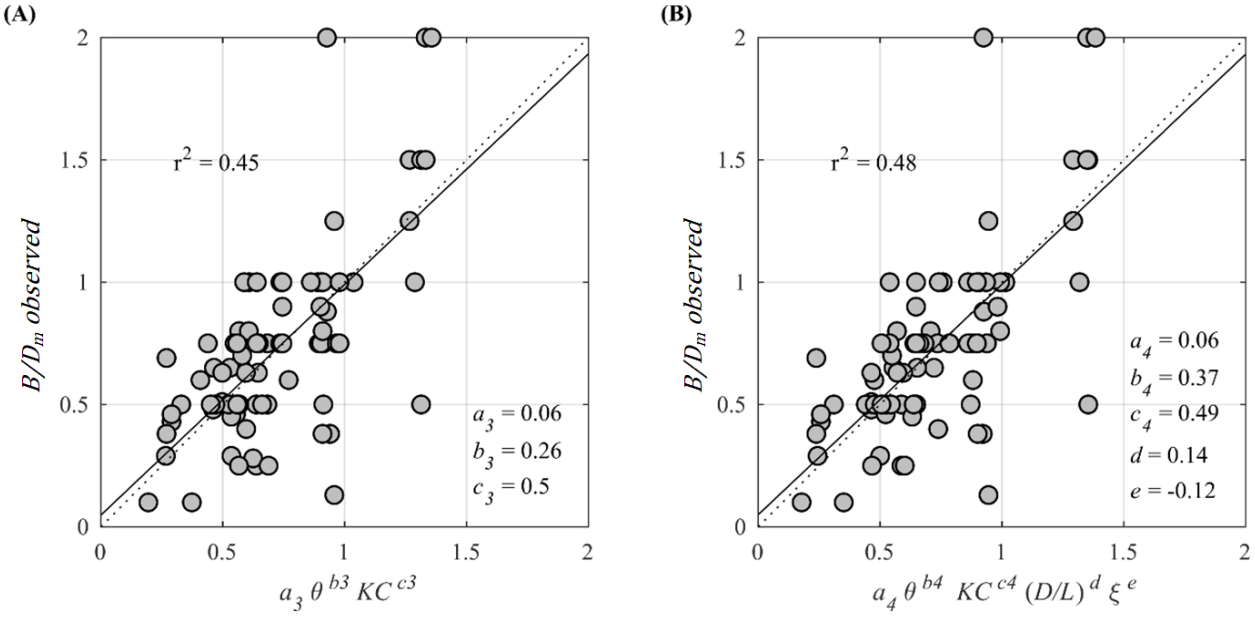

Figure 18. Observed versus predicted dimensionless burial depth using different empirical formulations (A and B).

Additional model tests of the form $B/D_m = [aq_1{}^b q_2{}^c q_3{}^d \ldots]$ where q_i indicates a different dimensionless quantity were tested. A slight improvement is obtained incorporating the munition shape and the Iribarren number

$$B/D_m = a_4\,\theta^{b_4} KC^{c_4} \left(\frac{D}{L}\right)^d \xi^e. \qquad (21)$$

The coefficients a_4 = 0.07 and c_4 = 0.49 are similar to a_3 and c_3 obtained for equation (20); while b_4, d and e are 0.35, 0.14, and -0.12 respectively. The squared correlation coefficient improves by only 0.03 (Figure 18B) which must be weighed against the inclusion of three additional fitting coefficients. Removing ξ decreases the correlation by 0.01 with r^2 = 0.48.

Migration was also correlated with θ_m and $\theta_{m\,mod}$. A nonlinear least squares regression analysis was conducted, similar to that for burial data. θ_m (and $\theta_{m\,mod}$) alone cannot fully explain the migration processes. The squared correlation coefficient found is nearly zero (r^2 = 0.05). Adding the ratio ρ_m/ρ_w increases r^2 substantially (r^2 = 0.27) confirming that density plays a fundamental role in migration processes. The semi-empirical formulation with the highest r^2 (0.37) found is

$$|d_x| = a_5 \theta_{m\,mod}{}^{b_5} \left(\frac{\rho_m}{\rho_w}\right)^{c_5} \xi^{\,d_5}, \quad (22)$$

yielding $a_5 = 25.65$, $b_5 = 0.75$, $c_5 = -2.59$ and $d_5 = -0.26$. Other parameters such as runup, foreshore slope alone (not included in the Iribarren number) and the initial orientation of the munition were tested without significant improvement in correlation.

4.4 Migration and Burial Time Evolution

4.4.1 Application of IMU algorithm for migration and algorithm reliability

Application of the IMU algorithm, for run 58 and a 81-mm munition is shown in Figure 19 as an example. IMU data are compared with data obtained using imagery. Time series are shown only for a window of 92 s until munition motion ceased. The first two panels (Figure 19A and Figure 19B) contain IMU measurements. Raw roll angle ranges from -180 to 180° (Figure 19A), and oscillates with each wave indicative of munition rolling. The instantaneous orientation of the munition (Figure 19B) determined with the IMU (solid line) follows the trend estimated from imagery (circles). The cumulative angle of rotation (Figure 19C) is positive with a final value corresponding to nearly 14 rotations offshore. Finally, the cross-shore migration d_x (magenta) matches well that derived from imagery (filled circles; Figure 19D). The background image is the corresponding time stack obtained from C1 while the black filled circle indicates the x coordinate of the munition surveyed by the RTK GPS at the end of the run.

The munition of interest was deployed at the shoreline (circled in Figure 19E at t_1) with an initial orientation of 186°. The munition remained fixed until roughly 50 s when it was impacted by the 4th wave of the run. The orientation changed such that x_m went from roughly perpendicular to roughly parallel to the shoreline (from 186° to 98°). An onshore migration of 0.3 m was followed by a 1.5 m offshore migration (snapshots in Figure 19E at t_2 and t_3) before the munition motion stopped (circled in Figure 19E at t_4). Imaged-derived and IMU positions align until they diverge towards the end of this offshore motion with an offset of 0.46 m at 56.22 s. A similar behavior of net offshore migration is evident for the next two waves. After each swash event, the munition stopped in a location more offshore than the previous. During the 7th wave of the run, the munition moved again with net offshore transport. This time the motion was detected only from the IMU and not from the imagery due to lack of visibility. The IMU heading measurement indicates a change of orientation from 98° to 17° and hence x_m was again roughly perpendicular to the shoreline. After t_5, the munition remained fixed as indicated by a constant IMU x = 1.73 m. The angle differences between IMU- and image-derived headings are generally less than 20° for this specific case. The largest error between image-derived and IMU-derived cross-shore locations is 0.7 m. Migration was captured from C1 only towards the ends of backwash due to visibility issues. Post-run cross-shore munition position surveyed with the RTK GPS yielded a difference of 0.19 m if compared with the IMU-derived position. The munition, when mobilized, showed the same trend of motion for each swash event; a small onshore movement followed by a larger offshore migration.

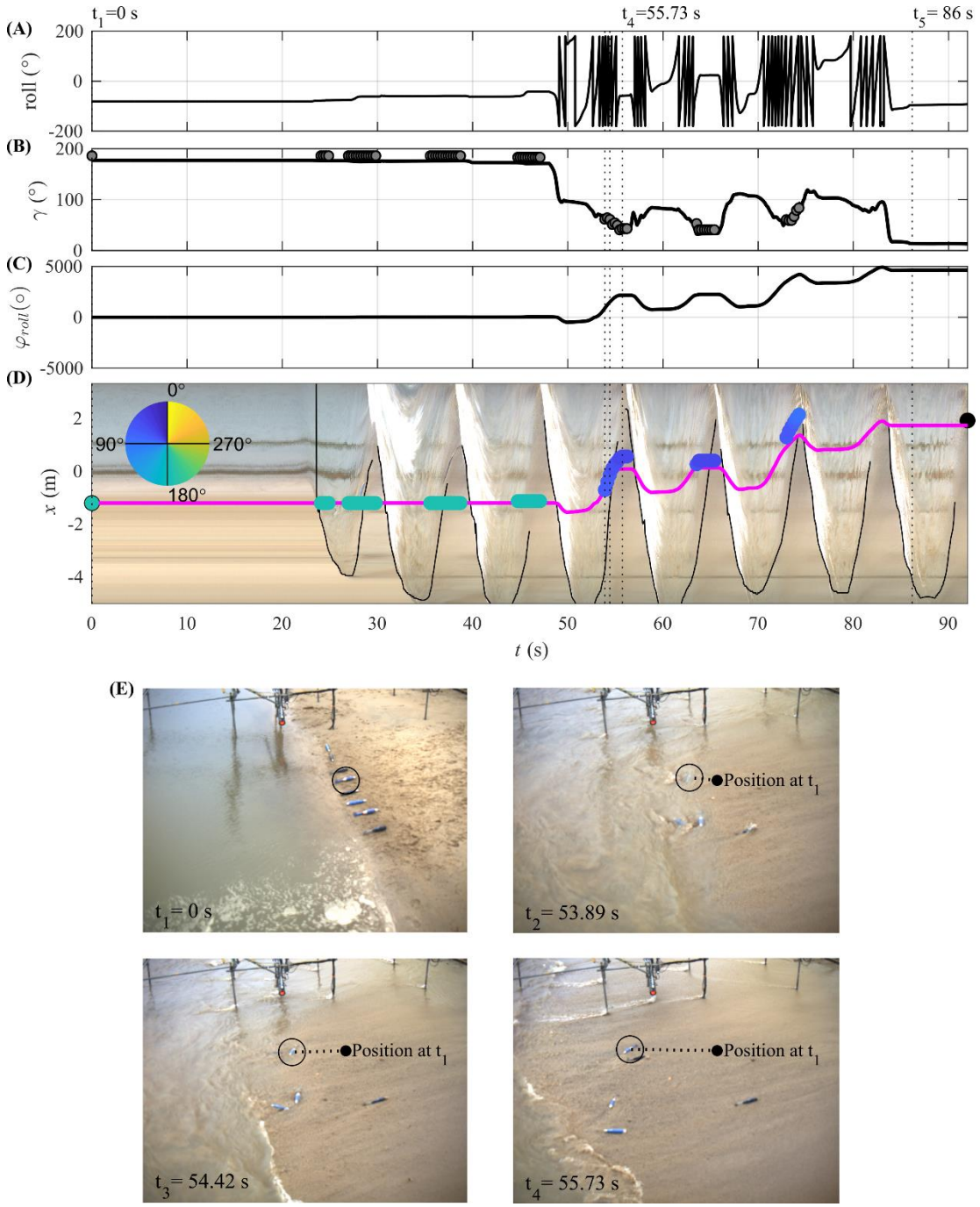

Figure 19. IMU algorithm application for run 58 and a 81-mm munition. Comparisons between IMU-derived and image-derived heading and cross-shore trajectories. A) Raw IMU roll measurements. B) Heading of x_m estimated from IMU yaw measurements (solid line) and imagery (circles). C) Cumulative angle of rotation. D) Munition cross-shore trajectory (magenta line) and image-derived cross-shore locations (circles). The background represents a time stack from imagery highlighting the runup curve (black line). The color wheel indicates the munition orientation. E) Snapshots of four instants of time from t_1 to t_4. The initial and subsequent positions of the 81-mm munition of interest are identified.

Munition trajectories and post-run positions derived from the IMU are affected by error. The RTK GPS and imagery were used to determine the magnitude of the IMU error for swash zone and breaker zone munitions. Post-run RTK GPS surveys were compared with the post-run locations derived from IMU for cross-shore (Figure 20A) and alongshore components (Figure 20B). The least squares fit for cross-shore (alongshore) migration has a slope of 0.69 (0.8) and an intercept of 0.05 (-0.15) with a squared correlation coefficient, r^2 of 0.62 (r^2 of 0.51). A similar analysis was carried out to compare munition locations derived from the IMU with those derived from imagery, solely for swash zone cases (cross-shore, Figure 20C; alongshore, Figure 20D). Larger error is estimated for cross-shore motion (r^2 of 0.49) if compared to the alongshore direction (r^2 of 0.75) for the IMU. Slopes and intercepts of least squares fits are 0.68 and -0.48 for cross-shore and 0.85 and -0.97 for alongshore respectively.

4.4.2 Migration time evolution observations

The developed IMU algorithm was applied to all available LWE cases for 155-mm, 81-mm and RKT munitions deployed in the swash and breaker zones. For both regions, cases were separated into two categories based on the total migration: no motion (motion less than 0.05 m) and motion (motion greater than 0.05 m). There were 31 cases for no motion and 40 cases for motion in the swash zone (Table 7; "IMU"). The corresponding numbers for the breaker zone munitions were 225 and 37 (Table 7; "IMU").

Swash zone observations of cross-shore migration are shown for the three munition types (Figure 21) only for cross-shore migration and for cases of motion. Thirty-two out of 40 cases of motion are associated with the steeper foreshore slope (LWE2; blue curves). The majority of the cases (34 out of 40) belong to RKT and 81-mm munitions. The RKT and 81-mm, of comparable length and diameter, often migrated up to 4 m offshore with some exceptions up to 8 m. In addition, RKT and 81-mm often mimicked the runup curve, rolling upslope during uprush and downslope during backwash (with incremental net motion offshore). The maximum offshore migration for the few cases of motion for the 155-mm munition (6 out of 40) was ~ 4 m. The 155-mm munitions did not mimic the RKT and 81-mm in terms of intra-wave onshore and offshore motions and instead migrated more erratically with a net offshore motion. Migration does not appear to be correlated solely to the forcing (θ) as the largest traveled distances are not always related to the largest forcing (identified from prior correlation analysis). The modified object mobility number ranges ascribed the three munitions were 0.52 – 0.98 for RKT, 0.16 – 0.33 for 155-mm and 0.33 – 0.68 for 81-mm. The largest migration distances for RKT (8.7 m), 155-mm (3.9 m) and 81-mm (8.2 m) occurred for $\theta_{m\ mod}$ of 0.75, 0.24 and 0.40 respectively; again showing inconsistent variability in migration distance as a function of the forcing.

Breaker zone munition cases experienced less motion compared to the swash zone munition cases. There are 37 cases of motion against 125 cases of no motion (Table 7; "IMU"), occurring for 81-mm and RKT munitions only. Trajectories for the 81-mm munition (not shown) are confined within an onshore migration of 1 m and an offshore migration of 0.5 m. The corresponding values for the RKT were 1 m and 2 m respectively. No dominance in motion direction (onshore, offshore) was observed.

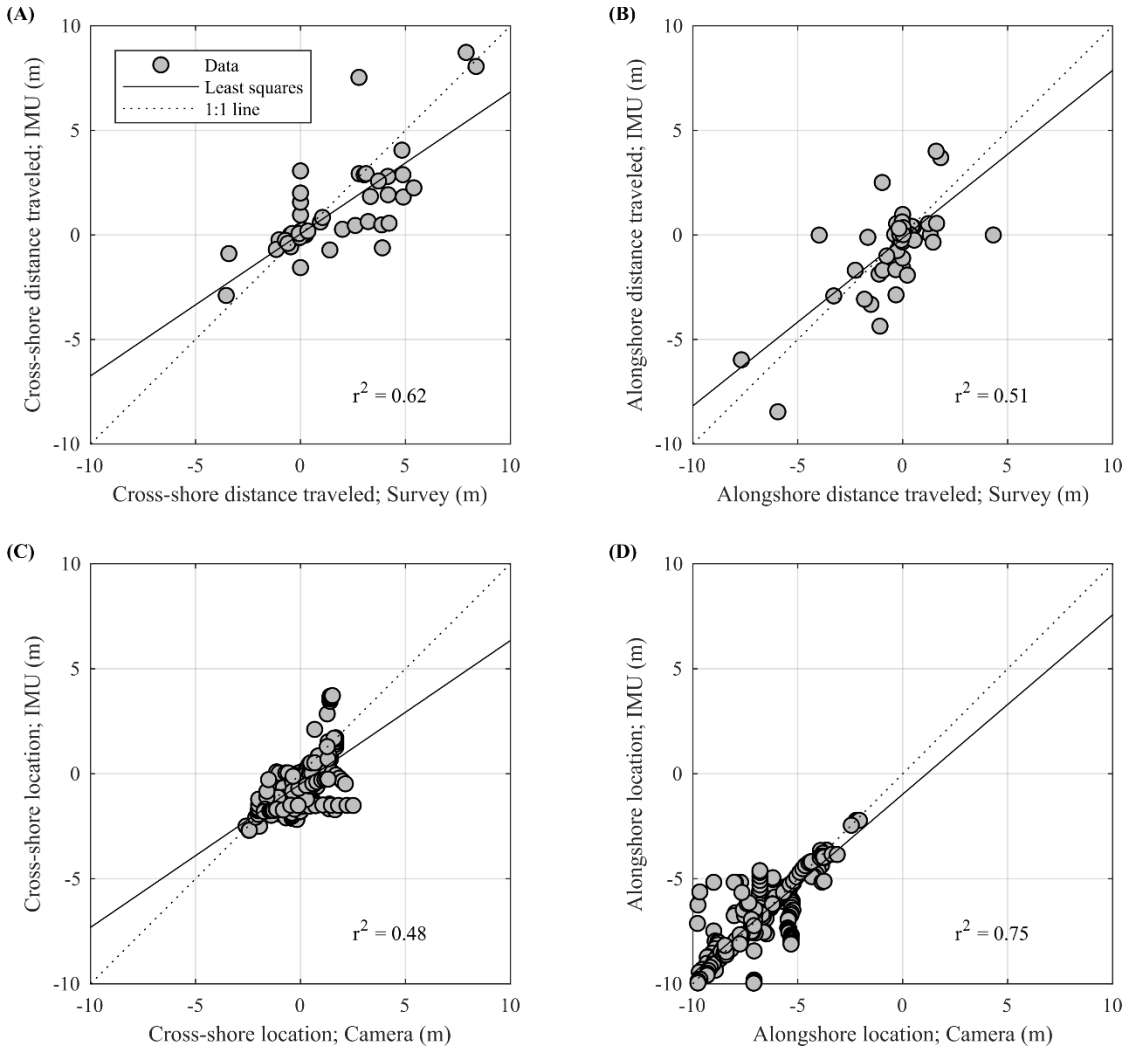

Figure 20. Cross-shore (A) and alongshore (B) munition distance traveled for GPS surveys and IMU derivations. Cross-shore (C) and alongshore (D) munition locations for imagery and IMU derivations. Least squares (solid) and 1:1 lines (dashed) are shown.

4.4.3 Application of photocells burial algorithm and algorithm reliability

An example from run 52 from LWE2 illustrates the approach to identify apparent burial time history (Figure 22). The munition was deployed proud at the shoreline (snapshot taken from UC; Figure 22G, t_1). The munition rolled offshore less than a complete rotation during the first five swash events and became buried roughly half of its diameter. Panels A-E are sub-divided into three time windows corresponding to the beginning of the run (0 - 10 s), the section where the munition rolled (20 - 120 s) and the end of the run (310 - 330 s). The first two panels (Figure 22A and Figure 22B) indicate the hydrodynamics showing water depth and cross-shore flow velocities respectively. Water depths started with values of 0.26 m and decreased to 0.20 m at approximately t_3. Velocity magnitudes reached maxima of 1.2 m/s for the uprush and 1.6 m/s for the backwash. The initial φ_{roll} was 109.8° indicating a munition orientation with PH08 and PH09 oriented downward. PH09 and PH04 had normalized voltages of roughly 0 and 1 respectively (Figure 22C; only five photocells out of 12 are shown for clarity). These photocell values match

the recorded initial deployment orientation. No motion occurred prior 30 s. At t_2, an offshore-directed rotation of 23.9° (from 109.8° to 133.7°; Figure 21D) caused PH09 to point downward (Figure 21H, t_2).

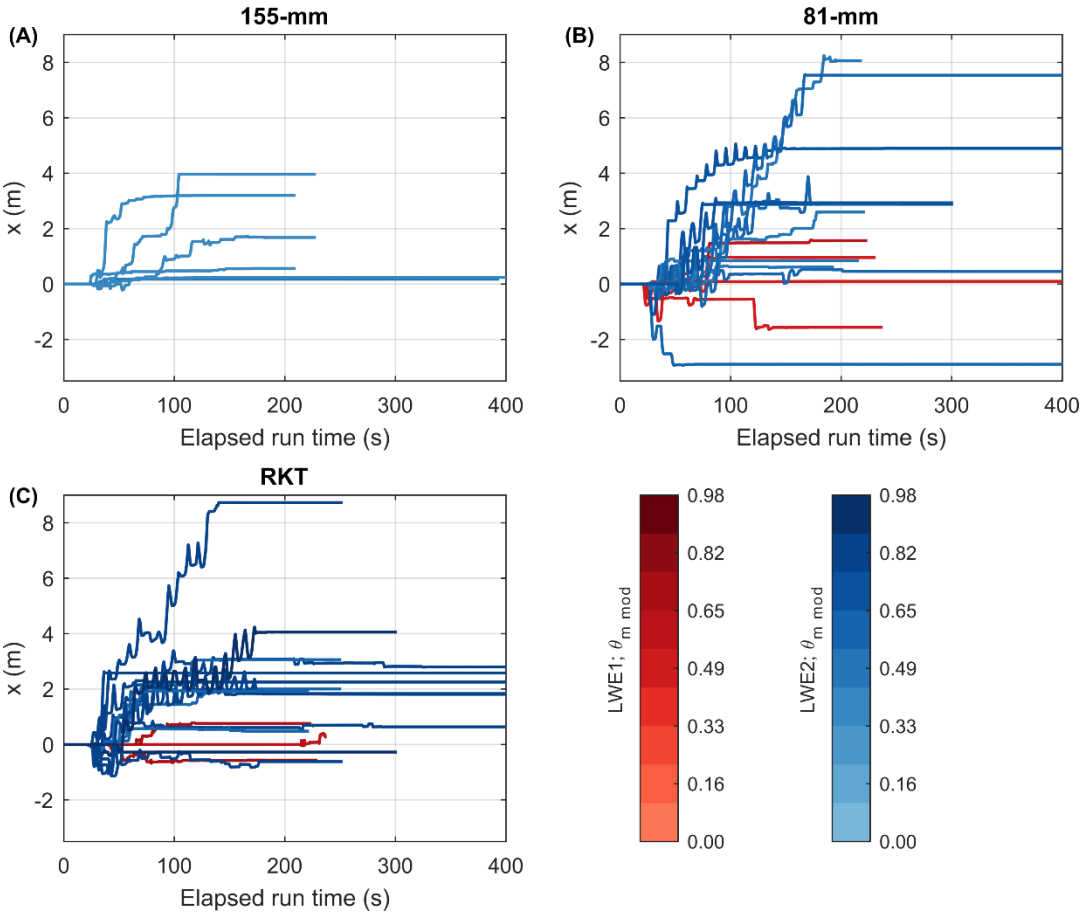

Figure 21. Swash zone munition cross-shore trajectories (when d_x > 0.05 m) derived from IMU for munitions 155-mm (A), 81-mm (B) and RKT (C). Each colorbar denotes a different foreshore steepness (red for tanβ = 1:16, blue for tanβ = 1:10). Colormaps refer to the modified object mobility number.

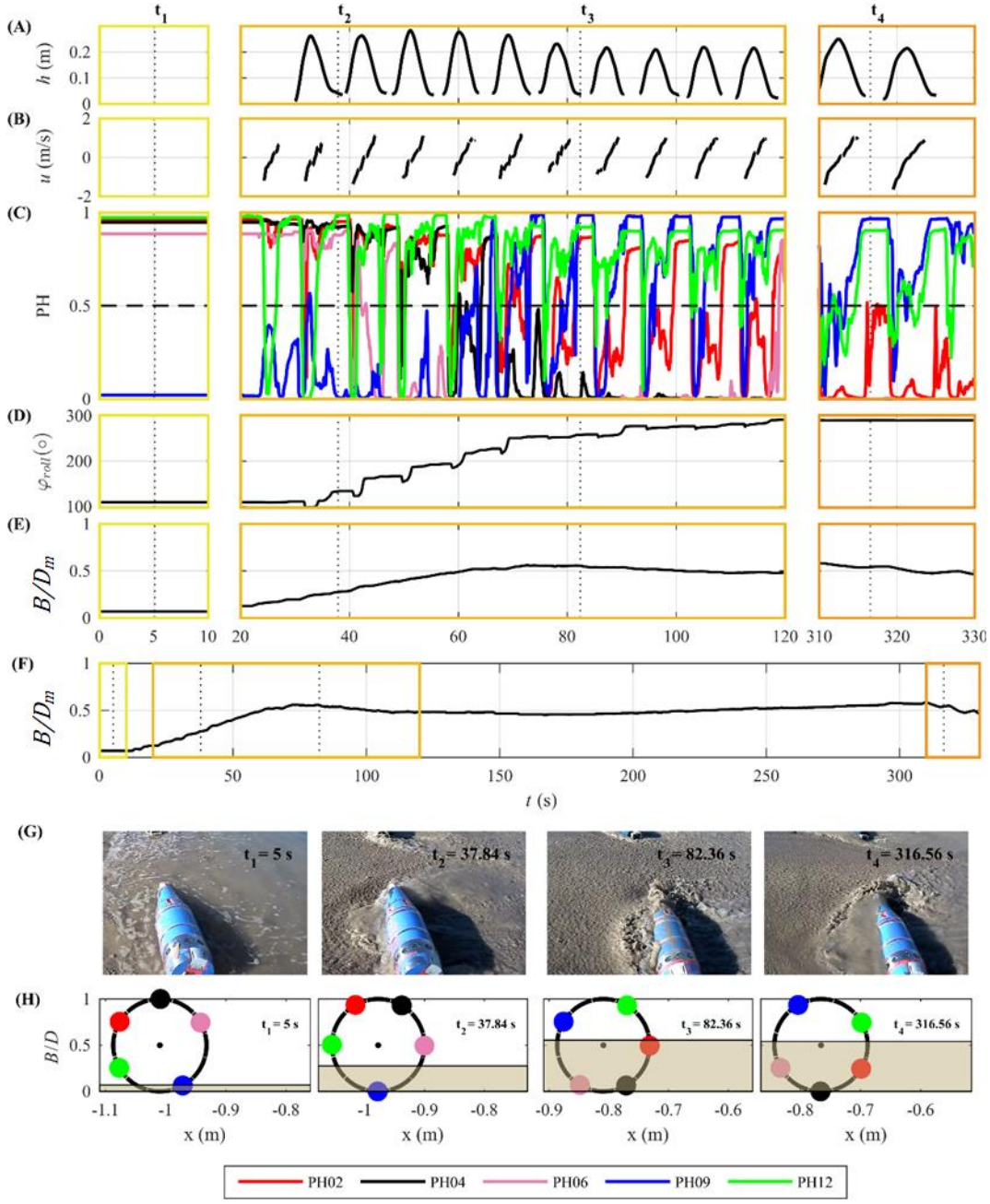

Figure 22. Example of 155-mm burial evolution derivation from photocells and IMU measurements (run 52). Panels A-E represent three sections of time, identified by the yellow boxes in panel F. A) Swash zone water depth. B) Swash zone cross-shore velocity. C) Normalized photocell voltage. D) Cumulative roll angle. E) and F) Time evolution of the munition dimensionless burial relative to the munition cross-shore section. G) Snapshots of the 155-mm at four different instants of time, t_1-t_4 (UC). H) 155-mm cross-sections (black circle) with locations of photocells PH02, PH04, PH06, PH09 and PH12 (color circles) derived from IMU and local bed level relative to munition cross-section derived from PH at four instants of time, t_1-t_4.

The relative bed level was 0.27 (Figure 22E, 22F and 22H) and PH02 and PH04 had a normalized voltage of nearly 1 (Figure 22C). Between t_2 and t_3 the munition continued rolling offshore. The rotation angle was 124.6° (from 133.7° to 258.3°; Figure 22D) leading to PH04 and PH06 being oriented downward (Figure 22H, t_3). Both PH04 and PH06 had a normalized voltage of 0 while PH09 and PH12 had a signal near 1 (Figure 22H). Normalized burial depth, B/D_m, reached a maximum value of 0.55 (Figure 22E, 22F and 22H). After t_3 the munition rolled slightly more offshore with PH04 oriented downward (Figure 22H at t_4) and PH02 having normalized voltage less than 0.5. Within the time window 120-310 s, the munition remained fixed with no appreciable changes in burial.

The burial detected from the photocell array at the end of each run was compared (least squares) to the corresponding post-run survey of burial status to estimate the errors in the developed algorithm (Figure 23). The best fit line is characterized by a slope of 0.88, an intercept of 0.04, and an r^2 of 0.73. However, the judgement parameter (manual burial measurements) is affected by the discretized nature of collection described earlier; an error of ± 25%.

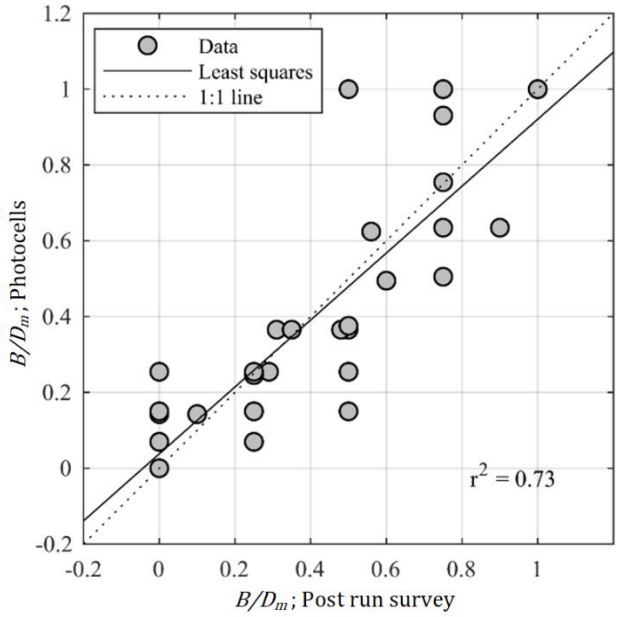

Figure 23. Dimensionless burial depth from the post-run survey versus the final dimensionless burial depth obtained from the photocells (grey circles). Least squares (solid) and 1:1 lines (dashed) are shown.

4.5 Field Study of Migration and Burial

Munitions were deployed initially at different (x,y) locations. Throughout the experiment, munitions were surveyed only when they were found. Tables 8 and 9 provide the surveys made for each munition reporting the survey time, the status, the x and y coordinates and the dimensionless burial depth, B/D_m. The burial depth, B, was measured as the vertical distance from the local bed level to the bottom of the munition. The status indicates whether the munition was deployed (D), found and surveyed (S) or retrieved (R). Table 8 groups together the surveys of retrieved munitions while Table 9 is dedicated to munitions that were never recovered. Only

22 out of 50 munitions deployed were retrieved at the end of the experiment highlighting the difficulty in deploying objects in the nearshore even when contained by a fence.

Table 8. Surveys of x,y position and burial relative to local bed level for long term deployed munitions that were retrieved before the end of the experiment. The acronyms 'D', 'S' and 'R' stand for Deployed, Surveyed, Retrieved.

UXO	Status	Time	B/D_m	x (m)	y (m)	UXO	Status	Time	B/D_m	x (m)	y (m)
S204	D	8/24/2020 14:02	0.0	11.5	-5.5	SRKT3	D	8/24/2020 14:01	0.0	17.6	-5.6
S204	S	8/28/2020 14:01	14.8	15.4	-5.7	SRKT3	S	10/4/2020 9:01	0.5	26.0	-8.3
S204	S	8/30/2020 17:05	8.0	13.9	-5.1	SRKT3	R	10/5/2020 10:00	1.3	25.9	-8.3
S204	R	10/22/2020 13:00	1.0	24.7	-2.7	SRKT4	D	8/24/2020 14:03	0.5	11.3	-11.1
SBLU2	D	8/24/2020 14:04	0.0	4.1	-6.3	SRKT4	R	8/28/2020 15:00	2.7	NaN	NaN
SBLU2	S	8/27/2020 18:00	0.5	4.1	-6.4	SRKT5	D	8/24/2020 14:03	1.0	11.4	-14.6
SBLU2	R	8/28/2020 16:04	0.5	4.2	-6.4	SRKT5	S	10/4/2020 9:04	1.0	26.0	-13.0
SBLU3	D	8/24/2020 14:04	0.5	4.5	-11.0	SRKT5	R	10/5/2020 9:05	1.4	26.0	-13.0
SBLU3	S	8/27/2020 18:00	0.5	4.5	-11.1	S1553	D	8/24/2020 13:05	0.0	20.4	13.9
SBLU3	S	8/28/2020 16:04	0.5	4.5	-11.0	S1553	S	8/28/2020 15:04	1.4	20.7	13.6
SBLU3	S	9/4/2020 10:00	0.5	4.5	-11.1	S1553	S	8/31/2020 17:04	1.1	20.6	13.9
SBLU3	S	9/7/2020 10:03	0.8	4.5	-11.0	S1553	S	9/7/2020 11:00	2.0	20.6	13.8
SBLU3	S	9/10/2020 13:04	1.3	8.0	-20.6	S1553	S	9/10/2020 14:00	1.0	20.7	13.2
SBLU3	S	10/3/2020 10:01	1.0	23.4	-21.7	S1553	R	10/10/2020 14:04	3.1	19.7	14.3
SBLU3	R	10/5/2020 10:03	3.0	23.5	-21.6	I402	D	8/24/2020 14:05	0.5	11.1	19.8
SBLU4	D	8/24/2020 14:04	1.0	4.4	-14.0	I402	S	8/27/2020 15:00	4.8	NaN	NaN
SBLU4	S	8/28/2020 16:04	1.0	4.4	-14.0	I402	R	8/28/2020 16:01	9.8	20.7	18.9
SBLU4	S	9/10/2020 13:05	1.5	13.9	-5.1	I402	D	8/28/2020 16:03	0.5	10.6	16.5
SBLU4	R	10/5/2020 11:00	2.8	26.6	-26.1	I402	S	8/31/2020 17:01	2.3	15.0	21.8
SBLU6	D	8/24/2020 14:04	0.0	7.5	-13.8	I402	S	9/4/2020 9:03	7.0	15.0	21.8
SBLU6	S	8/27/2020 18:00	1.7	7.4	-13.7	I402	S	9/7/2020 11:01	6.5	14.9	21.7
SBLU6	S	9/10/2020 13:04	1.1	7.4	-13.3	I402	S	9/10/2020 14:00	3.5	14.8	21.8
SBLU6	S	9/21/2020 12:03	3.0	7.2	-13.4	I402	R	10/9/2020 13:02	9.8	15.3	21.5
SBLU6	R	10/8/2020 12:03	4.3	7.6	-13.2	I811	D	8/24/2020 14:02	0.0	17.1	-22.9
S812	D	8/24/2020 14:01	0.0	17.7	-10.2	I811	S	8/28/2020 15:03	3.5	25.2	-23.4
S812	S	8/28/2020 15:01	2.5	22.6	-11.9	I811	S	9/7/2020 10:05	2.9	25.2	-23.4

S812	S	9/7/2020 10:05	3.1	22.6	-11.9	I811	R	10/5/2020 10:05	2.9	25.3	-23.4
S812	S	10/3/2020 9:05	1.0	23.3	-11.5	I813	D	8/24/2020 14:01	0.5	17.6	21.1
S812	R	10/19/2020 11:03	4.2	23.3	-11.6	I813	R	10/8/2020 13:02	3.5	23.9	23.4
S815	D	8/24/2020 14:00	1.0	17.8	11.0	IRKT1	D	8/24/2020 14:03	0.0	11.3	-17.5
S815	S	8/30/2020 16:03	1.0	24.5	11.6	IRKT1	R	10/19/2020 11:00	5.3	24.4	-20.9
S815	R	10/8/2020 13:05	4.7	24.1	11.7	IRKT2	D	8/24/2020 14:03	0.5	11.6	-21.0
S816	D	8/24/2020 14:02	0.0	17.7	-14.7	IRKT2	R	8/28/2020 15:02	1.0	25.9	-27.3
S816	R	8/28/2020 14:03	3.6	19.8	-18.5	IRKT2	D	8/30/2020 18:01	0.5	11.8	-14.0
S816	D	8/30/2020 18:01	0.0	15.4	-8.1	IRKT2	R	10/5/2020 10:05	3.9	24.8	-19.6
S816	S	8/31/2020 16:05	1.2	20.6	-7.9	I1551	D	8/24/2020 13:05	0.0	20.1	18.7
S816	S	9/4/2020 9:04	1.0	20.5	-7.9	I1551	S	8/28/2020 16:01	1.6	20.2	19.0
S816	S	9/7/2020 10:04	3.8	20.5	-8.0	I1551	S	8/31/2020 17:04	1.1	20.0	18.7
S816	R	9/19/2020 11:02	0.8	14.0	-6.4	I1551	S	9/7/2020 11:00	2.1	20.3	18.8
S817	D	8/24/2020 14:00	0.5	17.9	13.7	I1551	R	10/8/2020 15:00	3.6	19.9	18.6
S817	R	8/28/2020 15:05	2.6	20.7	13.8	I1552	D	8/24/2020 13:05	0.0	20.0	25.1
SRKT2	D	8/24/2020 14:02	0.0	11.4	-8.1	I1552	S	8/28/2020 16:02	1.8	19.8	25.2
SRKT2	R	8/28/2020 15:01	2.7	23.3	-10.2	I1552	S	8/31/2020 17:04	1.1	19.9	25.0
SRKT2	D	8/30/2020 18:01	0.0	11.4	-8.4	I1552	R	10/9/2020 14:03	2.7	19.0	24.4
SRKT2	R	8/31/2020 17:00	0.0	NaN	NaN	I1553	D	8/24/2020 14:01	0.0	17.5	25.4
SRKT2	D	8/31/2020 17:00	0.0	7.1	-8.9	I1553	S	8/30/2020 16:05	1.8	17.8	25.3
SRKT2	S	9/4/2020 9:05	1.0	25.1	-19.2	I1553	R	10/8/2020 14:04	2.3	16.5	24.9
SRKT2	S	9/7/2020 10:05	2.4	24.9	-19.0						
SRKT2	R	9/19/2020 11:01	0.8	14.6	-6.4						

Table 9. Surveys of x,y position and burial relative to local bed level for long term deployed munitions that went lost. The acronyms 'D', 'S' and 'R' stand for Deployed, Surveyed, Retrieved.

UXO	Status	Time	B/D_m	*x* (m)	*y* (m)	UXO	Status	Time	B/D_m	*x* (m)	*y* (m)
S201	D	8/24/2020 14:03	0.0	9.6	-5.4	SBLU7	D	8/24/2020 14:04	0.0	7.1	-20.0
S201	S	8/30/2020 17:05	8.0	14.2	-6.4	SBLU7	S	8/28/2020 14:05	2.2	22.8	-22.2
S201	S	9/10/2020 13:05	5.5	14.2	-6.3	SBLU7	S	8/30/2020 17:04	3.7	22.7	-22.2
S202	D	8/24/2020 14:03	0.5	9.2	-9.5	SBLU7	S	8/31/2020 16:04	2.0	22.7	-22.1
S203	D	8/24/2020 14:03	1.0	9.2	-12.5	SBLU7	S	9/7/2020 10:04	2.6	22.9	-22.1
S203	S	8/30/2020 17:05	8.0	14.5	-13.4	S813	D	8/24/2020 13:05	0.0	18.0	6.4

S203	S	9/10/2020 13:05	4.0	14.5	-13.4	S814	D	8/24/2020 14:00	0.5	17.9	8.4
S205	D	8/24/2020 14:02	0.0	14.3	-6.8	S814	S	8/30/2020 17:01	2.2	24.9	7.1
S205	S	8/31/2020 17:00	7.0	19.2	-7.0	S814	S	8/31/2020 17:02	0.0	24.4	7.5
S401	D	8/24/2020 14:05	0.0	6.9	7.8	S814	S	9/4/2020 9:02	1.0	24.5	7.3
S401	S	8/29/2020 16:05	3.5	22.8	5.2	S1552	D	8/24/2020 13:04	0.0	20.4	8.5
S402	D	8/24/2020 14:05	0.0	9.6	7.3	S1552	S	8/28/2020 15:03	1.4	20.5	8.4
S402	S	8/29/2020 16:02	5.5	19.2	6.6	S1552	S	8/31/2020 17:04	1.1	20.5	8.1
S402	S	8/31/2020 17:01	1.0	18.9	6.9	I201	D	8/24/2020 14:03	0.0	9.3	-15.8
S403	D	8/24/2020 14:05	0.0	12.2	4.8	I201	S	8/28/2020 14:04	4.5	20.4	-19.1
S403	S	8/27/2020 17:05	7.3	17.2	5.2	I201	S	8/30/2020 17:04	8.5	20.2	-19.0
S403	S	8/29/2020 16:02	6.0	17.3	5.1	I202	D	8/24/2020 14:04	0.5	9.4	-19.1
S403	S	8/31/2020 17:01	3.5	17.3	5.2	I202	S	8/28/2020 14:04	4.5	20.6	-19.1
S403	S	9/10/2020 14:00	1.0	17.3	5.1	I203	D	8/24/2020 14:04	1.0	9.7	-23.6
S404	D	8/24/2020 14:05	0.5	12.0	9.4	I203	S	8/28/2020 15:01	4.8	25.6	-24.7
S404	S	8/27/2020 17:05	7.3	16.6	8.7	I401	D	8/24/2020 14:05	0.0	11.4	16.5
S404	S	8/31/2020 17:01	3.5	16.8	8.7	I401	S	8/28/2020 15:05	2.8	23.2	14.0
S404	S	9/10/2020 14:00	1.0	16.7	8.5	I403	D	8/24/2020 14:05	1.0	11.0	24.3
S405	D	8/24/2020 14:05	1.0	11.7	13.0	IBLU1	D	8/24/2020 14:04	0.0	5.2	-18.2
S405	S	8/28/2020 15:05	4.8	23.0	12.5	IBLU1	S	8/27/2020 18:00	0.0	1.9	-19.4
S406	D	8/24/2020 14:05	0.5	8.7	14.1	IBLU1	S	8/28/2020 16:04	0.0	1.9	-19.4
S407	D	8/24/2020 13:05	0.0	17.8	3.1	IBLU1	S	9/4/2020 10:00	0.5	1.9	-19.4
S407	S	8/27/2020 17:05	5.3	18.7	3.0	IBLU1	S	9/7/2020 10:03	0.8	1.9	-19.4
S407	S	8/31/2020 17:02	3.5	18.9	3.1	IBLU2	D	8/24/2020 14:04	0.5	5.5	-21.7
S408	D	8/24/2020 13:04	0.0	20.7	3.8	IBLU2	S	8/27/2020 18:00	0.5	5.5	-21.6
S408	S	8/29/2020 16:03	5.5	22.3	0.3	IBLU2	S	8/28/2020 16:05	0.5	5.5	-21.7
S409	D	8/24/2020 15:00	0.5	6.6	14.1	IBLU2	S	9/4/2020 10:00	0.8	5.5	-21.7
S409	S	8/28/2020 15:05	3.5	21.6	16.9	IBLU3	D	8/24/2020 14:04	1.0	5.9	-25.2
S409	S	9/4/2020 9:03	1.0	20.8	16.5	IBLU3	S	8/27/2020 18:00	1.2	5.9	-25.1
SBLU5	D	8/24/2020 14:04	0.0	7.3	-9.3	I812	D	8/24/2020 14:00	1.0	17.5	17.4
SBLU5	S	8/28/2020 14:02	3.9	14.8	-11.5	I812	S	8/29/2020 16:04	2.9	23.9	18.8
SBLU5	S	8/30/2020 17:04	2.5	14.8	-11.5	I812	S	8/31/2020 17:04	0.0	24.0	18.7
SBLU5	S	8/31/2020 16:04	3.5	14.7	-11.5	IRKT3	D	8/24/2020 14:03	1.0	12.3	-24.2
SBLU5	S	9/4/2020 10:00	1.0	14.8	-11.5	IRKT3	S	8/31/2020 16:05	3.1	24.6	-26.2

SBLU5	S	9/7/2020 10:04	5.7	14.8	-11.4	IRKT3	S	9/4/2020 9:05	1.0	24.6	-26.2
SBLU5	S	9/10/2020 13:05	2.0	14.8	-11.5	IRKT3	S	9/7/2020 10:04	3.9	24.6	-26.2

Migration is defined as the distance traveled by a munition between two subsequent surveys, respectively at time t_{i-1} and t_i. The migration components d_x and d_y are calculated as

$$d_x = x_i - x_{i-1};\ d_y = y_i - y_{i-1}. \tag{23}$$

Similarly, the rate of change of the burial depth, ΔB, is given by the difference between burial depths at times t_i and t_{i-1}

$$\Delta B = B_i - B_{i-1}. \tag{24}$$

Equations (23) and (24) are used when munitions status at times t_{i-1} and t_i are one of the following: deployed-surveyed (D-S); surveyed-surveyed (S-S); deployed-retrieved (D-R); or surveyed-retrieved (S-R). In total, 129 observations of migration and burial were made.

4.5.1 Migration distances and morphological effects on munition burial

Migration distances d_x and d_y (Figure 24A) belong to munitions with different physical characteristics of shape, density and dimensions. The munition diameter is chosen to differentiate munitions in the figure and is represented based on color (dark color for larger munitions). Note that the observations are relative to the entire experiment (roughly two months) meaning that some migration distances occurred during calmer conditions (August) and some others during energetic conditions. Additionally, the difference between t_i and t_{i-1} ranged between 1 and 55 days with the average being 9 days. Therefore, there is considerable variation in migration distance associated with different munition physical characteristics, different time scales and different forcing conditions. Some munitions remained in place and are identified by a vector resultant migration distance of less than 0.05 m. A conservative threshold of 0.05 m is chosen to take into account the horizontal RTK GPS accuracy of about 0.02 m. Of the 129 observations, 56% migrated based on the previous definition. Cross-shore migration was observed to be more frequently oriented offshore (71%) with a maximum seaward migration of 17.9 m and maximum landward migration of 10.3 m. In the alongshore, the preferred direction was negatively (southerly) oriented (62%). The maximum d_y were -21 m and 12.6 m. The munition that reached y = -21 m, a BLU-61, was actually located at the fence; meaning it would have migrated farther alongshore if no barrier was present.

Figure 24B and 24C provide a comparison between the dimensionless rate of change of munition burial depth, $\Delta B/D_m$, and the dimensionless rate of change of the bed elevation, $\Delta z/D_m$ for the 129 observations. Δz was found differently depending on whether or not the munition was mobilized between the two subsequent surveys. If a munition experienced no migration ($x_i = x_{i-1}$), Δz was determined as the difference between the bed elevations at the munition cross-shore location at times t_i and t_{i-1}

$$\Delta z = z(x_i, t_i) - z(x_{i-1}, t_{i-1});\ if\ |x_i - x_{i-1}| \leq 0.15\ m, \quad (25)$$

where $z(x,t)$ is the RTK GPS beach profile elevation at cross-shore location x and time t (the beach profile closest to the munition is chosen). Instead, if the munition migrated between t_{i-1} and t_i, the rate of change becomes

$$\Delta z = z(x_i, t_i) - z(x_i, t_{i-1});\ if\ |x_i - x_{i-1}| > 0.15\ m. \quad (26)$$

A threshold of 0.15 m is chosen to account for measuring errors. The bed elevation rate of change is calculated for x_i in equation (26). Considering that the munition probably became exposed when at x_{i-1} and then migrated to x_i, B_{i-1} is set to zero in the ΔB calculation. The time at which the munition moved to position x_i is within t_{i-1} and t_i, but is unknown. Using the elevation z at time t_{i-1} is imprecise but is perhaps the best available choice.

Positive Δz identifies local bed accretion. Positive ΔB indicates an increase in burial depth. If burial processes were dominated solely by the beach morphology changes, the data should trend as the 1:1 line. Non-migration munitions represent 44% of the 129 observations and are reported in Figure 24B. Data show scatter around the 1:1 line which indicates near field processes (scour) also dictate munitions burial on the beach face. The first quadrant (Figure 24B) is where cases of accretion and burial occur. Similarly, the third quadrant is where cases of erosion and munition exposure occur. The first and third quadrant data (72%) make sense intuitively considering beach accretion (erosion) is expected to increase munition burial (exposure). The second quadrant contains munitions that became buried during an erosional event (15%). This scenario is possible through local scour processes even though the bed level decreased over time. Note that an initial dimensionless burial depth of either 0 or 1 characterizes all second quadrant data. The maximum subsequent burial is below three munition diameters; a small number for the smallest caliber munitions considering measurement errors in burial surveys. Measurement errors have a large impact on, for example, 20 mm munitions where an error of only 0.02 m translates to one D_m. The remaining 13% of data are located in the fourth quadrant; where the beach accreted and munition became exposed. The initial dimensionless burial depths ranged between 1.9 and 7. It is hard to imagine that a munition buried several or more diameters somehow exposed itself while the beach accreted. Instead, it is likely an erosional event exposed the munition first. Subsequently, the beach accreted but with slower munition burial processes.

Burial of mobilized munitions (56% of observations) is shown in Figure 24C. Unlike Figure 24B, only quadrants 1 and 2 are present based on the assumption the munition always began migration proud (initial relative burial of 0). The first quadrant contains 66% of the migration data. Despite scatter, data groups around the 1:1 line suggesting that generally if accretion occurs, burial depth also increases. Note how maximum $\Delta B/D_m$ and $\Delta z/D_m$ observed here are higher if compared to panel B. However, the smaller diameter munitions, 20-mm and 40-mm are the ones with accretion and burial both greater than 5 diameters. Several munitions showed burial rate equal to 0 despite deposition of sediment occurred. This is attributed to the fact that the munition (mobilized) did arrive at the final position after some time and probably closer to the survey time. The erosional-burial quadrant presents generally lower burials than quadrant 1 (mostly below 5). Looking at the general trend the burial rate decreases as the erosion rate increases (except for the two exceptional points referred to 20-mm and 40-mm) which make

sense considering that scour during erosion may occur but is not expected to make the munition achieving large burial depths. The 155-mm, although erosional events, are at least 1.3 diameter buried.

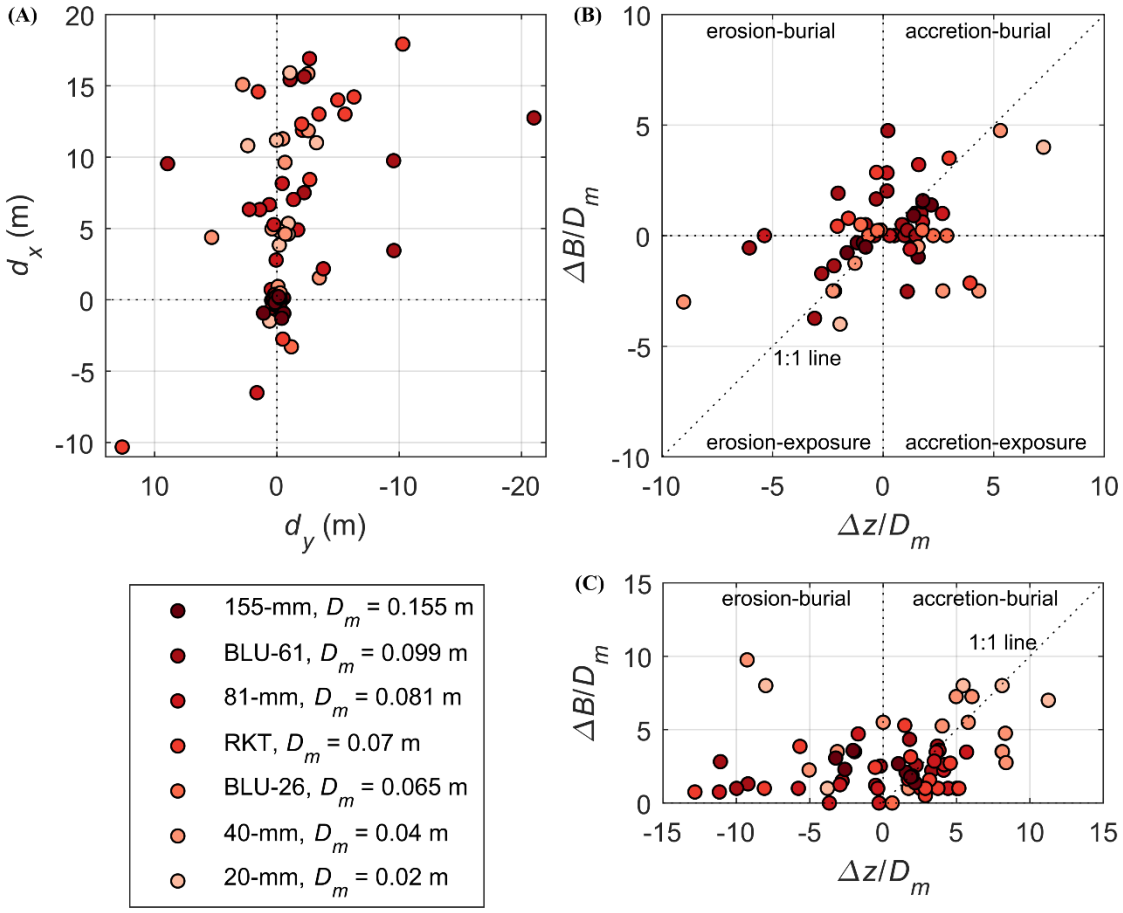

Figure 24. Long term deployed munitions observations. (A) Migration distances in x and y from initial (x,y) position. (B-C) Rate of change of the dimensionless burial depth as a function of the rate of change of the dimensionless beach morphology change for munitions that remained in place (B) or migrated (C). Color scheme is associated with munition diameter with darker colors for larger munitions.

4.5.2 Migration distances related to the hydrodynamics and the initial burial depth

The 129 observations were related to the hydrodynamics considering the burial depth at time t_{i-1}. In this regard, the Shields number, was chosen as a representative of the hydrodynamic intensity. Station 9 was chosen for Shields number calculations, as it is the most offshore station that recorded continuously (unlike the Vector that recorded in bursts). Nevertheless, data at Station 9 are available for the entire tidal cycle with swash zone occurring at low tide. For each recording hour, four flow velocity values were retained: the 95th percentiles of uprush, backwash, y^+, and y^- velocities. Thus, four values of bed shear stress are calculated for each hour, two in x and two in y: τ_{bx^+}, τ_{bx^-} , τ_{by^+} , τ_{by^-}. Consequently, four different Shields numbers are obtained: θ_{x^+}, θ_{x^-} , θ_{y^+} , θ_{y^-}. The reason behind retaining the sign of the Shields numbers for both x and y resides

in the desire of relating a cross-shore offshore (onshore) migration with the cross-shore offshore (onshore) directed Shields number (similarly for the alongshore direction).

The relationship between the migration distances d_x and d_y (already shown in Figure 24A) and the corresponding Shields numbers components is reported in Figure 25 considering also the burial status of the munition. In fact, a deeply buried munition has low probability of motion despite large Shields numbers, unless an erosional event takes place. A Shields number is associated to a migration component, d_x or d_y, as: if the munition migrated offshore ($d_x \geq 0$) between times t_{i-1} and t_i, the migration d_x is associated with the 95th percentile of all the cross-shore and offshore directed Shields components comprised between t_{i-1} and t_i (θ_{x95^+}, θ_{x95^-} , θ_{y95^+} , θ_{y95^-}). The maximum magnitude of θ_{x95} and θ_{y95} is less than 15 and 8.3 respectively. Cross-shore velocities and therefore cross-shore Shields numbers are larger as compared with the alongshore direction. The majority of the migration occurred for lower initial burial depths B_{i-1}, as expected.

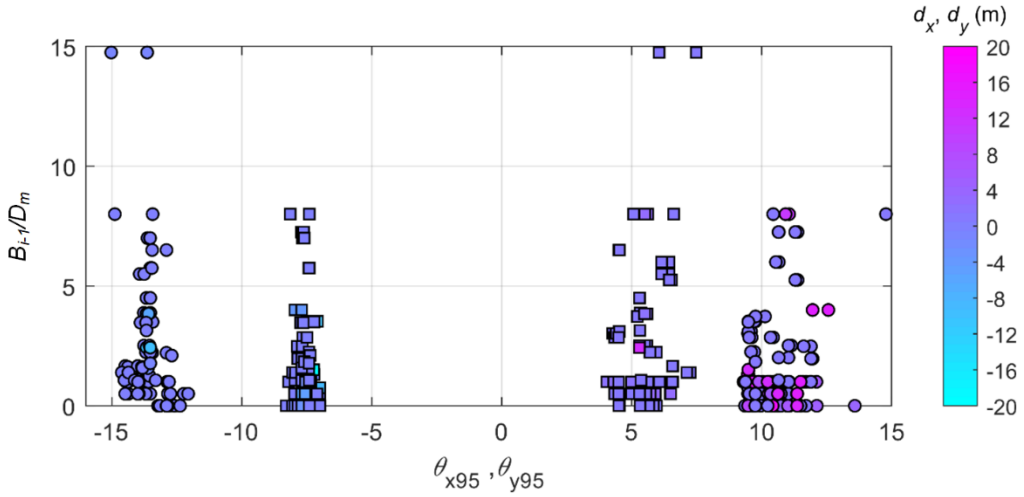

Figure 25. Comparison between migration distances and initial dimensionless burial depth observed for long term deployed munitions.

4.5.3 Instrumented munition observations

Ten munitions contained sensors for this part of the field study. Some of the munitions were deployed only once. Others were redeployed a second time providing a total of 14 munitions cases deployed with sensors. Unfortunately, some munitions were lost either the first or the second time they were deployed. In the end, nine cases are left and only seven with an IMU inside (the remaining two just with a PT). Out of this seven, three remained in place (a BLU-61 and two 155-mm) while the rest moved substantial distances (not shown). The IMU detected traveled distances of 5.8 and 8.5 m were offshore-directed for two 81-mm. The motion occurred after 2.5 hours and within 1 hour from the initial deployment respectively. Two RKT also migrated offshore, one migrating 9.7 m after 1 hour from deployment and another one traveled 0.7 m almost 2.5 hours after deployment.

The RKT that migrated 9.7 m offshore is taken as an example to show the trajectory detected from the IMU and corresponding hydrodynamics (Figure 26). The RKT was deployed at a cross-shore position (x = 11.4 m; y = -8.1 m) in between stations 4 and 5 on August 24th during a rising

tide (see d_x at minute 141 in Figure 26A between station 4 and 5; d_x and Station locations are referenced to x = 11.4 m).

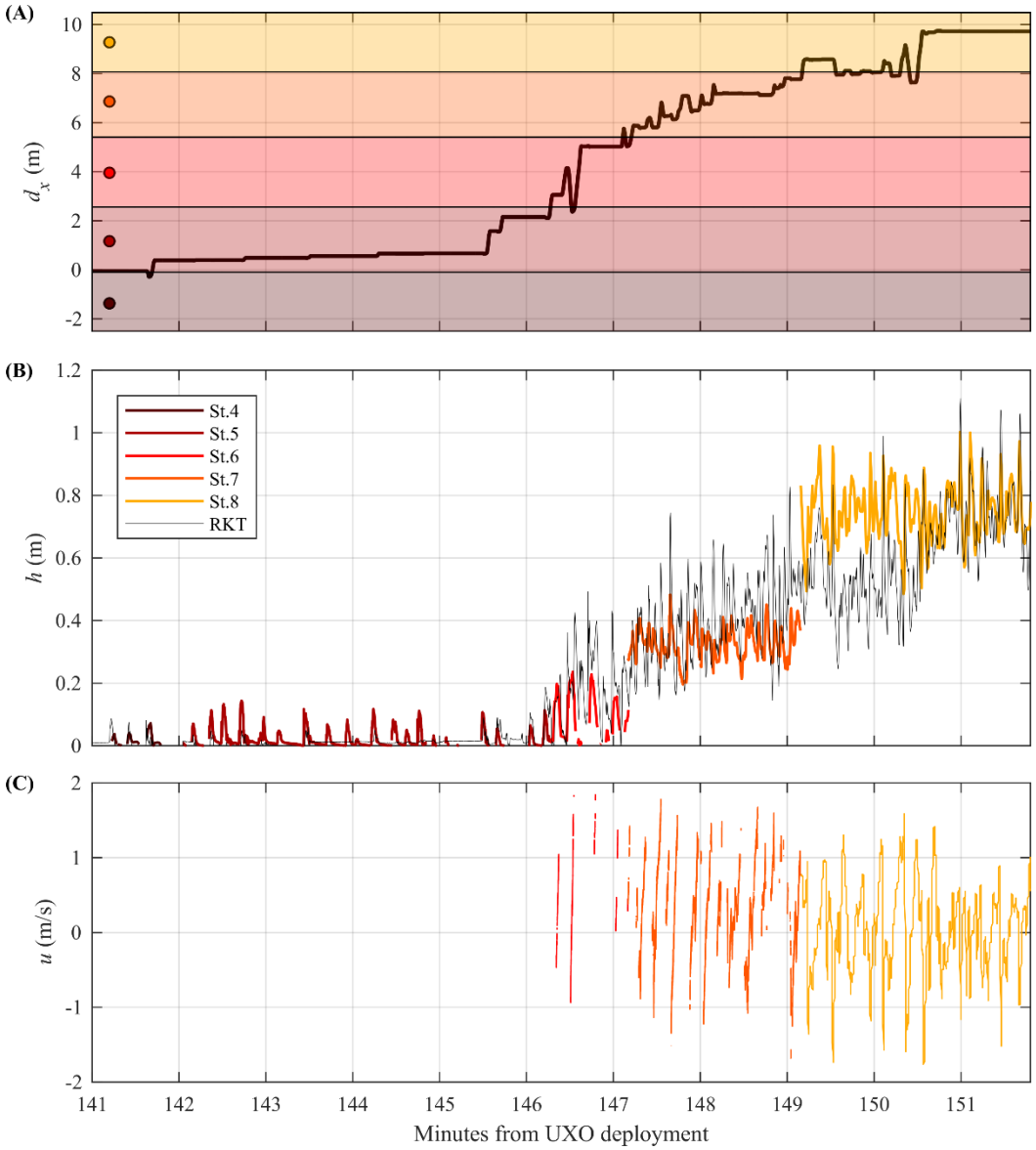

Figure 26. Example mobility of the instrumented RKT deployed at x = 11.4 m and y = -8.1 m on Aug. 24th. (A) IMU cross-shore trajectory (solid black line) and cross-shore locations of measuring stations 4 – 8 (circles, the color scheme follows panel B legend) referenced to 11.4 m. (B) Water level measurements (RBR) at stations 4 – 8 and at the munition location (PT). (C) Cross-shore flow velocities relative to stations 4 – 8 (Vectrino and JFE).

The RKT crossed four measuring stations (Station 5-8) during the 9.7 m migration. Therefore, water levels (Figure 26B) and cross-shore velocity (Figure 26C) of stations 4-8 are shown. *h* and *u* of each station are shown for a limited interval of time when the munition was near the station cross-shore location, (see the five rectangles, one for each station, helping visualize where the RKT is relative to the stations). Unfortunately, there are no velocity measurements for Station 4

and 5 during the time interval 141 – 146 minutes from deployment due to water levels below the flow velocity sensor elevation. Looking at the first three waves (Figure 26B), there is a time lag between $h_{st.4}$ and h_{RKT} with Station 4 landward of the RKT. The munition was closer to Station 5 during the third wave. Initially, the munition migrated offshore three times (h_{RKT} ~ 0.05 m) at small increments reaching a net distance of 0.07 m at minute 145.5. After that, four other events, increasing in intensity, caused offshore migration to 1.5 m (h_{RKT} ~ 0.08 m), 2.1 m (h_{RKT} ~ 0.08 m), 3 m (h_{RKT} ~ 0.18 m) and 4.1 m (h_{RKT} ~ 0.19 m) during backwash phases (within minute 146.5). At this point RKT was at the same cross-shore location of Station 6. An event of 0.23 m water depth and maximum uprush and backwash velocities of -1.2 and 1.8 m/s, managed to cause landward migration of 2.3 m followed by seaward migration of 5 m. Subsequently, the munition remained in place from 146.63 to 147.1 minutes. The motion restarted at 147.1 minutes when the RKT exited the swash zone, approaching Station 7. From this point h_{RKT} never again reached zero as the munition was constantly submerged. A series of events characterized by velocity magnitudes up to 1.8 m/s caused further net offshore movement towards Station 8 with an oscillating motion of onshore-offshore segments. The munition reached the final position at 9.7 m at 150.6 minutes after deployment. Eventually, the IMU stopped recording due to battery capacity and the trajectory tracking ceased.

4.6 Single Swash Event Cases

4.6.1 Observations of migration and object mobility number

Munition response for a *single* swash event can be classified as one of the following: no motion; upslope motion (during uprush); downslope motion (during backwash) or upslope followed by downslope motion. Setting a threshold of motion of 0.05 m, Table 10 provides the number of cases for each motion type. The maximum distances traveled for 58 retained swash events were 1.7 m and 1.8 m for onshore and offshore respectively.

Table 10. Number of cases for different type of motion during a single swash event (based on 58 cases tested in the swash zone).

Motion type	No motion	Upslope	Downslope	Upslope and downslope
# cases	36	5	4	13

A larger number of munitions was tested but due to the difficulties in capturing the cross-shore velocity measurements, many cases did not contain corresponding velocity data. These cases were not considered in the analysis. Flow velocity measurements may also be intermittent during the swash event. For this reason, a linear fit to the velocity time series, u_{fit}, was used in the analysis. Additionally, flow velocities are not often available for the initial part of the swash event and were extrapolated backwards in time until the instant of time where water level increase started.

A time series of object mobility number was estimated for all retained swash events. The temporal evolution of θ_m is shown as an example in Figure 27 for an 81-mm-nf case. The measured hydrodynamics, h (Figure 27A) and u (Figure 27B), are also reported for reference and to highlight the time windows of uprush and backwash phases. During this specific case, the 81-mm-nf traveled upslope during the uprush and stopped at 0.35 m of onshore motion (Figure 27D). The corresponding object mobility number shows a decreasing trend during uprush, due to

the decelerating flow. On the contrary, the backwash is characterized by a growing θ_m, due to the flow accelerating while receding seaward. However, the flow depths and mobility number are insufficient to cause seaward munition migration.

For each of the 58 cases tested, the θ_m time series was related to the time series of the increments of cross-shore distance traveled, Δd_x (Figure 28), where Δd_x at a given time t_i is the difference between $d_x(t_i)$ and $d_x(t_{i-1})$. The signs were preserved with positive for offshore and negative for onshore. Focusing on the uprush (negative-negative quadrant), if motion occurred (Δd_x not zero), the relationship has a parabolic shape for each event.

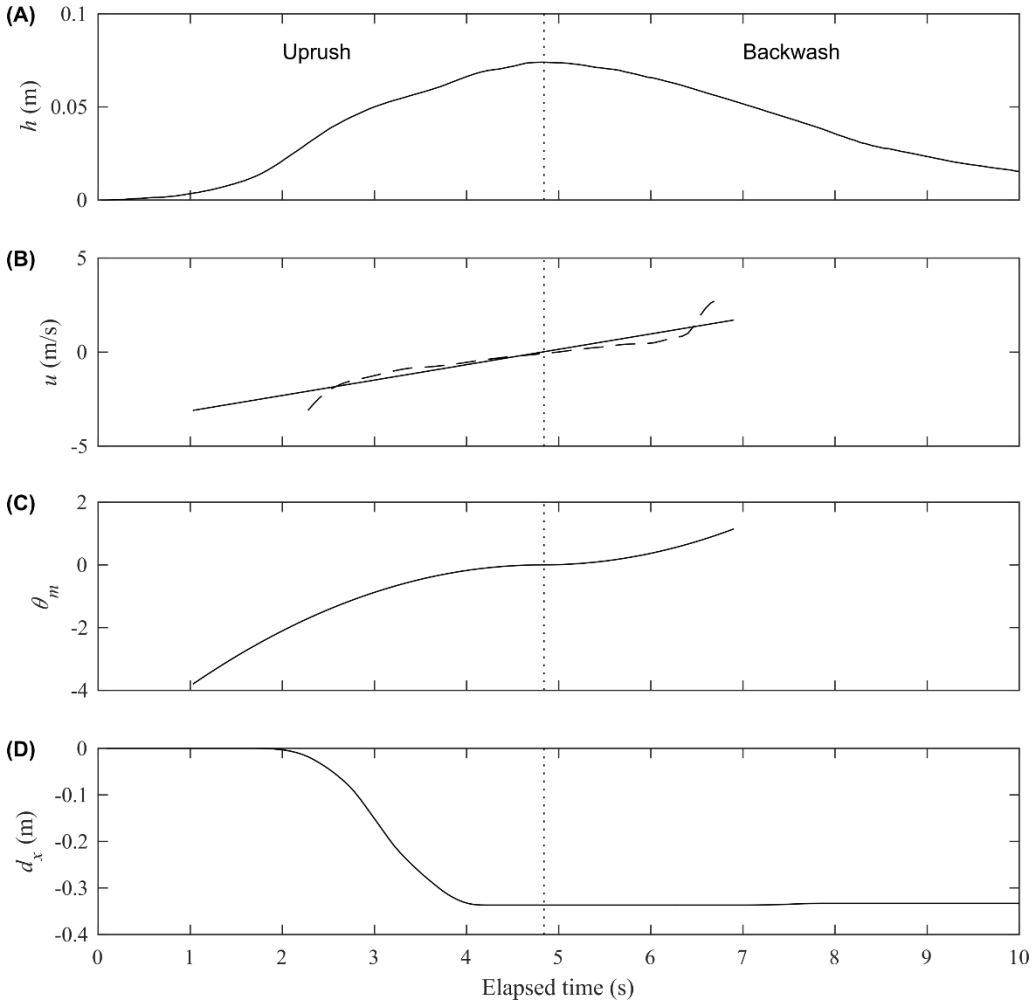

Figure 27. Example of the object mobility number time evolution during a swash event for an 81-mm-nf munition: (A) water depth; (B) cross-shore flow velocity, measured (dashed) and fitted (solid); (C) object mobility number; (D) munition trajectory.

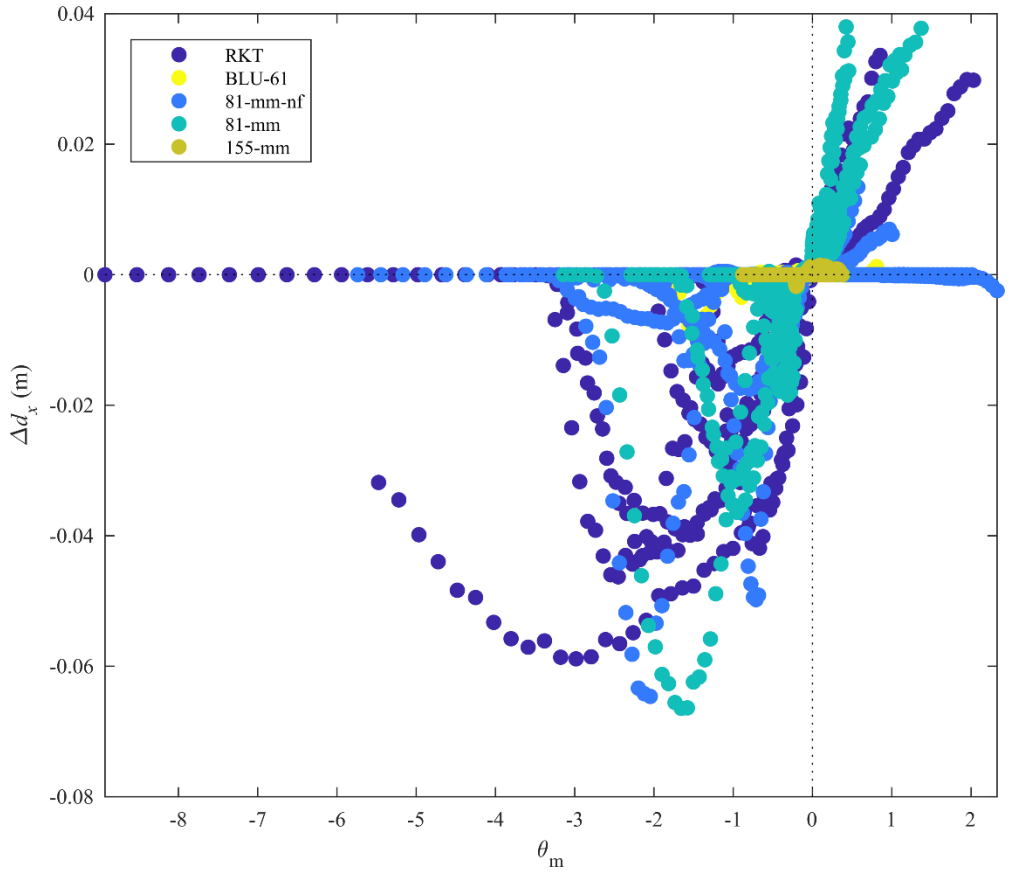

Figure 28. Time series of the object mobility number against the time series of increments of distance traveled for single event swash munition cases.

At the beginning of the uprush (maximum θ_m) the munition is subjected to an impact as Δd_x increases. Once the munition reaches the maximum landward Δd_x, there is a second trend where the munition decelerates (Δd_x decreases). For the backwash phase (positive-positive quadrant) the same parabolic trend is expected. However, due to difficulties in capturing the entire swash event with the velocity sensor, only a portion of the trend is observed. Similarly, as for the uprush, there is an increase in motion while θ_m increases due the downslope accelerating flow. Note that maximum Δd_x observed were nearly 0.07 m. Considering that the time interval between consecutive instants was 1/16 s, a 0.07 m increment translates to 1.12 m/s of munition motion. When the munition was not mobilized ($\Delta d_x = 0$), θ_m ranged from the two extremes, -9 and nearly 2.5 for uprush and backwash respectively. As discussed previously, the object mobility number cannot alone explain the mobility of munitions in the swash zone. In fact, although large object mobility numbers are observed, the corresponding munition response is not necessarily mobility.

For each swash event for which mobilization occurred, a representative value of object mobility number was determined integrating the object mobility number time series. Uprush and backwash phases were kept separated and therefore, if the munition was mobilized in both directions, two data points are obtained for the corresponding portions of the swash event. The integrated object mobility numbers were then related to the corresponding distances traveled (Figure 29). For the backwash, the last part of the event is not captured by the flow velocity

sensor. Thus, the migration was set to be the distance that occurred when velocity data were available. The uprush data (circles in Figure 29) roughly track with the integrated mobility number except for three data points corresponding to 81-mm-nf munitions (three light blue circles with θ_m between 5.5 and 7.5 and d_x below 0.4 m). Two of those values showed a net downslope motion. The GPS survey of the final location of the munition does not include information on whether the munition moved upslope during the uprush and returned in the initial place at the end of the backwash. The video imagery was obscured by foam denying the possibility to determine any potential upslope motion that was not captured by the IMU. The high uprush object mobility numbers and the absence of fins would suggest these finless 81-mm munitions did move onshore before migrating back offshore. Backwash data also seem to group around a straight line but with a larger slope compared to the uprush data. A larger slope indicates that lower mobility numbers are needed to mobilize a munition downslope; intuitive as the motion downslope is aided by gravity. A linear regression was performed on both data clusters with an r^2 correlation coefficient of 0.45 and 0.24 for backwash and uprush respectively. The slopes of the fitting lines are 0.50 and 0.12, again for backwash and uprush. The r^2 changes from 0.24 to 0.86 if the three 81-mm-nf points discussed above are discarded from the analysis.

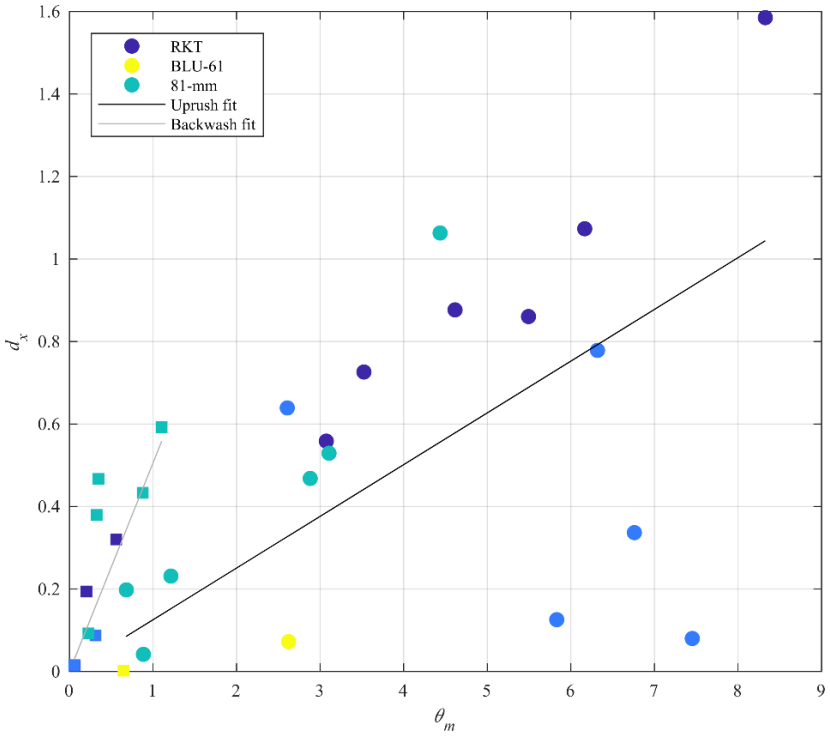

Figure 29. Relationship between the maximum distance traveled and the integrated object mobility number over the uprush (circles) or backwash (squares). The symbol colors represent different munition types. Solid lines are the lines of best linear fit for data of uprush (black) and backwash (grey).

4.6.2 Force balance

Forces time series were calculated for the 58 cases available. Figure 30 provides an example of the measurements collected, derived variables, and the forces during a swash event. The drag, friction and added mass coefficients were all set to 1 initially. The munition used for this example was a RKT. The swash event lasted for 10 s with maximum water depth above 0.15 m (Figure 30A). Flow acceleration du/dt, needed for the calculation of F_{facc}, was derived from u_{fit} (Figure 30C). The munition response was determined from the IMU. The derived cross-shore trajectory indicates an onshore motion that reached 0.5 m followed by an offshore motion of 2 m (Figure 30D). Munition velocity and munition acceleration were then determined from the smoothed munition trajectory (black lines in Figure 30B and 30C respectively). The munition, once mobilized, first accelerated and then decelerated prior to stopping 0.5 m landward of the initial position. For the next 3 s the munition remained in place. The flow reversed and the munition began moving offshore, showing again an acceleration phase followed by a deceleration before motion ceased.

The forces calculated are shown in Figure 30E. Drag and friction forces have the greatest magnitude and dominate the force balance. The drag force was maximally 69 N during the uprush phase while the friction magnitude was maximally 27.7 N and always opposed to the drag. The buoyancy magnitude, nearly constant, ranged between 2.2 N and 3 N due to the variability associated with munition submergence relative to water level. The time series of the sum of all forces excluding F_{macc} is reported in blue in Figure 30F. The areas highlighted in green indicate where, if the munition moves, the sum of the forces should be located (oriented). The example shows the sum of forces do not align with the munition acceleration force. Some possible explanations for the imbalance can be the use of a force balance rather than a torque balance (see for instance Traykovski and Austin, 2017)) or the initial coefficient values. This example and the other cases with munition motion show the munition acceleration force as substantially less than drag and friction (Figure 31) indicating C_d and C_f could be optimized as the corresponding forces act in opposition.

A coefficient calibration was performed using the cases that showed motion during the swash event to investigate whether a simple force balance can explain the motion of munitions. Two attempts were made varying at each time either the drag and the friction coefficient and fixing the other to a constant value. For the first attempt, C_d was set equal to 1 (C_d is near 1 for a large range of Reynolds numbers) and assumed to be constant throughout the entire swash event. The friction coefficient (and any potential effect of suction) is considered as time dependent and identified by rearranging equation (9) as

$$C_f = \frac{F_{macc} - (F_d + F_b + F_{facc})}{V_m\,(\rho_m - \rho_w)\,g\,cos\beta}. \tag{27}$$

C_f presents a similar shape for all cases (Figure 32) with larger values at the beginning and the end of the event and minimum values near flow reversal. This shape is due to the drag being nearly zero around flow reversal and the need for those two dominant terms to balance. On the contrary, when the uprush and backwash are characterized by their maximum velocities, the drag is high and so the friction must be larger to compensate. The C_f values obtained are confined between 0 and 4.

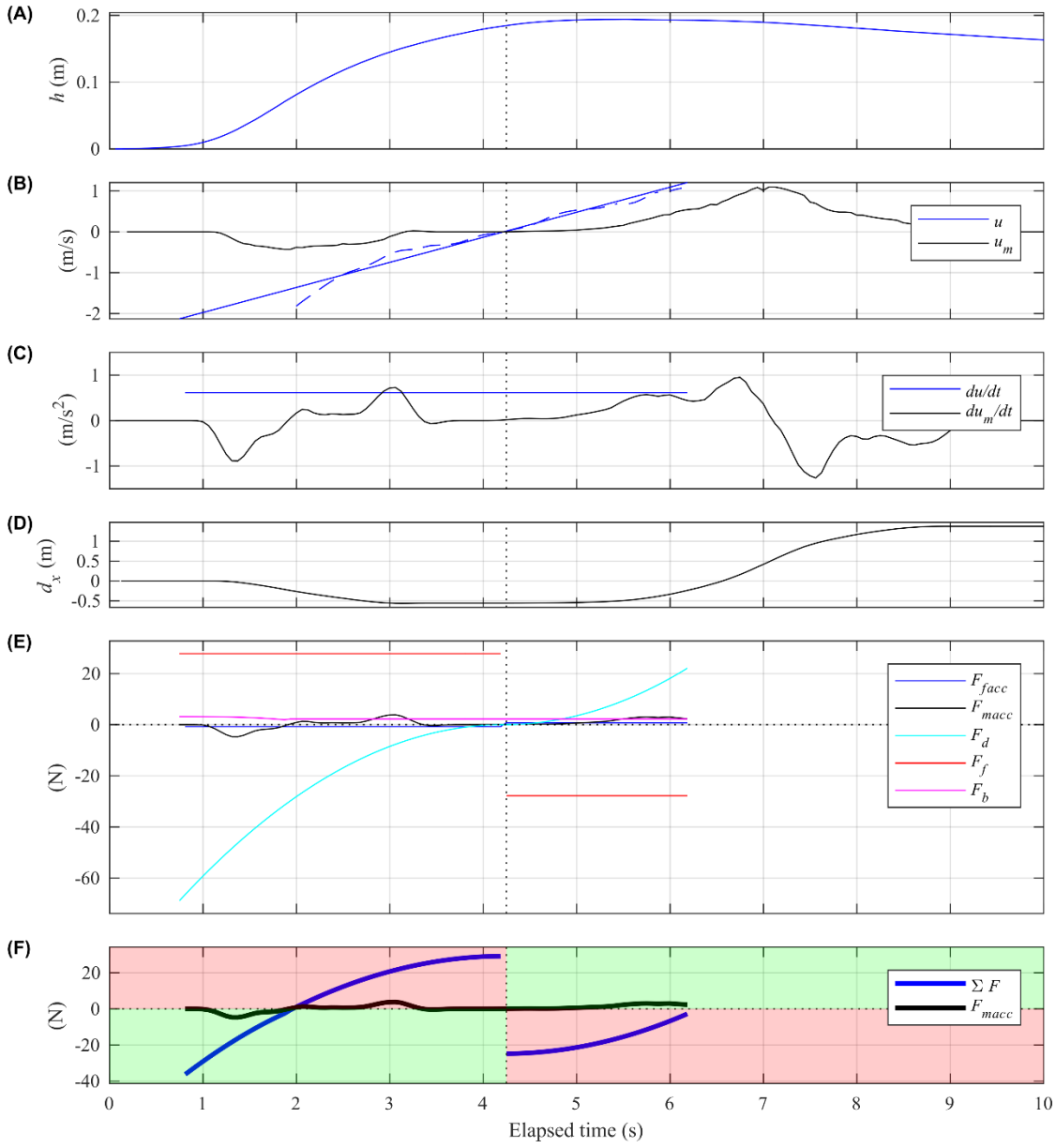

Figure 30. Example of the force balance terms and their derivation based on the measurements collected during a single swash event for an RTK munition: (A) water level; (B) cross-shore flow and munition velocities; (C) cross-shore flow and munition accelerations; (D) munition cross-shore trajectory; (E) forces applied to the munition, sign indicate force direction; (F) comparison between munition acceleration force and the sum of all the other forces.

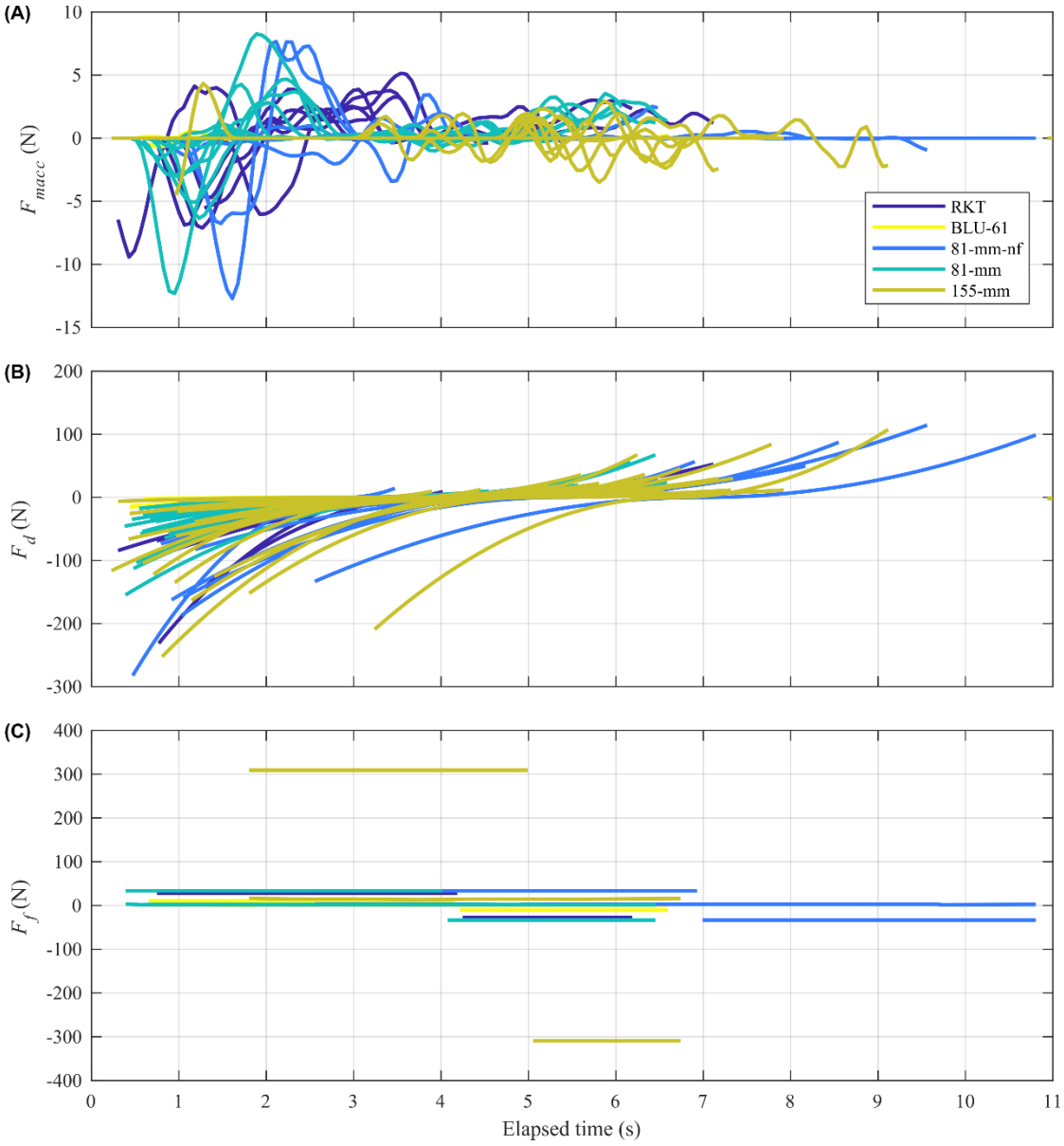

Figure 31. Temporal evolution of the main forces resulting from the 58 swash events. (A) Munition acceleration force; (B) drag force; (C) friction force. The color separation indicates a different type of munition.

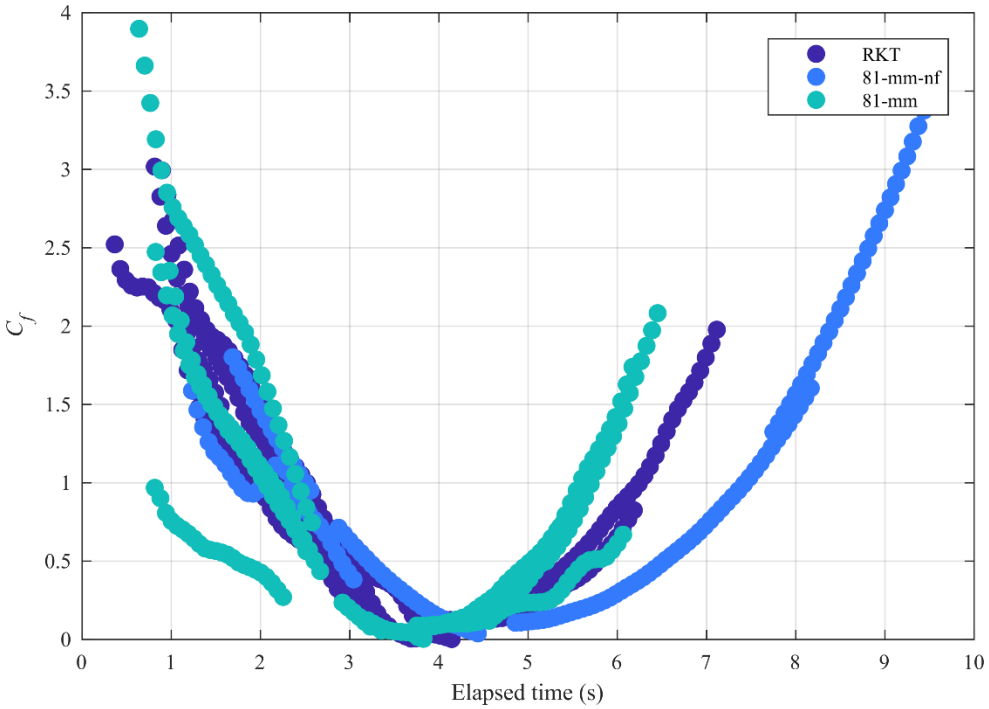

Figure 32. Friction coefficient temporal evolution determined from the force balance of motion cases.

For the second attempt, C_f was set to 0.4 (Luccio et al., 1998). The drag coefficient was then derived from the force balance (equation 3.11) as

$$C_d = \frac{F_{macc} - (F_f + F_b + F_{facc})}{\frac{1}{2}\rho_w D_m L_m u|u|}. \quad (28)$$

The time dependent drag coefficient (Figure 33A) shows the same trend for all cases of motion. The drag increases during the uprush as the flow decelerates and decreases during the backwash where the flow accelerates. At flow reversal (u = 0), equation (28) cannot be applied and this explains the gap of data in Figure 33A (between roughly 3.5 and 5 s). The C_d trend is similar to time varying friction coefficient from a drag law during a single swash event (Chardón-Maldonado et al., 2016). The obtained C_d values are between 0.06 and 0.75. Increasing the friction coefficient to from 0.4 to 1 results in C_d varying between 0.23 and 2.7.

A comparison between the time series of drag coefficient and the corresponding munition Reynolds number (equation 3.18) is shown in Figure 33B. The munition Reynolds number was found to be always greater than 40,000. The drag coefficient decreased with increasing Reynolds number as might be expected for flow around a cylinder.

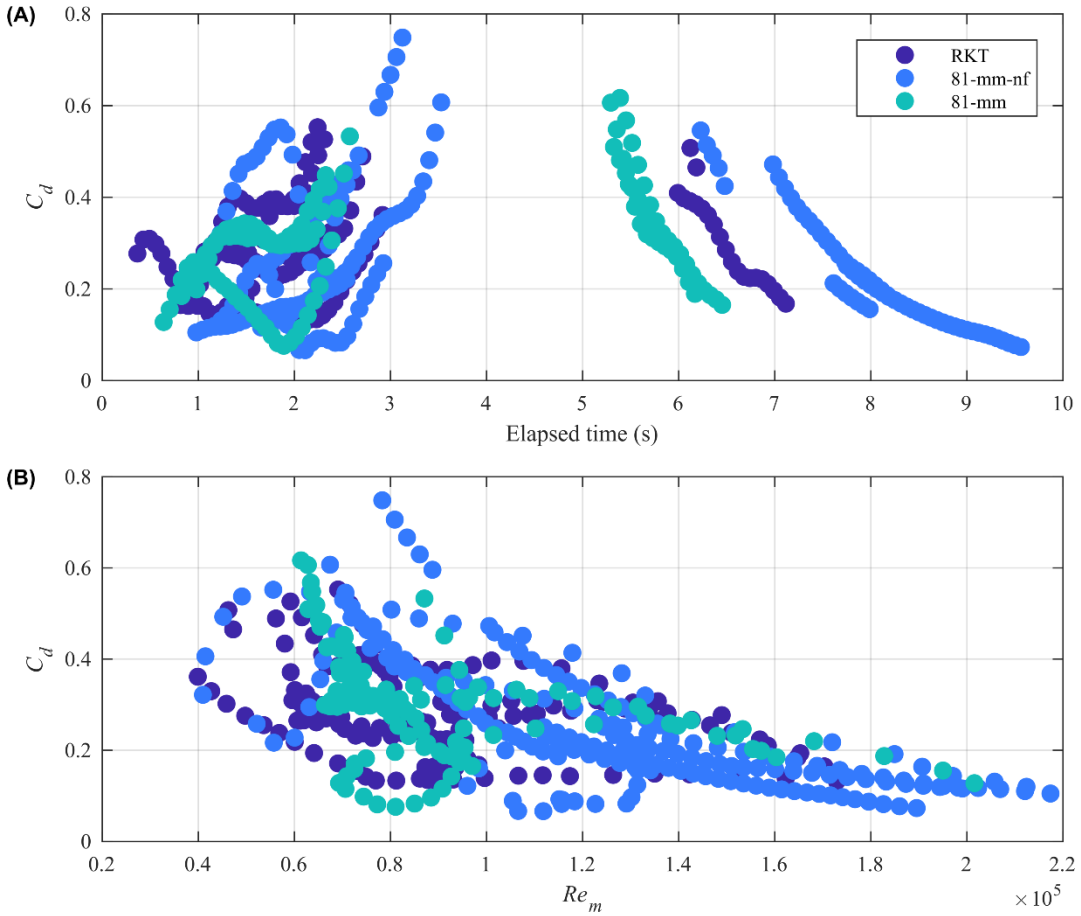

Figure 33. (A) Drag coefficient temporal evolution determined from the force balance of motion cases. (B) Drag coefficient as a function of the munition Reynolds number.

4.6.3 Impact force

The impact force was determined for 104 cases. The velocity was obtained from video imagery from camera UC. As the calculation of the impact force does not require a full velocity time series, cases that were discarded for the previous analysis are now included. A separation of motion/no-motion was performed to segregate the data. Here, different than previously, only munitions that moved during the uprush phase are classified as having motion (motion potentially related to the impact force, only present during the beginning of the uprush). The threshold distance used is 0.05 m. Only eight munitions (out of 104) were mobilized onshore. Note that the 58 cases mentioned in Table 10 are not all present in this group of 104 cases. Only cases for which the video imagery was present are used.

For a specific along-shore coordinate (corresponding to the munition initial location *y* coordinate), a time stack of images was generated for each swash event (Figure 34). The cross-shore impact velocity was determined manually for each event by identifying the slope of the runup (*dx*/*dt* in the image) at the moment the uprush impinged on the munition. The velocities at impact are on the order of 1 m/s and maximally 3 m/s. Impact force magnitudes can exceed 1000 N but typically range from 3.7 N to 625 N (Figure 35A,B). Maximum impact forces exceed maximum drag forces by a factor of 2 to 3. However, the most frequent observations are confined between 3.7 N and 300 N; comparable to the drag and the friction forces. Figure 35C

provides the relationship between the velocity of impact and the impact force highlighting the differences for different munition types. Assuming the water impinges the munition with a water depth greater than the munition diameter, the variation between different munitions in the impact force calculation is determined only by the impingement velocity and munition diameter and length. For fixed velocity, the greater the area of action (D_m by L) the greater the impact force.

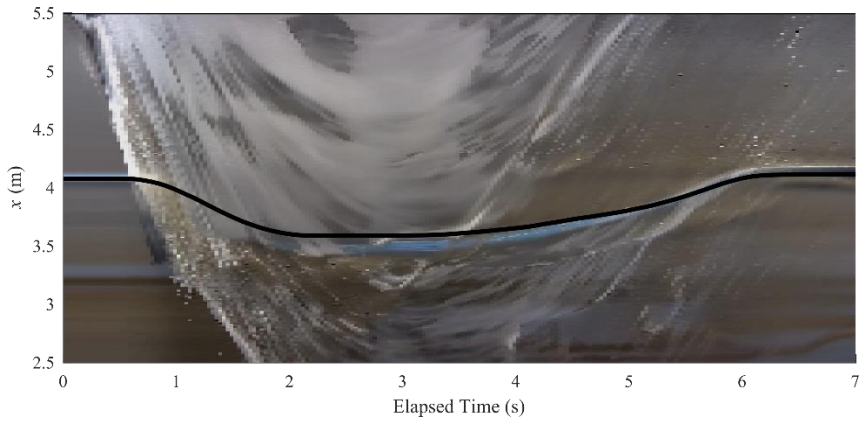

Figure 34. Example of video imagery time stack of one of the 58 swash events for a fixed y coordinate. Black solid line represents the munition trajectory detected from the IMU.

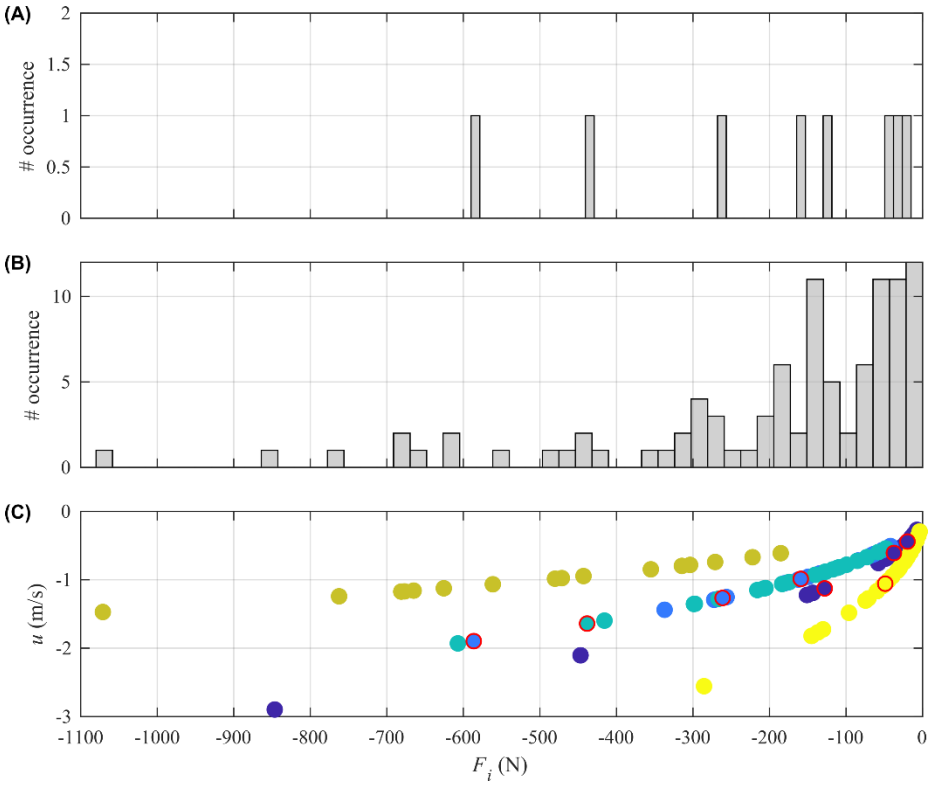

Figure 35. Impact force histograms for cases of motion (A) and no motion (B). Impact force as a function of the cross-shore velocity of impact (C). Color scheme indicates a different munition type (see Figure 30 for legend). Symbols circumscribed in red correspond to motion cases.

4.7 Discussion on Migration

Data from a large-scale laboratory study under near prototype forcing conditions showed initially proud munitions in medium sand in the swash zone and breaker zone can be mobilized. Migration data were captured using RTK GPS equipment, georeferenced imagery and inertial motion units inside some of the munitions. Munitions located in the swash zone generally mimicked the runup curve with a slight onshore migration followed by a more prolonged offshore migration (Figure 21). In addition, munitions tend to migrate the most during the initial stages of forcing (Figure 21). Migration slows or ceases when munitions enter deeper water and are offshore of bore collapse or when they are located landward beyond the extent where backwash forcing is capable of remobilization (Figure 21). The net migration of swash zone munitions was mostly offshore-directed (Figures 17 and 21) with only 46 out of 149 cases (31%) of net landward migration observed. Cross-shore migration showed some relationship with munition density with the less dense munitions generally migrating farther offshore (maximum distance of 20 m) and the most dense munitions having small or no migration (Figure 17). No obvious relation was found between the distance traveled and the object mobility number or the modified object mobility number. Breaker zone munitions were not reset in between runs (implying variable initial burial depths) and all munitions tended to exhibit less migration. Munitions migrated maximally 3.4 m onshore and 3.6 m offshore with no preferential migration direction (58 cases migrated offshore, 57 cases migrated onshore and 225 cases migrated less than 0.05 m). Munition migration distances were variable under the "same" offshore forcing conditions, "same" munitions placement and same munitions density indicating local, small-scale hydrodynamic and sediment transport processes are vitally important for predicting munitions processes. The variability in swash zone migration could not be well-described using empirical formulations related to offshore forcing; namely the munition bulk density, object mobility, Shields and Iribarren numbers with squared correlation coefficients of only 0.37 maximally. Additional tests incorporating initial munition orientation and dimensionless runup were unsuccessful. Poor correlation between forcing and migration distance was not fully unexpected considering, for example, the variability in migration with object mobility number (Figure 17; larger object mobility number does not equate to larger migration distances).

The data obtained here show that swash zone munitions tend to migrate offshore. The question arises as to how munitions are occasionally found on beaches. One option is that munitions appear on the foreshore through erosion of dunes or the foreshore through the process of exhumation. A second option is munitions are transported to the foreshore from a more offshore location. Indeed, LWE data showed that some onshore migration can occur but there was no preferential direction of migration for breaker zone munitions and migration distances were small (the latter possibly due to the short run durations). However, the LWE studies were limited, by necessity, in several ways that could be circumvented in the future: 1) The water level was not altered during the study. Altered water levels (tides) would change the location of wave breaking (forcing) and could perhaps change munition migration patterns; 2) The foreshore slopes for both studies were fairly steep (1:16 and 1:10) causing the downslope component of gravity to be a major driving force in munitions migration. The LWE facility could not accommodate a much shallower sloping foreshore indicative of a dissipative beach. A shallower sloping beach would de-emphasize the downslope gravity component and perhaps enable more capability for net onshore migration (especially with tidal variations); 3) Forcing conditions were near prototype for what might be identified as moderate forcing. Extreme event forcing could not

be tested but would likely be able to force an additional component of onshore migration perhaps leading to net migration in that direction. Indeed, analyses (UXO mobility model) indicated munitions initiated far offshore could experience net onshore transport and exposure under high energy waves and currents (NAVFAC, 2013), but the ability to be stranded on the foreshore was not tested; 4) All munitions tested were deployed initially proud – except subsequent runs in the breaker zone when munitions were not reset. Yet, migration is expected to be reduced when forcing acts upon partially buried munitions such that the conditions tested at LWE provided the best opportunity (under the forcing used) for munitions to experience a net onshore migration.

4.8 Discussion on Burial

Burial observations at LWE were governed by both foreshore morphologic changes as well as local scour processes (Figure 16C). Burial data indicated again the importance of munitions bulk density with the denser munitions having a greater relative burial depth (Figure 16A,B). Maximum burial ($B/D_m > 2$) was observed for the 20-mm with a bulk density of 7990 kg/m^3. Fluidization of the seabed may be one reason why B/D_m reached values greater than 1. Note that previous studies of object burial generally occurred under non-sheet flow conditions. Friedrichs et al. (2016) identified more than 600 cases of reported munitions-like object burial by waves (or waves + currents) in sand; with more than the 95% for Shields parameters less than 0.6, and none exceeding 2. In contrast, the observations made at LWE in the swash zone are associated with greater Shields numbers (1.3 – 7.5). The scour processes in sheet flow conditions and a fluidized bed may be different than those investigated by previous studies. Sheet flow conditions may enable dense objects to "sink" through the fluidized bed enhancing burial. Additional measurements and analysis would be required to further test this concept.

Equilibrium scour burial under combined waves and currents has been related to dimensionless forcing parameters: Keulegan-Carpenter number and Shields parameter with some success(Cantano-Lopera et al., 2011; Friedrichs et al., 2016a; Sumer and Fredsøe, 2001). Attempts using the parameters alone or in tandem provided moderate squared correlation coefficients with respect to relative burial depth ($r^2 = 0.45$ and $r^2 = 0.48$; Figure 18A). Thus, only roughly 50% of the variability in relative burial depth can be explained by these simple relationships for non-equilibrium burial depth.

4.9 Discussion on Force Balance and Impact Force

Munitions were deployed to be subjected to a single swash event while measuring simultaneously the munition trajectory and the hydrodynamics. Fifty-eight cases for which data, and especially velocity data, were available for the entire event were identified. The munitions generally remained in place. If mobilized, the type of motion was either upslope, downslope or both. A representative object mobility was defined for both uprush and backwash integrating the object mobility number temporal evolution in time and compared with the munition migration distance. Correlation coefficients were 0.25 and 0.45 for uprush and backwash indicating only 25 to 45% of the observed migration variability could be described by the mobility number.

Forces were estimated using a simple force balance equation to cases of munitions subjected to a single swash event. The forces considered are friction, drag, flow acceleration, buoyancy and the munition acceleration. The force balance analysis indicated that drag and friction dominate the processes for mobility. However, quantifying these forces, largely through varying coefficients, proved difficult. The predicted values were an order of magnitude larger than the munition force

indicating that more investigation is required and perhaps under more controlled conditions. A possibility for the relatively low munition acceleration force may be attributed to the assumption made that munitions move only by rolling. This was adopted to facilitate the derivation of the time series trajectory from the IMU. However, the munition could potentially slide or be lifted up and moved by saltation. If the transport mode is not rolling, the acceleration is underestimated. Additionally, the lift force should also be included and an analysis on the moment balance could be undertaken.

The forces time series, for cases of motion, were used to investigate the temporal evolution of the coefficients of friction and drag. Fixing one coefficient and letting the other vary in time, the expression of the coefficient was derived from the force balance equation. C_f values ranged between 0 and 4. The trends for C_f (C_d = 1) are consistent between cases and shows decreasing C_f during the uprush and increasing C_f during the backwash. These trends result from the compensation needed between drag and friction forces, being the largest in magnitude. Nandasena and Tanaka (2013) showed temporal evolution of the friction coefficient for different object materials with values generally below 0.8. Letting only C_f vary and maintaining C_d constant may be not appropriate for the dataset considered here. The drag coefficient was then considered as a variable assuming a constant friction (C_f = 1). The temporal evolution of C_d was evaluated through the force balance, similarly as for the friction coefficient. The results obtained are more commesnurate with what is expected regarding the swash event phases, with the drag coefficient a function of the hydrodynamics. C_d increases for decelerating flow (uprush) and decreases for accelerating flow as the friction factor of the bed shear stress does. The C_d values obtained were always below 0.8.

It is debatable whether the impact force of the flow on the munition should be included as a separate term in the force balance. For this reason, a separate analysis was performed as an investigation of the magnitudes of the impact force. It is hard to determine a threshold of motion based on the impact force, having a low number (8) of cases of upslope motion. Impact force for mobilized munitions ranged between 20 and 580 N. The magnitudes of the forces for no motion cases (96) suggest that large impact forces do not necessarily indicate munition mobilization. More investigation on the force of impact is required. The absence the water depth measurements at the initial munition location required the assumption of using D_m instead of h in the calculation of the impact force area. This assumption has an influence on the magnitude of the impact force.

4.10 Discussion on Sensor Capability: Inertial Motion Unit

Munition trajectories and final positions inferred from a simple algorithm were similar with moderate correlation (r^2 roughly 0.5) to those inferred from imagery and pre- and post-run RTK GPS measurements. Moderate correlation might be expected considering the IMU is a low-cost sensor and trajectories are affected by compounding error and data processing issues. The cumulative angle of rotation, φ_{roll}, was derived directly from the roll angle measurements. However, φ can also be derived indirectly by integrating the angular velocity time series from the gyroscope. Comparisons were made between the two approaches. In the gyroscope-derived, φ_{gyro}, approach, a cutoff of 10 °/s was used to neglect angular velocity data assumed to be associated with sensor noise. A cutoff is necessary because integrating small angular velocities an extended period of time when the munition is actually stationary can lead to large error in φ

(Frank et al., 2016). The error between φ_{roll} and φ_{gyro} was estimated for each case belonging to the motion group as

$$error = 100\frac{|\varphi_{roll}(t_{end}) - \varphi_{gyro}(t_{end})|}{\varphi_{roll}(t_{end})}, \quad (29)$$

where t_{end} refers to the end of the run. The average error for the 71 swash and breaker zone cases when the gyroscope also collected data was 13.5% with an error range of 0.09 to 70%. The roll angle was chosen for migration distance in this work because roll and heading data are associated to the same time vector (that differs from gyroscope time vector) on the IMU guaranteeing consistent data sampling and time synchronization. The trajectory, regardless of how the roll is quantified, is found cumulatively. Thus, any measurement error compounds over time. Other IMU vendors caution against using IMU data for position for long data records because the errors grow exponentially (CH Robotics). The error is likely to be exacerbated using the gyroscope data because a double integration is required to obtain position.

4.11 Discussion on Sensor Capability: Photocell Array

Manual measurements of burial were made post-run and using photocells on some 155-mm surrogate munitions (r^2 = 0.73). Apparent burial time histories were derived from array of photocells similar to optical or acoustical rings used around surrogate mines used in past efforts (Bradley et al., 2007; Traykovski et al., 2007). Normalized voltage thresholds of 0.5 were chosen for the swash zone and 0.2 for the breaker zone. The difference in threshold was due to intermittent emergence of the swash zone munitions and continually submergence of the breaker zone munitions under opaque water. Several examples of dimensionless burial depth, B/D_m, curves show a similar trend (Figure 36). Swash zone munitions experienced a rapid increase of relative burial depth at initial stages of the run followed by an approximately constant B/D_m for the remainder of the run. The observed trend matches the burial temporal evolution of cylinders in oscillatory flow (Demir and García 2007). However, the fairly constant normalized voltage for the majority of the run may also be attributed to light attenuation through the water causing the apparent burial of the munition. Normalized voltages decreased after wave forcing ceased causing the apparent burial to decrease. However, there is no physical mechanism without wave forcing that would exhume the munitions. Instead, the decrease in burial depth implies photocells overestimate the actual burial depth during the run due to the difficulties in separating actual burial (photocell covered by deposited sand) from apparent burial (photocell covered by turbid water). Thus, the decrease in normalized voltage after wave forcing is attributed to sediment settling post-run (post wave activity). Some swash zone cases appeared to confirm apparent burial where, for instance, a 155-mm deployed initially proud (B/D_m = 0) experienced 100% burial (B/D_m = 1) confirmed by manual surveys (grey curve in Figure 35). The findings suggest the photocells are likely appropriate for identifying burial on longer time scales in more opaque water or in the swash zone and for shorter time scales in less opaque water. Otherwise an alternate method for determining burial time series is required.

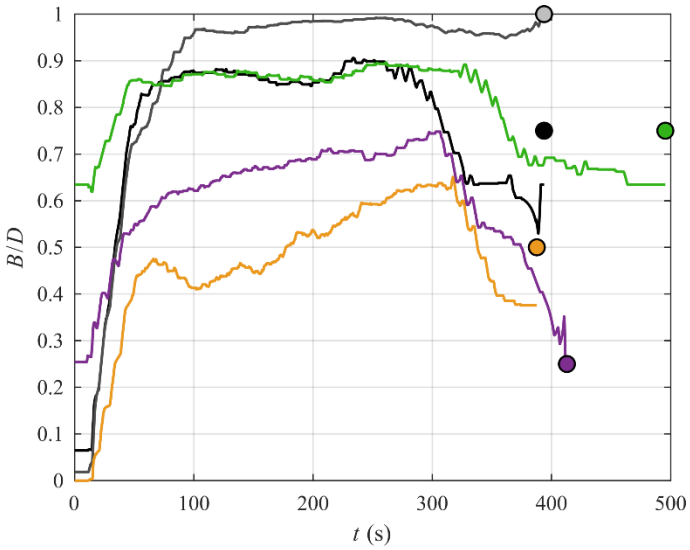

Figure 36. Examples of time evolution of dimensionless apparent burial depth of the swash zone deployed 155-mm surrogate munitions (curves) and corresponding post-run surveyed dimensionless burial depths (matching color circles).

5 Conclusions and Implications for Future Research / Implementation

This work investigated mobility and burial of unexploded ordnance in the dynamic swash zone. Experiments were carried out measuring simultaneously the munitions behavior and the forcing conditions. Surrogate munitions were first designed and fabricated with the capability of housing internal sensors for mobility and burial data collection. Particularly, the IMU was the most used sensor to derive munition trajectory. The designed munitions were used for two large-scale laboratory experiments where munitions were tested for short-term bursts of waves (2.5 - 10 minutes) and a two-month duration field experiment where munitions where left on site for the experiment duration.

The key findings are:

1) Munitions cross-shore migration were observed to be preferably offshore-oriented for both the short- (69%) and long- term (71%) studies. Munitions subjected to motion were usually the less dense munitions. Time series of migration showed that munitions were often mobilized upslope and downslope mimicking the runup curves but with offshore motion exceeding onshore motion. There was no preferential direction for breaker zone munitions and migration distances there were less than 3.6 m. Most of the swash zone munitions that migrated offshore start to bury once motion ceased. Maximum migration distances for swash zone munitions were on the order of 20 m. Empirical relationships using the object mobility number could only explain less than ~ 50% of the observed migration.

An example of variability in migration (and perhaps why mobility number or other simple parameters may not be adequate for migration are provided. Imagery (Figure 37) corresponding to LWE2 RUN 057 (Monochromatic waves with H = 0.5 m and T = 9 s) show motion of various surrogates and inerts. Four rockets and four 81 mm mortars were deployed just landward of the still water line. Two of each type of munition are surrogates with the other two being inerts. The order of deployment is as follows from bottom top of Figure 37A (top to bottom of Figure 37A-

1): surrogate rocket with an orientation of 0° (only the tip is visible in Figure 37A); inert rocket with an orientation of 0°; inert 81 mm mortar with an orientation of 90°; surrogate 81 mm mortar with an orientation of 90°; inert 81 mm mortar with an orientation of 90°; surrogate 81 mm mortar with an orientation of 90°; inert rocket with an orientation of 0°; and surrogate rocket with an orientation of 0°. Shortly after wave action, the rockets have rolled downslope or alongshore (Figure 37B and B-1). They mostly behave the same in that they tend to migrate offshore, but the travel distances and trajectories differ. The 81 mm mortars all initially behave the same with no motion. After more wave activity, the inert 81 mm mortars "wag" back and forth (presumably due to fins) and move offshore slightly. Surrogates and inerts do not appear to behave the same with surrogates remaining farther landward. This difference might be attributed to the lack of a nose cone in the inerts given the rest of the designs are consistent. Even the surrogate 81 mm mortars do not behave similarly with subsequent wave activity. One surrogate migrated several meters offshore while the 2nd surrogate remained mostly in place. In fact, the migrating surrogate had a final travel distance exceeding that of the inert 81 mm mortar.

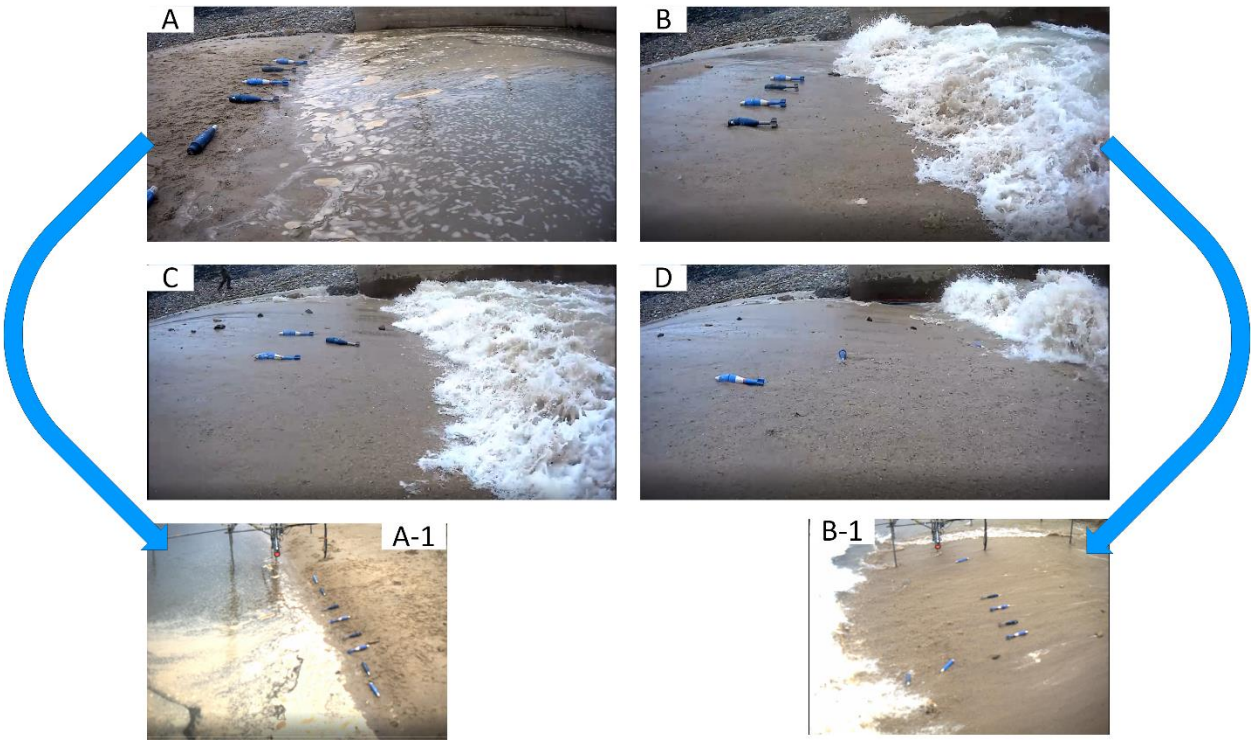

Figure 37. Imagery providing a qualitative view of the surrogate and inert motions for run 057 from LWE2.

A second example (Figure 38) shows contrasting observations of surrogate and inert motion from RUN053 LWE2 (Jonswap spectrum with H_s 0.52 m and T_p 3.28 s). Initial deployment (bottom to top of picture) contains a surrogate 155 mm Howitzer with an orientation of 0°, inert 155 mm with an orientation of 0°, two surrogate BLU 61 cluster bombs, inert 155 mm with an orientation

of 90°, and a surrogate 155 mm Howitzer with an orientation of 90°. The surrogate and inert with an initial orientation of 0° roll downslope with the first few waves (Figure 38B). The other surrogates and inerts do not migrate and begin to bury in place. The surrogate and inert with an initial orientation of 0° have rolled farther downslope near the end of wave cessation and both maintain roughly the same orientation. The BLU 61 cluster bombs have scoured in roughly half way (B/D_m = 0.5) and the other 155 mm Howitzers have scoured in only slightly.

Figure 38. Examples of surrogate and inert 155 mm Howitzer and BLU 61 cluster bomb motion under irregular wave forcing (RUN 053 LWE2).

These qualitative observations are further evidence of the variability in surrogate/inert motion as well as the variability even for the same type of object under the same forcing conditions. It is believed that even slight variations in local bathymetry or even offshore bathymetry altering local wave shoaling or refraction can influence how the munitions on the beach face respond to wave action.

2) Observed munition dimensionless burial depth ranged between 0 and 2 for short-term deployments and 0 and 14 for long term deployments in the field. Beach morphology changes are responsible for large burial depths obtained rapidly and are found to be an important factor for munition burial. Denser munitions bury deeper, especially for the short-term cases as scour dominates burial processes. Empirical relationships between the Keulegan-Carpenter number or the Shields number only described ~ 50% of the observed variance in munitions burial for short-term events.

3) Drag and friction were identified as the forces with largest magnitudes in a munitions migration force balance. A time dependency of the drag coefficient was obtained by rearranging the force balance. The analysis is still incomplete and requires more iterations of munitions motion and corresponding forcing for individual events. Additional cases of munitions migration and hydrodynamics time series for a single swash events may be extracted from the LWE studies to enlarge the number of the cases.

Both LWE and the field study results indicate large variability in the burial and migration of munitions due to the numerous parameters and factors that must play a role in their behavior. Additional data are required to enlarge the swash zone observations dataset for munition mobility and burial. Long-term investigations using numerous munitions of the same type and with density variations performed in controlled environments may help to narrow the important parameters and forces important for burial and migration.

6 Literature Cited

Aagaard, T., Holm, J., 1989. Digitization of Wave Run-up Using Video Records. Journal of Coastal Research 5, 6.

Bradley, J., Griffin, S., Thiele, M., Richardson, M.D., Thorne, P.D., 2007. An Acoustic-Instrumented Mine for Studying Subsequent Burial. IEEE Journal of Oceanic Engineering 32, 64–77. https://doi.org/10.1109/JOE.2007.890945

Bruder, B., Cristaudo, D., Puleo, J.A., 2018. Smart Surrogate Munitions for Nearshore Unexploded Ordnance Mobility/Burial Studies. IEEE Journal of Oceanic Engineering 1–20. https://doi.org/10.1109/JOE.2018.2871227

Calantoni, J., 2017. Long Time Series Measurements of Munitions Mobility in the Wave-Current Boundary Layer.

Calantoni, J., 2014. Informal Workshop on Burial and Mobility Modeling of Munitions in the Underwater Environment.

Cantano-Lopera, Y.A., Demir, S.T., Garcia, M.H., 2007. Self-Burial of Short Cylinders Under Oscillatory Flows and Combined Waves Plus Currents. IEEE Journal of Oceanic Engineering 32, 191–203.

Cantano-Lopera, Y.A., Landry, B.J., Garcia, M.H., 2011. Scour and burial mechanics of conical frustums on a sandy bed under combined flow conditions. Ocean Engineering 38, 1256–1268.

CH Robotics, n.d. Using Accelerometers to Estimate Position and Velocity. URL http://www.chrobotics.com/library/accel-position-velocity (accessed 6.1.19).

Chardón-Maldonado, P., Pintado-Patiño, J.C., Puleo, J.A., 2016. Advances in swash-zone research: Small-scale hydrodynamic and sediment transport processes. Coastal Engineering 18.

Dean, R.G., Dalrymple, R.A., 2002. Coastal Processes with Engineering Applications. Cambridge University Press.

Demir, S.T., García, M.H., 2007. Experimental Studies on Burial of Finite-Length Cylinders under Oscillatory Flow. Journal of Waterway, Port, Coastal, and Ocean Engineering 133, 117–124. https://doi.org/10.1061/(ASCE)0733-950X(2007)133:2(117)

Federation of American Scientists, 2017. Hydra-70 Rocket System Integration Information [WWW Document].

Frank, D., Landry, B.J., Calantoni, J., 2016. Investigating munitions mobility in oscillatory flows with Inertial Measurement Units, in: OCEANS 2016 MTS/IEEE Monterey. IEEE, pp. 1–6.

Friedrichs, C.T., Rennie, S.E., Brandt, A., 2016a. Self-burial of objects on sandy beds by scour: A synthesis of observations, in: Scour and Erosion. CRC Press, pp. 179–189.

Gross, B., Puleo, J.A., 2019. Mobility of Unexploded Ordnance using Spherical Surrogates on the Beach Face, in: Florida Shore and Beach Preservation Association. Presented at the Shoreline.

Harms, G.E., 1978. Improved BLU-63. DTIC Document.

Holland, K.T., Holman, R.A., Lippmann, T.C., Stanley, J., Plant, N., 1997. Practical use of video imagery in nearshore oceanographic field studies. IEEE Journal of Oceanic Engineering 22, 81–92.

Iribarren, C.R., Nogales, C., 1949. Protection des ports. Presented at the XVIIth Int. Nav. Congress, pp. 31–80.

Luccio, P.A., Voropayev, S.I., Fernando, H.J.S., Boyer, D.L., Houston, W.N., 1998. The motion of cobbles in the swash zone on an impermeable slope. Coastal Engineering 33, 41–60.

Nandasena, N.A.K., Tanaka, N., 2013. Boulder transport by high energy: Numerical model-fitting experimental observations. Ocean Engineering 57, 163–179. https://doi.org/10.1016/j.oceaneng.2012.09.012

NAVFAC, 2013. Hydrodynamic Mobility Analysis of UXO Transport Andrew Bay. Adak, Alaska.

Nielsen, P., 1993. Coastal Bottom Boundary Layers and Sediment Transport (Advanced Series on Coastal Engineering). World Scientific Publishing Company.

Puleo, J.A., Holland, K.T., 2001. Estimating swash zone friction coefficients on a sandy beach. Coastal Engineering 43, 25–40.

Rennie, S.E., Brandt, A., Friedrichs, C.T., 2017. Initiation of motion and scour burial of objects underwater. Ocean Engineering 131, 282–294.

Rogers, J., Celmins, I., 2009. Control Authority of a Mortar Using Internal Translating Mass Control: Defense Technical Information Center, Fort Belvoir, VA. https://doi.org/10.21236/ADA503142

Soulsby, R.L., Whitehouse, R.J.S., 1997. Threshold of Sediment Motion in Coastal Environments. Pacific Coasts and Ports ’97: Proceedings of the 13th Australasian Coastal and Ocean Engineering Conference and the 6th Australasian Port and Harbour Conference; Volume 1 145.

Sumer, B.M., Fredsøe, J., 2001. Scour around Pile in Combined Waves and Current. Journal of Hydraulic Engineering 127, 403–411. https://doi.org/10.1061/(ASCE)0733-9429(2001)127:5(403)

Traykovski, P., Austin, T., 2017. Continuous Monitoring of Mobility, Burial and Re-exposure of Underwater Munitions in Energetic Near-Shore Environments (No. SERDP Project MR-2319).

Traykovski, P., Richardson, M.D., Mayer, L.A., Irish, J.D., 2007. Mine Burial Experiments at the Martha's Vineyard Coastal Observatory. IEEE Journal of Oceanic Engineering 32, 150–166. https://doi.org/10.1109/JOE.2007.890956

Truelsen, C., Sumer, B.M., Fredsøe, J., 2005. Scour Around Spherical Bodies and Self-Burial. J. Waterway, Port, Coastal, Ocean Eng. 131, 1–13. https://doi.org/10.1061/(ASCE)0733-950X(2005)131:1(1)

Voropayev, S.I., Cense, A.W., McEachern, G.B., Boyer, D.L., Fernando, H.J.S., 2001. Dynamics of cobbles in the shoaling region of a surf zone. Ocean Eng. 28, 763–788.

Voropayev, S.I., Testik, F.Y., Fernando, H.J.S., Boyer, D.L., 2003. Morphodynamics and cobbles behavior in and near the surf zone. Ocean Engineering 30, 1741–1764. https://doi.org/10.1016/S0029-8018(03)00013-1

Voropayev, S. I., Testik, F.Y., Fernando, H.J.S., Boyer, D.L., 2003. Burial and scour around short cylinder under progressive shoaling waves. Ocean Engineering 30, 1647–1667.

Wessam, M.E., Chen, Z.H., 2015. Firing Precision Evaluation For Unguided Artillery Projectile, in: Proceedings of the 2015 International Conference on Artificial Intelligence and Industrial Engineering. Presented at the 2015 International Conference on Artificial Intelligence and Industrial Engineering, Atlantis Press, Phuket, Thailand. https://doi.org/10.2991/aiie-15.2015.156

Yeh, H., 2006. Maximum fluid forces in the tsunamic runup zone. Journal of Waterway Port Coastal and Ocean Engineering 132, 496–500.

7 Appendices

7A Technical Publications

7A.1 Refereed journal articles

Puleo, J.A., D. Krafft, J.C. Pintado-Patiño, and B. Bruder. 2017. Video-derived near bed and sheet flow sediment particle velocities in dam-break-driven swash, *Coastal Engineering,* 126, 27-36.

Bruder, B., D. Cristaudo, and J.A. Puleo. 2018. Smart surrogate munitions for nearshore unexploded ordnance mobility/burial studies, IEEE *Journal of Oceanic Engineering,* 99, 1-20.

Cristaudo, D. and J.A. Puleo. In Revision. Observation of migration and burial of munitions in the swash zone, *Ocean Engineering*.

7A.2. Dissertation / thesis

Cristaudo, D. 2020. Experimental study of burial and mobility of unexploded ordnance in the swash zone, PhD Dissertation, University of Delaware, 143 p.

Gross, B. 2019. Mobility of unexploded ordnance using spherical surrogates in the swash zone, Master's Thesis, University of Delaware, 59 p.

7A.3 Conference proceedings

Cristaudo, D., B. Bruder and J.A. Puleo. 2017. Instrumented surrogate munitions for nearshore unexploded ordnance studies – design and measurement capabilities. Proceedings of the MTS/IEEE Oceans Conference, Anchorage, Alaska.

7A.4 Conference abstracts

Gross, B.M. and J.A. Puleo. 2019. Mobility of Unexploded Ordnance using Spherical Surrogates on the Beach Face. National Conference on Beach Preservation Technology, Florida Shore and Beach Preservation Association, St. Augustine, FL.

Puleo, J.A. and D. Cristaudo. 2019. Mobility of Instrumented Unexploded Ordnance in the Nearshore Environment. SERDP/ESTCP Symposium, Washington, DC.

Cristaudo, D. and J.A. Puleo. 2018. Mobility of Instrumented Unexploded Ordnance in the Nearshore Environment. American Geophysical Union Fall Meeting, Washington, DC.

Gross, B., D. Cristaudo, and J.A. Puleo. 2018. Mobility of Unexploded Ordnance using Spherical Surrogates in the Swash Zone. American Geophysical Union Fall Meeting, Washington, DC.

Cristaudo, D. and J.A. Puleo. 2018. Analysis of the transport of instrumented surrogate munitions deployed in the swash zone of a large-scale laboratory beach. European Geophysical Union, Vienna Austria.

Gross, B., J.A. Puleo and D. Cristaudo. 2018. Mobility of Unexploded Ordnance using Spherical Surrogates in the Swash Zone. SERDP/ESTCP Symposium, Washington, DC.

Puleo, J.A., D. Cristaudo, B. Gross. 2018. Mobility of Instrumented Unexploded Ordnance in the Nearshore Environment. SERDP/ESTCP Symposium, Washington, DC.

Cristaudo, D. and J.A. Puleo. 2018. Long term behavior of unexploded ordnance in the nearshore environment. Young Coastal Scientists and Engineers Conference – Americas, Merida, Yucatan, Mexico.

Gross, B. and J.A. Puleo. 2018. Mobility of Unexploded Ordnance using Spherical Surrogates in the Swash Zone. Young Coastal Scientists and Engineers Conference – Americas, Merida, Yucatan, Mexico.

Puleo, J.A. and D. Cristaudo. 2017. Nearshore unexploded ordnance studies using instrumented surrogate munitions. SERDP/ESTCP Symposium, Washington, DC.

Cristaudo, D. J.A. Puleo, and B. Bruder. 2017. Instrumented surrogate munitions for nearshore unexploded ordnance mobility studies - design and measurement capabilities. IEEE/MTS Oceans Conference, Anchorage, Alaska.

Cristaudo, D., B. Bruder and J.A. Puleo. 2017. Preliminary results of a munitions mobility study in the swash zone. Young Coastal Scientists and Engineers Conference - Americas, Dauphin Island, AL.

Bruder, B., D. Cristaudo and J.A. Puleo. 2016. Observing migration and burial of unexploded ordnance in the nearshore environment with instrumented surrogates. AGU Fall Meeting, San Francisco, CA.

Cristaudo, D., B. Bruder and J.A. Puleo. 2016. Quantification of hydrodynamic forcing on smart munitions on the beach face – design of smart munitions. AGU Fall Meeting, San Francisco, CA.

Puleo, J.A., J.C. Pintado-Patino, D. Krafft and B. Bruder. 2016. Sediment particle velocities in the sheet layer of dam break driven swash. AGU Fall Meeting, San Francisco, CA.

Cristaudo, D., B. Bruder and J.A. Puleo. 2016. Quantification of hydrodynamic forcing on smart munitions in a large wave flume – experimental plan and design of smart munitions. Young Coastal Scientists and Engineers Conference - Americas, Kingston, Ontario, Canada.

Krafft, D., J.A. Puleo, and J.C. Pintado-Patino. 2016. Quantification of swash-zone velocities in the sheet flow layer using particle image velocimetry. EC14C-1002. AGU Ocean Sciences Meeting, New Orleans, LA.

Bruder, B., D. Cristaudo and J.A. Puleo. 2016. Quantification of hydrodynamic forcing on spherical objects in the swash zone. EC14C-0997. AGU Ocean Sciences Meeting, New Orleans, LA.

7A.5 Scientific or technical awards

SERDP 2019 Project of the Year award

7B Experiment Data Server

Surrogate munitions design documents, CAD drawing, Experiment planning documents and quality controlled data are available on the Munitions Response data server housed at the University of Delaware.